First Observation of An Excited Charm Baryon Decaying to Omega Charm Baryon at the BABAR Experiment

Rahmi Bula

SLAC-R-881

Prepared for the Department of Energy
under contract number DE-AC02-76SF00515

Printed in the United States of America. Available from the National Technical Information Service, U.S. Department of Commerce, 5285 Port Royal Road, Springfield, VA 22161.

First Observation of an Exited Charm Baryon Ω_c^* decaying to $\Omega_c^0\gamma$ at the *BABAR* Experiment

by

Rahmi Bula

A Dissertation Submitted to the University at Albany, State University of New York in Partial Fulfillment of the Requirements for the Degree of Doctor of Philosophy

College of Arts & Sciences

Department of Physics

2006

Abbreviations

$\Omega_c^* \rightarrow \Omega_c^0(\Omega^-\pi^+)\gamma \equiv C1$ $\qquad$ $\Omega_c^0 \rightarrow \Omega^-\pi^+ \equiv$ c1

$\Omega_c^* \rightarrow \Omega_c^0(\Omega^-\pi^+\pi^0)\gamma \equiv C2$ $\qquad$ $\Omega_c^0 \rightarrow \Omega^-\pi^+\pi^0 \equiv$ c2

$\Omega_c^* \rightarrow \Omega_c^0(\Omega^-\pi^+\pi^-\pi^+)\gamma \equiv C3$ $\qquad$ $\Omega_c^0 \rightarrow \Omega^-\pi^+\pi^-\pi^+ \equiv$ c3

$\Omega_c^* \rightarrow \Omega_c^0(\Xi^-K^-\pi^+\pi^+)\gamma \equiv C4$ $\qquad$ $\Omega_c^0 \rightarrow \Xi^-K^-\pi^+\pi^+ \equiv$ c4

$\Omega_c^* - \Omega_c^0 + 2.6975(GeV) \equiv \Delta\Omega_c^*$ $\qquad$ $\Omega_c^0 - \Omega^- + 1.6725(GeV) \equiv \Delta\Omega_c^0$

(speed of the light c $\equiv$ 1)

$\Omega_c^* - \Omega_c^0 \equiv \delta$ m

Monte Carlo $\equiv$ MC

Positron Electron Project $\equiv$ PEP-II

The Silicon Vertex Tracker $\equiv$ SVT

Drift Chamber $\equiv$ DCH

Detection of Internally Reflected Cherenkov light $\equiv$ DIRC

Electromagnetic Calorimeter $\equiv$ EMC

Instrumented Flux Return $\equiv$ IFR

Abstract

We have carried out a search for a charmed baryon Ω_c^* decaying to Ω_c^0 and a γ where Ω_c candidates are reconstructed using decay modes $\Omega^-\pi^+$(c1), $\Omega^-\pi^+\pi^0$(c2), $\Omega^-\pi^+\pi^-\pi^+$(c3) and $\Xi^-K^-\pi^+\pi^+$(c4). This search is performed by analyzing integrated luminosity of 230.7 fb^{-1} data collected by the *BABAR* detector at the Stanford Linear Accelerator Center. In decay channel $\Omega_c^* \to \Omega_c^0(\Omega^-\pi^+)\gamma$ (C1), we observe a signal yield of $39.2^{+9.8}_{-9.1}(stat) \pm 6.0(syst)$ events with a significance of 4.2 standard deviations. In decay channels $\Omega_c^* \to \Omega_c^0(\Omega^-\pi^+\ \pi^0)\gamma$ (C2) and $\Omega_c^* \to \Omega_c^0(\Xi^-K^-\ \pi^+\ \pi^+)\gamma$ (C4), we observe signal yields of $55.2^{16.1}_{-15.2} \pm 5.6$ and $20.2^{+9.3}_{-8.5} \pm 3.1$ with significances of 3.4 and 2.0 σ, respectively. As for the $\Omega_c^* \to \Omega_c^0(\Omega^-\pi^+\ \pi^-\ \pi^+)\gamma$ (C3) decay channel , we observe signal yields of $-5.1^{+5.3.8}_{-4.7} \pm 1.0$ without a positive significance. We assume the same production mechanism for the four decay channels of Ω_c^* studied. By combining these four channels, the fit results in a signal yield of $105.3^{+21.2}_{-20.5} \pm 6.0$ events with a significance of 5.2 σ. We report the mass difference $\Omega_c^* - \Omega_c^0(\delta\,\mathrm{m})$ of the singly charmed baryon Ω_c^* to be $70.8^{+1.0}_{-1.0} \pm 1.1$ MeV. Finally, the ratios of production cross sections are calculated: $\frac{\sigma(e^+e^-\to C1)}{\sigma(e^+e^-\to c1)} = 0.71^{+0.19}_{-0.18} \pm 0.11$, $\frac{\sigma(e^+e^-\to C2)}{\sigma(e^+e^-\to c2)} = 1.76^{+0.71}_{-0.69} \pm 0.19$, $\frac{\sigma(e^+e^-\to C3)}{\sigma(e^+e^-\to c3)} = -0.66^{+0.74}_{-0.66} \pm 0.13$, $\frac{\sigma(e^+e^-\to C4)}{\sigma(e^+e^-\to c4)} = 1.70^{+1.0}_{-1.0} \pm 0.27$ and $\frac{\sigma(e^+e^-\to \Omega_c^*\ (combined))}{\sigma(e^+e^-\to \Omega_c^0\ (combined))} = 1.0^{+0.23}_{-0.22} \pm 0.11$.

To my Family

Acknowledgments

This dissertation could not have been completed without the help of others who have been supporting me. I would like to thank family, my sisters Esra and Reyhan, and my mother Raziye for their support and love.

I would also like to extend my thanks to the Albany physics groups and other supporting groups within the physics department. But particularly professor Saj Alam for his support and generosity. I would like to thank to Dr. Frank Whappler for his help and friendship. I would like to thank to professor Jesse Earnst, Dr. Samya Zain, Dr. Shamona Ahmed, Dr. Muhammad Saleem, Liu Jian, Bin Pan for their friendship and support. I would like to thank to all Albany Physics Faculty especially to professor John Kimball for his friendship and support. I would like to thank to Donna Collins. I also would like to thank to Dr. Dalaver Anjum for his great friendship.

I would also like to thank the *BABAR* group(s). I would like to thank to charm AWG group, Dr. Brian Peterson, Dr. David Williams, Dr. Prafulla Kumar Behera, Dr. Mat Charles, professor Bill (William) Dunwoodie and professor Brian Meadows for their original ideas and contributions on this analysis.

I would like to thank to dissertation committee group, professor John Kimball, professor Brian Meadows, professor Jesse A. Ernst, Dr. Brian Peterson, Dr. Prafulla Kumar Behera.

Specicial thanks to my co-advisor, Dr. Prafulla Kumar Behera for his support and advices in Physics and life. He has become an inspiration in my life.

I thank also my supportive group of friends outside the Physics department, my special friendship group. I would like to thank my soulmate Florencia Cornet for

her continues support of every kind I can imagine. I would like to thank Ali Dalkilic who is and has been a tremendous financial and moral support.

Contents

List of Figures

List of Tables

Chapter 1

Introduction

The production of charm baryons is not fully explored and provides an interesting environment to study the dynamics of quark-gluon interactions. All singly-charmed baryons having zero orbital angular momentum have been discovered, except for the $J^P = \frac{3}{2}$ css state, denoted as Ω_c^*. In this dissertation, first observation of Ω_c^* at BABAR experiment is given in detail.

1.1 The Original Quark Model

In 1963 Murray Gell-Mann and George Zweig independently proposed quark model. According to the model, all hadrons are composite systems of two or three fundamental constituents called quarks. In the model there were only three types of quarks represented by the symbols u, d, and s named as up, down and sideways (new name, strange) respectively. After the original quark model introduction three other quarks called charm, bottom and top were discovered. The u, d and s quarks have charges of $\frac{+2e}{3}$, $\frac{-e}{3}$, and $\frac{-e}{3}$, respectively. Each quark has a spin of $\frac{1}{2}$ and a

baryon number of $\frac{1}{3}$. Composition of hadrons could be explained by following rules. Mesons consist of one quark and anti-quark and Baryons consist of three quarks.

1.1.1 Up and Down Quarks

The up and down quarks are the most common and least massive quarks. They are the constituents of protons and neutrons.

1.1.2 The Strange Quark

In 1947 during a study of cosmic ray interactions, a product of a proton collision with a nucleus was found to live for much longer time than expected: 10^{-10} seconds instead of the expected 10^{-23} seconds. This particle was named the lambda particle (Λ^0 ,1947) and the property which caused it to live so long was strange therefore name 'strange quark' (1964) is given to one of the quarks from which the lambda particle is constructed. The lambda is made up of three quarks: an up, a down and a strange quark.

The shorter lifetime of 10^{-23} seconds was expected because the lambda was expected to participate in the strong interaction, and that usually leads to such very short lifetimes. The long observed lifetime helped develop a new conservation law for such decays called the "conservation of strangeness". According to this new law a particle decay by the strong or electromagnetic interactions preserve the strangeness quantum number. The presence of a strange quark in a particle is denoted by a quantum number S=-1.

1.1.3 The Charm Quark

Although the original quark model was highly successful in classifying particles, there were some problems between predictions of the model and certain experimental decay rates. Physicists argued that if there are four leptons (as was thought at the time), there should be four quarks because of an underlying symmetry in nature. Consequently, a forth quark, designated by c, was given a new property, or quantum number, called charm in 1967. The charm quark has a charge $\frac{+2e}{3}$, but its new property of charm , which is denoted by $C = +1$ ($C = -1$ for its anti-quark) distinguishes it from the other three quarks. Charm, like strangeness, is conserved in strong and electromagnetic interactions, but not in weak interactions.

J/ψ was predicted in 1970 by Sheldon Glashow, John Iliopoulos, and Luciano Maiani, and first observed in 1974, with the simultaneous discovery of the J/ψ charm particle at SLAC by a group led by Burton Richter and at BNL by a group led by Samuel C. C. Ting. The particle was named J by the BNL group and ψ by the SLAC group; when the naming controversy could not be resolved, the compromise J/ψ was adopted.

1.1.4 The Bottom Quark

In 1973 Kobayashi and Maskawa predicted bottom and top quarks. In 1977, an experimental group at Fermilab led by Leon Lederman discovered a new resonance at 9.4 $\frac{GeV}{c^2}$ which was interpreted as a bottom-antibottom quark pair and called the Υ meson. The reaction being studied was $p + N \rightarrow \mu^+\mu^- + X$

where N was a copper or platinum nucleus.

1.1.5 The Top Quark

Convincing evidence for the observation of the top quark was reported by Fermilab 's Tevatron facility in April 1995. The evidence was found in the collision products of 0.9 TeV protons with equally energetic anti-protons in the proton-anti-proton collider.

1.2 The Standard Model (SM)

In particle physics SM was developed at the beginning of 1970s and it describes the strong, weak, and electromagnetic fundamental forces, as well as the fundamental particles that make up all matter. SM is a quantum field theory consistent with both quantum mechanics and special relativity. To date, almost all experimental tests of the three forces described by SM have agreed with its predictions.

SM is not a complete theory of fundamental interactions, primarily because it does not describe the gravitational force. We do not know what causes the fundamental particles to have masses. The simplest idea is called the Higgs mechanism. This mechanism involves one additional particle, called the Higgs boson, and one additional force type, mediated by exchanges of this boson. The Higgs particle has not yet been observed: if it exists, it should have a mass greater than about 80GeV/c2. The Large Hadron Collider at CERN is intended to search for the Higgs particle and distinguish between competing concepts as well as other ideas. Thus, this one aspect of the Standard Model does not yet have the status of 'theory' but still remains in the realm of hypothesis or model.

In SM, the theory of the electroweak interaction describes the weak and electromagnetic interactions. The theory of the electroweak interaction is combined

with the theory of quantum chromodynamics. All of these theories are gauge theories, meaning that they model the forces between fermions by coupling them to bosons which mediate (or "carry") the forces. The Lagrangian of each set of mediating bosons is invariant under a transformation called a gauge transformation, so these mediating bosons are referred to as gauge bosons. The bosons in the Standard Model are: Photons, which mediate the electromagnetic interaction. W and Z bosons, which mediate the weak nuclear force. Eight species of gluons, which mediate the strong nuclear force. The Higgs bosons, which induce spontaneous symmetry breaking of the electroweak gauge group and are responsible for the existence of inertial mass.

1.3 Charm Baryons

The predicted spectroscopy of ground state baryons containing a single charmed quark was mapped out in 1974 (M. K. Gaillard, B. W. Lee and J. L. Rosner, Rev. Mod. Phys. 47, 277 (1977). Figure 1.1 shows ground state $\frac{1}{2}^+$ and $\frac{3}{2}^+$ charmed baryons.

The first evidence for a single charmed baryon Λ_c^+ was published in 1975. In 2002, the SELEX collaboration published evidence of a doubly charmed baryon, but this claim has yet to be confirmed by another experiment.

1.4 Theoretical Predictions of Ω_c^*

The $J^P = 3/2^+$ baryon with constituent quark content *css*, the so-called Ω_c^* charm baryon, is the final L=0 singly-charmed baryon predicted by the quark model

in the SU(4) 20-plet whose observation has not yet been reported. Similar to the Ξ_c' discovered in 1999 at CLEO, the dominant decay mode of the Ω_c^* is expected to be electromagnetic, $\Omega_c^* \to \Omega_c^0\gamma$ (Figure 1.2), where the mass difference between Ω_c^* and Ω_c^0 is smaller than the pion mass. Mass predictions for Ω_c^* as well as for other charmed baryons are given in Table 1.1. From this table we see that the theoretical Ω_c^* mass value varies between 2659 and 2836 MeV: Potential models are given in detail at [3,11-13,14], chiral perturbation theory at [4], chiral quark model at [9], heavy quar k effective theory at [10,22], non-relativistic quark models at [15,16], bag models at [17-19], lattice QCD at [20,21], SU(4) Skyrmion model at [23], group theoretical model s at [24,25], and other models at [5-8, 26-28].

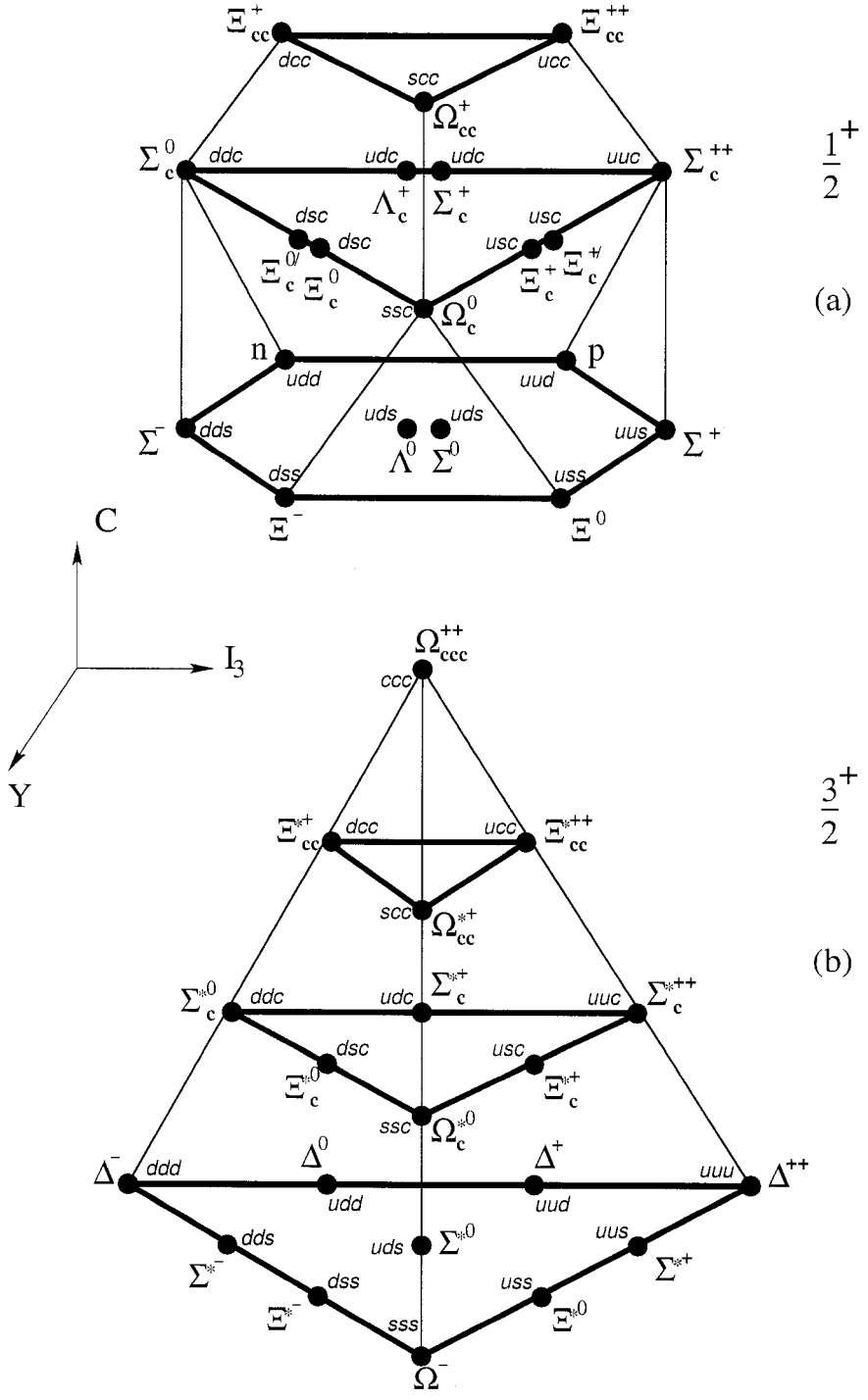

Figure 1.1: Charmed baryon SU(4) 20-plets

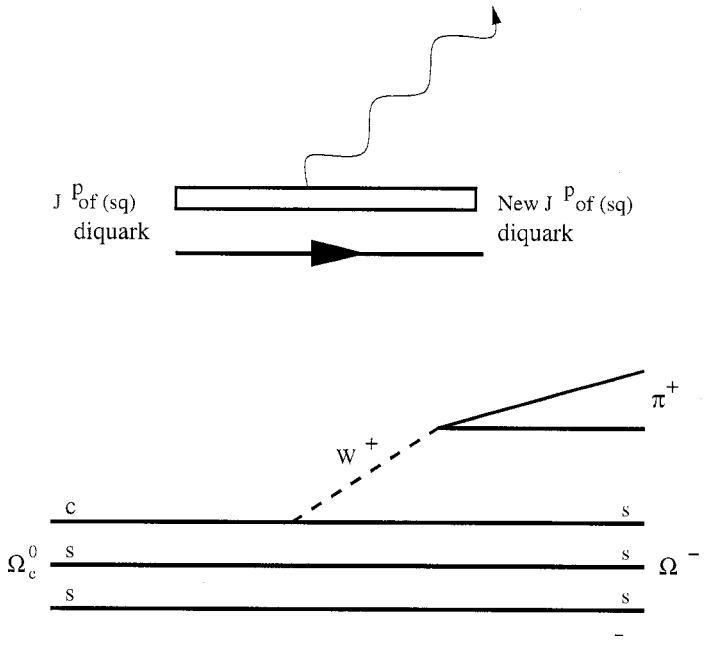

Figure 1.2: Ω_c^* and Ω_c^0 decay diagrams

Table 1.1: Theoretical predictions for several charmed baryon masses.

Ref.	$\Xi_c^{'}$ (MeV)	Ξ_{cc} (MeV)	Ω_{cc} (MeV)	Ω_c^* (MeV)	Ξ_{cc}^* (MeV)	Ω_{cc}^* (MeV)
[2]	2569± 6	3610± 3	3804± 8	2767± 7	3735± 17	3850± 25
[3]			3737	2760		3797
[4]	2579			2768		
[5]				2771		
[6]	2580± 20	3660± 70	3740± 80	2770± 30	3740± 70	3820± 80
[7]	2582	3676	3787	2775	3746	3851
[8]	2580± 10			2770± 10		
[9]	2593			2765		
[10]	2581± 2			2761± 5		
[11]	2510	3550	3730	2720	3610	3770
[12]	2532			2780		
[13]	2566	3605	3732	2836	3680	3801
[14]	2558	3613	3703	2775	3741	3835
[15]	2590			2805		
[16]	2608			2822		
[17]	2530	3511	3664	2764	3630	3764
[18]	2500			2710		
[19]	2467			2659		
[20]				2767 ± 35		
[21]	2570			2660		
[22]	2570	3610	3710	2740	3680	3760
[23]	2596	3752	3934	2811	3793	3964
[24]	2600	3725	3915	2811	3783	3953
[25]	2690	3700	3960	2810	3768	3931
[26]	2583				2772	
[27]	2542	3710	3852	2798	3781	3923
[28]	2578	3661	3785	2782	3732	3856

Chapter 2

BABAR Experiment

2.1 Positron Electron Project (PEP-II)

The accelerator at *BABAR* experiment has two sections. One of them is Linear accelerator(LINAC) and the the other one is PEP-II in which e^- and e^+ beams have asymmetric energies. The 3.2 km LINAC is made from over 80,000 copper discs and cylinders brazed together. In the LINAC, electron and positron beams are accelerated to the required high energies. PEP-II is located at SLAC and operating at the Upsilon 4S resonance. The PEP-II facility consists of two independent storage rings, which are some 5 meters underground, 700 meters in diameter and 2200 meters in circumference, located atop of each other in the PEP tunnel. The accelerator and storage ring were designed for $3.00X10^{33}\frac{1}{cm^2} \times s^{-1}$ luminosity.

At the western end of the tunnel is the electron gun, which produces the electrons to be accelerated. A filament that is heated by an electrical current flowing through it releases a few electrons into the space around it. When a strong electric field is applied, more electrons are pulled out of the hot filament and accelerated toward to

the beginning of the LINAC.

After the first ten feet of the LINAC, the electrons are traveling in bunches with an energy of approximately 10 MeV (99.9% of the speed of light). These bunches have a tendency to spread out in the directions perpendINACicular to their travel. Because a spread out beam gives fewer collisions than a narrowly focused one, the electron and positron bunches are sent into damping rings (small storage rings) to be focused. The synchrotron radiation decreases the motion in any direction, while the cavity re-accelerates only those in the desired direction. Thus, the bunch of electrons or positrons becomes more and more parallel in motion as the radiation "damps out" motion in the unwanted directions. The bunches are then returned to the LINAC to gain more energy as they travel along it.

The microwaves from a klystron are fed into the accelerator structure, which is a small portion of LINAC, via the waveguides. This creates a pattern of electric and magnetic fields, which form an electromagnetic wave traveling down the accelerator. The trick is to have the electrons or positrons arrive in each cell or cavity of the accelerator just at the right time to get maximum push from the electric field in the cavity. Of course, since positrons have opposite charge from electrons, they must arrive when the field is pointing the opposite way to be pushed in the same direction.

From the LINAC, periodically the electrons are injected (clock-wise) into the High Energy Ring (HER) and positrons are injected (anticlock-wise) into the Low Energy Ring (LER). The high-energy ring (HER), in which has a 9-GeV electron beam travels, was an upgrade of the existing PEP facility. The low-energy ring, in which 3.1-GeV positron beams travels, was newly constructed.

Positrons, which are the anti particles of electrons, are produced by diverting some of the electrons from the accelerator and colliding them with a large piece

of tungsten. This collision produces large numbers of electron-positron pairs. The positrons are collected and sent back along a separate line to the start of the L. At the beginning of the LINAC, magnets turn the positrons around and send them into the LINAC where they are accelerated in just the same way as electrons.

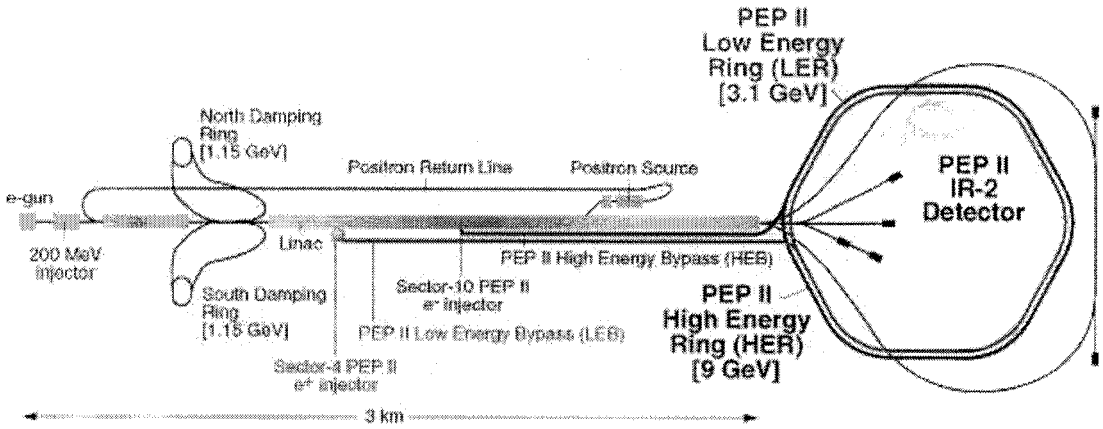

Figure 2.1: PEP II scheme.

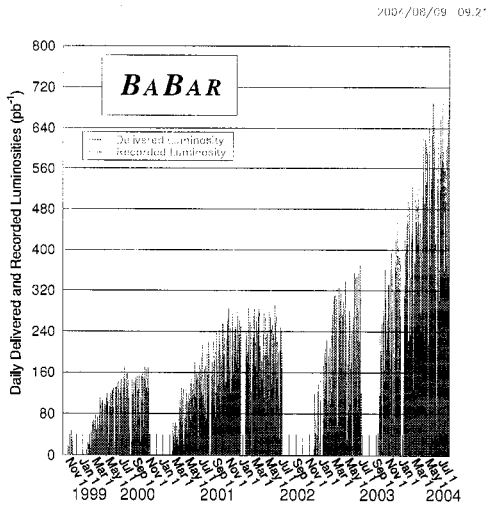

Figure 2.2: Daily recorded luminosity.

2.1.1 Physics at PEP-II

When e^+e^- collides at the interaction point, they usually scatter. Occationally they anhilate to produce a virtual photon which fragments into a pair of fermions. The production cross sections of fermions is shown in Table 2.1.

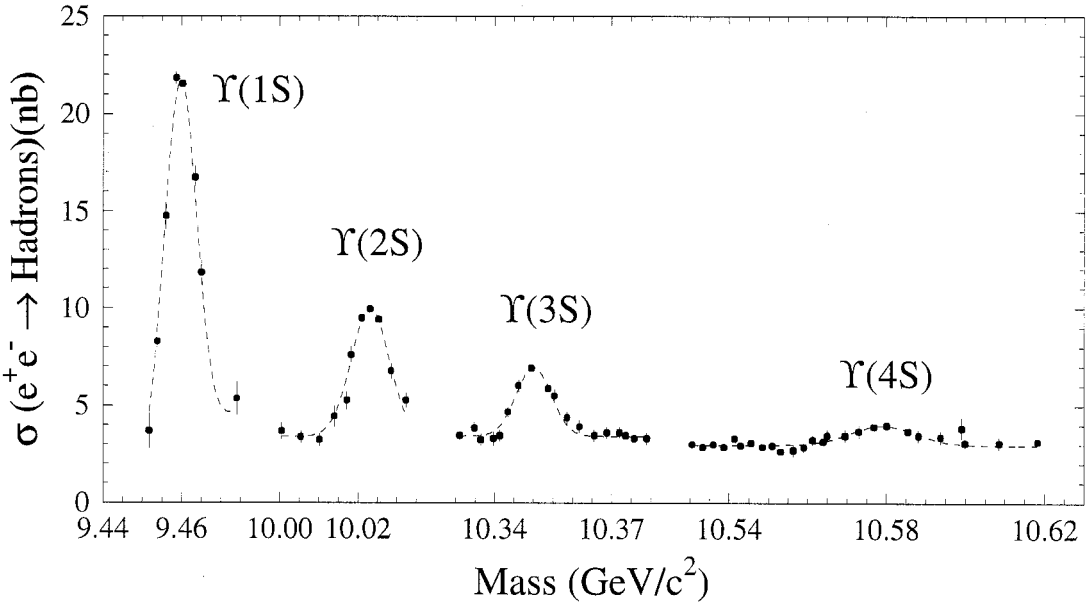

Figure 2.3: Υ resonances is shown for CLEO experiment. The Υ resonances at *BABAR* experiment is similar.

The production cross sections of fermions is shown in Table 2.1.

2.2 The *BABAR* Detector

The *BABAR* detector [30] was built by a large international team of scientists and engineers. Figure 2.4 shows a longitudinal section through the detector center, and 2.2 shows an end view with the main dimensions. The detector surrounds the PEP-

Table 2.1: Production cross-sections at $\Upsilon(4S)$

fermions	cross-section (nb)
$b\bar{b}$	1.05
$c\bar{c}$	1.30
$s\bar{s}$	0.35
$u\bar{u}$	1.35
$d\bar{d}$	0.35
$\tau^+\tau^-$	0.94
$\mu^+\mu^-$	1.16
e^-e^+	40

II interaction region. To maximize the geometric acceptance for the boosted $\Upsilon(4S)$ decays, the whole detector is offset relative to the beam-beam interaction point (IP) by 0.37 m in the direction of the lower energy beam. The inner detector consists of a silicon vertex tracker, a drift chamber, a ring-imaging Cherenkov detector, and a CsI calorimeter. These detector systems are surrounded by a superconducting solenoid that gives a field of 1.5 T. The steel flux return is instrumented for muon and neutral hadron detection.

2.2.1 The Silicon Vertex Tracker (SVT)

The SVT, which is the innermost component of the *BABAR* detector, is made out of five layers of silicon wafers cylindrically centered about the beam pipe. The SVT has been designed to measure positions and momenta of charged particles as well as rate of energy loss over distance ($\frac{dE}{dx}$) for particle Identification. The inner three layers primarily provide position and angle information for the measurement of the vertex position. The outer two layers are at much larger radii, providing the

coordinate and angle measurements needed for linking SVT and DCH tracks. The SVT was designed to provide a transverse vertex resolution of 100 m perpendicular to the beam line.

The five layers of double-sided sensors provide up to ten measurements of dE/dx in the SVT for each charged track Figure 2.5 and 2.6. Layers 1, 2, 3, 4, and 5 have 6, 6, 6, 16, and 18 modules, respectively. The ϕ measuring strips are parallel to the beam and the z measuring strips are oriented transversely to the beam axis. The ϕ and z resolutions are aproximitly 40 μm.

A channel in SVT is a reversly biased p-n junction diode. If we apply pozitive potential to n side and negative to the p side (reverse-biase) the electric field pulls the electrons and creates a depletion reigion. Thermal generation of electrons and holes creates a small bias current. When a charged particle passes through the depletion region it creates electrons and holes in opposite directions which is another current. The current created by charged particle passing through the depletion region electron alters bias current. A hit in SVT produces a change in the bias current.

For minimum ionizing particles (MIPs), the dE/dx resolution is 14%. A two-sigma separation between kaons and pions can be achieved for momenta up to 500 MeV/c and between kaon and proton beyond 1 GeV/c, Figure 2.7.

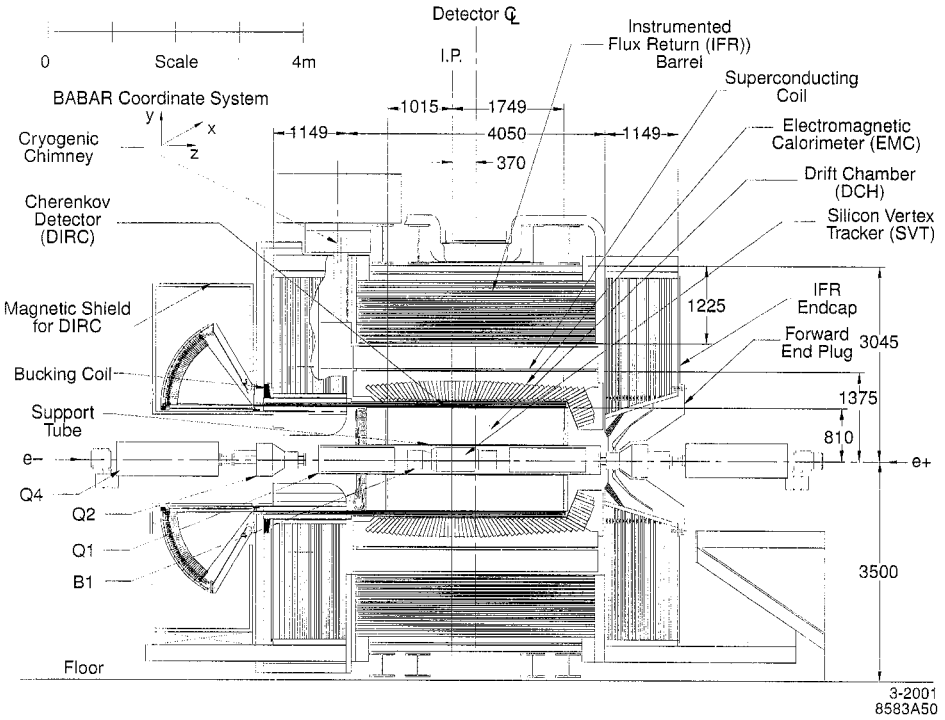

Figure 2.4: The *BABAR* detector.

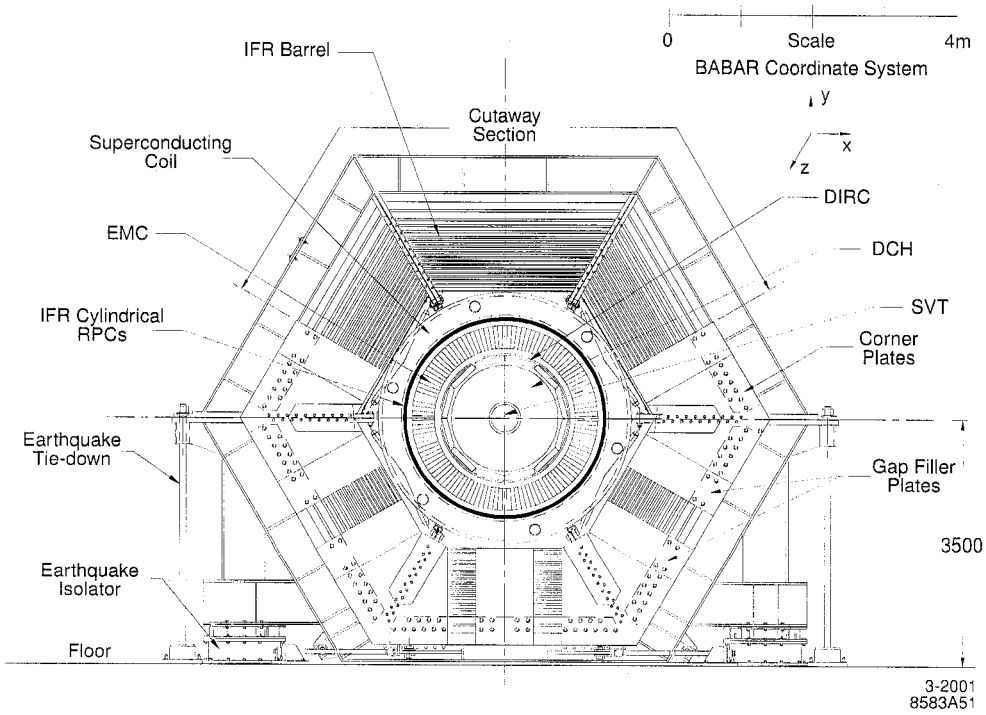

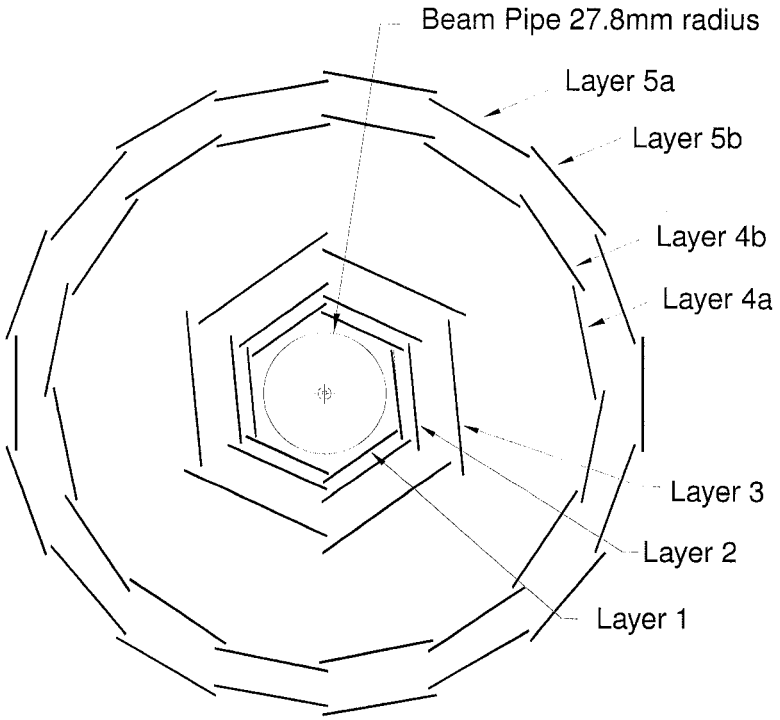

Figure 2.5: view of the SVT.

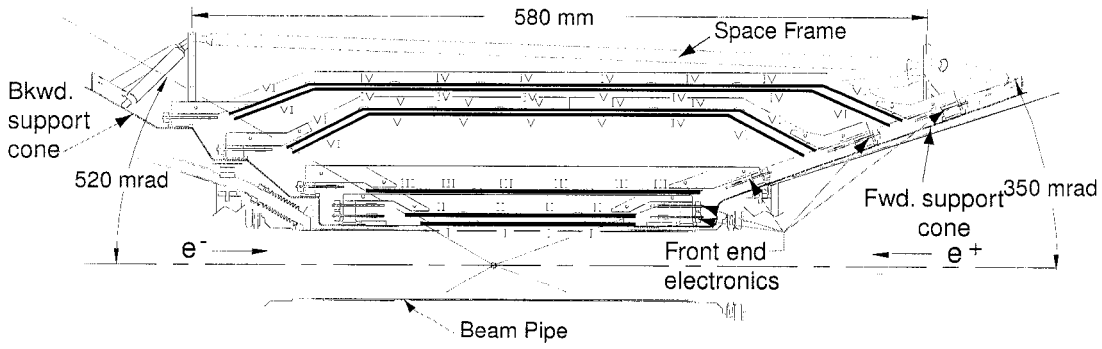

Figure 2.6: Longitudinal view of SVT.

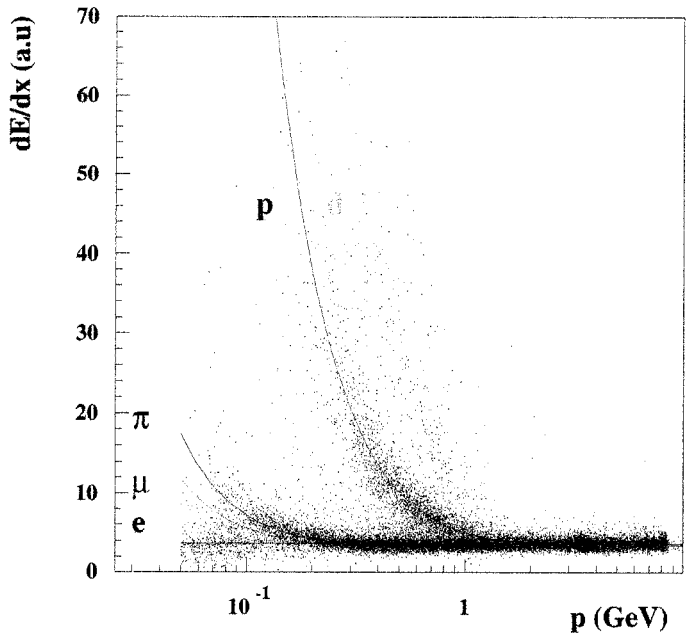

Figure 2.7: dE/dx as a function of track momentum for SVT.

2.2.2 Drift Chamber (DCH)

The DCH (2.8), which is placed next to the SVT, is about 2.8m long, and it has 0.81m outer and 0.24 inner radius. The DCH consists of 40 cylindrical layers of drift cells centered around the beam pipe. 40 layers of cells provide up to 40 spatial and ionization loss (dE/dx) measurements for charged particles with tranverse momentum 180 $\frac{MeV}{c}$ or more.

The drift cells, which are hexagonal in shape, are about 0.02m wide and 2.80m long. Each cell is made of six field wires arranged in a hexagon and one sense wire in the center. To measure the z coordinate, some wires are aligned at a small angle to the z-axis. There is gas mixture of 80% helium and 20% isobutane inside the cells. The field wires are at ground potential and the sense wires are at apositive high voltage. A charged particle passing through the cells can ionize the gas on its path. Ionized electrons accelerate towards pozitively charged sense wires. The accelerating electrons cause secondary ionization which creates a pulse on the sense wire. The total charge collected by a sense wire is proportional to dE/dx.

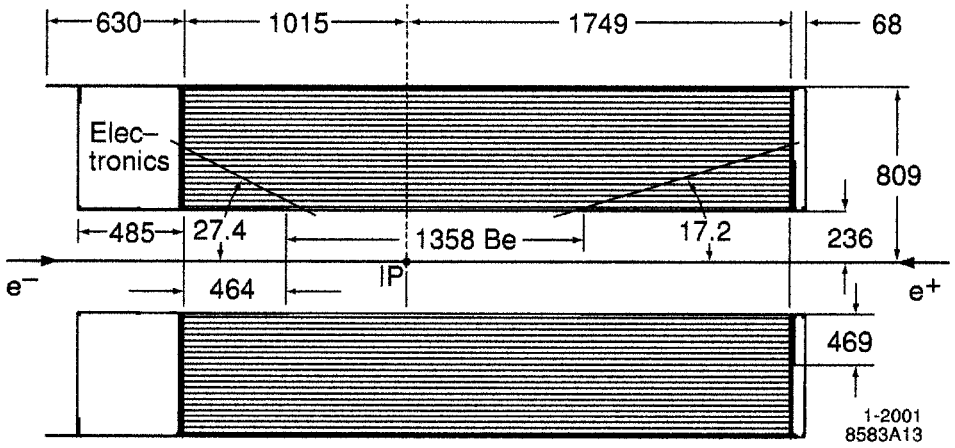

Figure 2.8: Longitudinal view of the DCH.

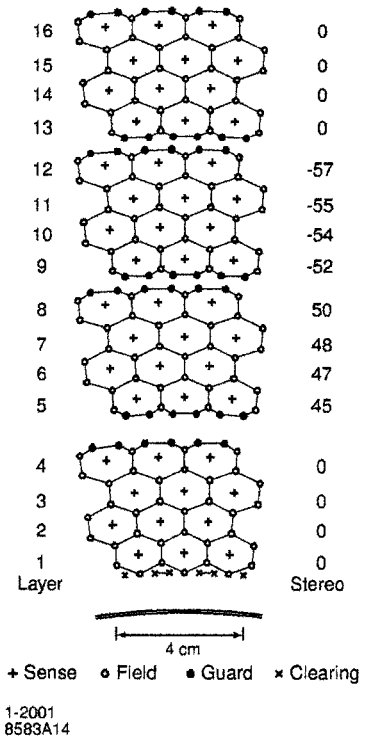

Figure 2.9: Schematic layout of drift cells for the four innermost superlayers. The numbers on the right side give the stereo angles (mrad) of sense wires in each layer.

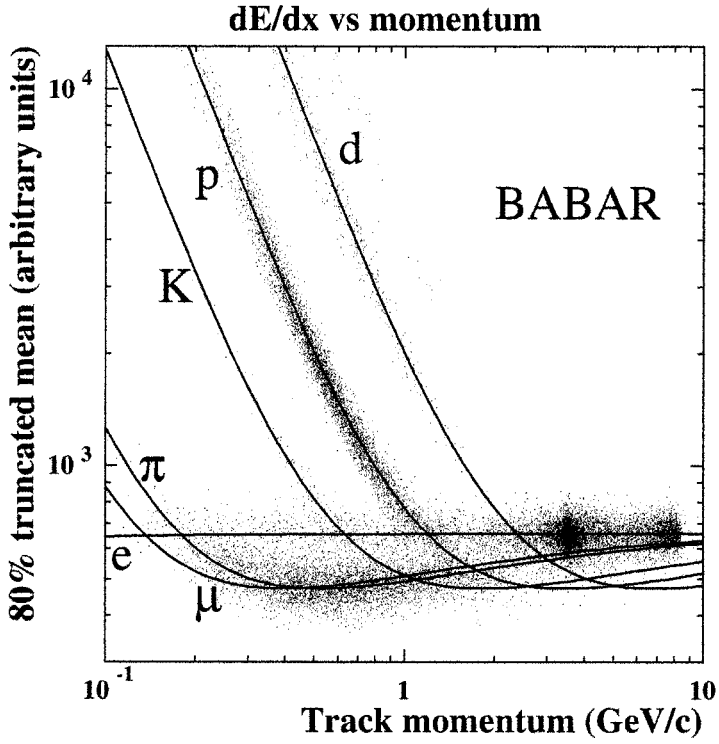

Figure 2.10: Energy loss ionization (dE/dx) in the DCH is shown as a function of track momentum. The solid lines indicates the Bethe-Bloch predictions.

2.2.3 Detection of Internally Reflected Cherenkov light (DIRC)

The DIRC is placed next to the DCH and it has 144 silica bars which are about 0.02m thick and 4.9m long. The DIRC is designed for PID of charged particles with momentum of 0.7 $\frac{GeV}{c}$ or above. Particle identification below 700 MeV/c relies on SVT and DCH.

The DIRC is designed on the principle that reflection from a flat surface preserves angular magnitudes. The quartz bars of the DIRC serve both as radiators and as light pipes. The photon multiplying tubes(PMTs) are placed at the backward end where it does not compete for space with other front-end detecting components.

The DIRC is based on the concept of Cherenkov radiation. A charged particle traveling faster than light in an optically dense medium will emit a light with an angle θ_c depending on its velocity in the medium. $Cos(\theta_c) = \frac{1}{n\beta}$, where $n = 1.473$ is the reflection index of the medium. The photon created by a charged particle will be reflected inside the quartz bars and reach the PMTs.

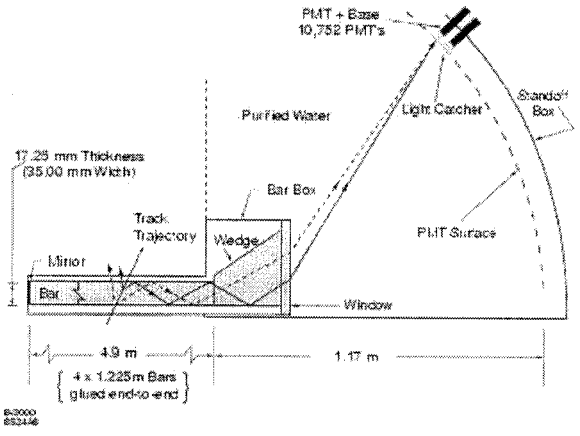

Figure 2.11: DIRC geometry.

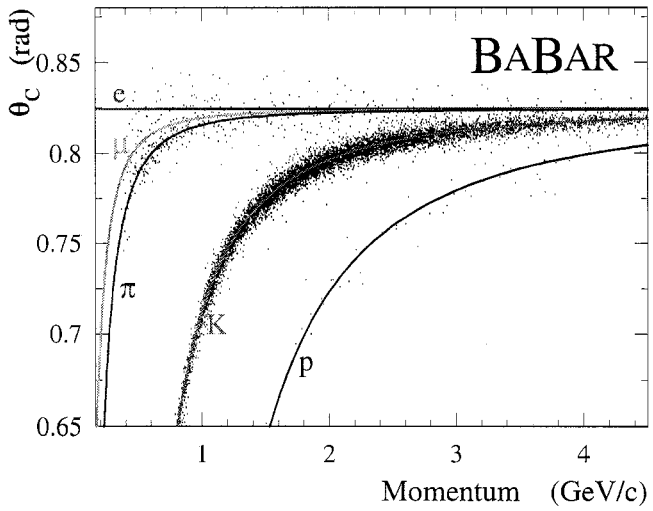

Figure 2.12: Cherenkov angle as a function of momentum.

2.2.4 Electromagnetic Calorimeter (EMC)

The EMC is made of 6580 CsI(Tl) crystals with lengths between 29.6 to 32.4cm. The barrel section of EMC has 5760 CsI(Tl) crystals in 48 rings and the end-cap section has 820 CsI(Tl) crystals in eight rings. The radiation length of the CsI(Tl) crystal is 1.85 cm.

The radiation length of the CsI(Tl) crystal is 1.85 cm. If charged particles or photons enters to CsI crystals, electromagnetic showers are created through ionization, pair production, Bremsstrahlung, Compton scattering and the photoelectric effect. To maximize the incoming energy of the charged particles or photons to relatively long electromagnetic wavelength photons, which are detected with silicon photodiodes, as CsI(TI) crystal is chosen. The relatively long electromagnetic waves are produced by excitation and de-excitation of the thallium ions in the crystal lattice.

The energy resolution of EMC is given by $\frac{\sigma_E}{E}$, where σ_E is the RMS error in the energy measurement. By using π^0 and μ decays, the angular resolution of the EMC is determined. The angular resulution ($\sigma\theta$) is between 3 (at high energy) to 12 mrad (at low energy).

2.2.5 Instrumented Flux Return (IFR)

The IFR is *BABAR*ś outermost subdetector. IFR has two different main purposes, as a muon and neutral hadron detector, and as a flux return for the magnetic solenoid which by itself is not a particle detector. The flux return is made of layers of iron and steel, with active detectors between each layer to detect the passage of particles (or of showers generated in the IFR layers).

At the beginning of the experiment, all of the layers were made of iron and

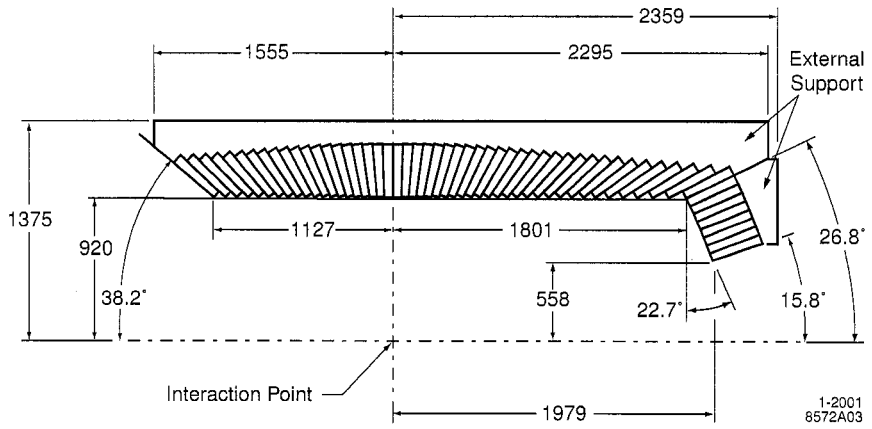

Figure 2.13: EMC geometry is shown. Lengths are given in mm.

all of the active detectors were RPCs. Hovewer, rapid aging and efficiency loss of the original RPCs forced upgrades and replacements in the forward endcap and barrel. In the summer of 2002 the original RPCs were replaced by new RPCs and 2 additional absorption lengths of absorber (brass in 5 IFR gaps and more external steel layers). In 2004, 2 of the IFR RPC sextants were replaced by LSTs and a brass absorber. The remaining 4 RPC sextants in the barrel were replaced by LSTs in the fall of 2006. Each of the LST sextants contains 12 layers of LSTs and 6 layers of brass absorber.

The IFR detects muons and long-lived neutral hadrons. The IFR is made of layers of Resistive Plate Chambers (RPC) and Limited Streamer Tubes (LST) placed between layers of steel of increasing thickness.

2.2.6 The superconducting Selenoid

The superconducting solenoid is located between the EMC and the IFR. Without a magnetic field, a tracking device could measure only position but not charge or

momentum of a particle. When a magnetic field is present, the charged tracks curve, and the charge and momentum of the particle can be determined from the direction and curvature of the track.To achieve good momentum resolution without increasing the tracking volume , the magnetic field is set at 1.5T.

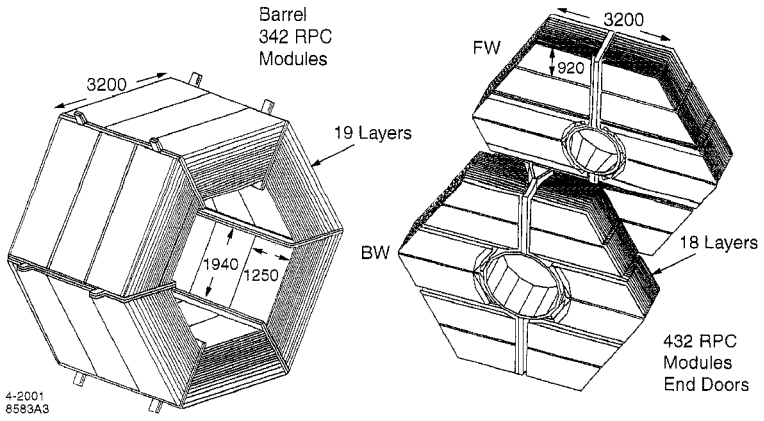

Figure 2.14: On the left barrel RPC modules, on the right forward (FW) and backward(BW) end door RPC modules are shown.

Chapter 3

Particle Identification

For the track finding and fitting Kalman filter algorithm is used. This algorithm takes into account the magnetic field and the detailed distribution of material in the detector. Charged tracks are defined by five parameters, which are ω, $tan\lambda$, d_0, ϕ_0 and z_0, and their assoc iated error matrix. These parameters are measured at the point of closest approach (POCA) to the z-axis. d_0 and z_0 are the distances of this poin t from the origin of the coordinate system in the x-y plane and along the z-axis, respectively. $\omega = \frac{1}{p_t}$ is the curvature of the track, λ is dip angle relative to the transverse plane, ϕ_0 is the azimuthal angle of the track.

3.1 Charged Particle Identification

We can only detect protons, kaons, pions, electrons and muons since they are sufficiently long-lived particles to leave a track in the detector. All oth er particles decay to those long-live particles before reaching any subdedectors. Charged particle candidates are identified by measuring energy loss $\frac{dE}{dx}$ in the SVT and DCH together

with information from the DIRC. The Bethe-Bloch equation [?] describes energy loss $\frac{dE}{dx}$ as a function of th e particles kinematic properties and the detector make-up.

$\frac{dE}{dx} = 4\pi r_e^2 m_e c^2 N_A \frac{Z}{A} \frac{1}{\beta^2} [\frac{1}{2} ln(\frac{2m_e c^2 \gamma^2 \beta^2 T_{max}}{I^2} - \frac{\delta}{2})]$

r_e and m_e are the electron's classical radius and mass, c is the speed of light, N_A is Avogadro's number,z is the charge of incoming part icle, A is the atomic weight of the absorber, β and γ are the relativistic quantities of the incoming particle, I is the mean excitation en ergy, and δ is the effect correction.

For each particle hypothesis a likelihood (L) is calculated using the following formula:

$L = L_{SVT} \times L_{DCH} \times L_{DIRC}$

where L_{SVT}, L_{DCH} and L_{DIRC} are SVT, DCH and DIRC likelihoods respectively.

3.1.1 SVT Likelihood Calculation

The likelihood for the SVT is calculated from an asymmetric Gaussian function.

$L_{SVT} = e^{(\frac{(ln((\frac{dE}{dx})meas) - ln((\frac{dE}{dx})expe))^2}{2\sigma\sqrt{\frac{5}{N}}})}$

N is the number of SVT layers. $\sigma = \sigma_L$ for $\frac{dE}{dx} < (\frac{dE}{dx})mod$ and $\sigma = \sigma_R$ for $\frac{dE}{dx} > (\frac{dE}{dx})mod$. The left-side (σ_L) and right-side standard deviations (σ_R) of the asymmetric Gaussian are fixed to values in control samples. $(dEoverdx)_{expe}$ is the expected energy loss.

A minimum 3 out of 5 SVT layer hits is required to provide $\frac{dE}{dx}$ information, otherwise the same L_{SVT} value is assigned to all particle type s. To moderate the effects of the Landau fluctuations, only the smallest 60% of the $(\frac{dE}{dx})$ values are used to calculations. For 5 samples, the lowest 3 values are used for average $\frac{dE}{dx}$. A modified Bethe-Bloch equation is used since the truncation algorithm is applied to

find $\frac{dE}{d\ x}$.

3.1.2 DCH Likelihood Calculation

The L_{DCH} is calculated using a symmetric Gaussian function.

$L_{DCH} = e^{(\frac{(ln((\frac{dE}{dx})meas)-ln((\frac{dE}{dx})expe))^2}{2\sigma})}$

where σ is a function of the measured mean, the number of samples, the RMS of the$\frac{dE}{dx}$ values and the track hypothesis. To moderate the eff ects of Landau fluctuations, only the smallest 80 % of the samples are used.

3.1.3 DIRC Likelihood Calculation

The L_{DIRC} is calculated by multiplying a Gaussian distribution for the measured Cerenkov angle and a Poison distribution for the measured number of pro tons. H

$L_{DIRC} = \frac{1}{\sqrt{2\pi\sigma_c}} \times \frac{e^{(\theta_c^{expe}-\theta_c^{meas})^2}}{2\sigma_c} \times \frac{e^{-N^{expe}}(N^{expe})^{N^{meas}}}{N^{meas}!}$

The N_{meas} is measured number of photons and N_{expe}, the expected number of photon, is taken from a calibration table created using reconstructed tr acks. Measured Cerenkov angle, θ_c^{meas}, and σc are calculated by fitting the ring of photons observed in the DIRC PMTs. The θ_c^{expe}, expected Cerenkov angle, is found using the track momentum at the entrance to the DIRC and the track mass hypothesis.

3.2 Proton Identification

Whether it is proton, pion or kaon likelihood selector there are four different strength levels: VeryLoose, Loose, Tight and VeryTight. In the proton like lihood selector, a particle's probability of being a proton is defined by comparing proton, pion and kaon likelihoods as shown in Table 3.1.

Table 3.1: Proton L Selector levels

pLHSelectors	$\frac{L(p)}{L(p)+L(\pi)}$	$\frac{L(K)}{L(K)+L(p)}$	Reject
pLHVeryLoose	> 0.5	< 0.75	-
pLHLoose	> 0.5	< 0.3	$p < 0.75$ GeV/c or not eLHTight
pLHTight	> 0.75	< 0.2	$p < 0.75$ GeV/c or not eLHTight
pLHVeryTight	> 0.96	< 0.1	$p < 0.75$ GeV/c or not eLHTight

3.3 Kaon Identification

In the kaon likelihood selector, a particle's probability of being kaon is defined by comparing proton, pion and kaon likelihoods as shown in Table 3.2.

Table 3.2: Kaon LH Selector levels

KLHSelectors	$\frac{L(K)}{L(K)+L(\pi)}$	$\frac{L(K)}{L(K)+L(p)}$	Reject eLHTight
KLHVeryLoose	> 0.50	> 0.02	-
KLHLoose	> 0.82	> 0.02	$p < 0.40$ GeV/c or not eLHTight
KLHTight	> 0.90	> 0.2	$p < 0.40$ GeV/c or not eLHTight
KLHVeryTight	> 0.90	> 0.2	$p < 0.40$ GeV/c or not eLHTight

3.4 Pion Identification

In the pion likelihood selector, a particle's probability of being pion is defined by comparing proton, pion and kaon likelihoods as shown in Table 3.3.

3.4.1 s9s25

s9s25 is the energy sum of the 3x3 crystal block (with the most energetic crystal in its center), divided by the energy sum of the 5x5 crystal block (with the most

Table 3.3: Pion LH selector levels

piLHSelectors	$\frac{L(K)}{L(K)+L(\pi)}$	$\frac{L(p)}{L(p)+L(\pi)}$	Reject eLHTight
piLHVeryLoose	< 0.98	< 0.98	-
piLHLoose	< 0.82	< 0.98	eLHTight
piLHTight	< 0.50	< 0.98	eLHTight
piLHVeryTight	< 0.20	< 0.50	eLHTight

energetic crystal in its center). This cut help distinguish between hadronic and electromagnetic showers at EMC thus we reduce the background.

3.4.2 Lateral Moment

To separate electromagnetic from hadronic showers in the calorimeter, the lateral energy distribution LAT of each bump is considered. It is defined as

$$LAT = \frac{\sum_{i\geq 3} E_i r_i^2}{E_1 r_0^2 + E_2 r_0^2 + \sum_{i\geq 3} E_i r_i^2}$$

E_i represents the energy deposited in the i'th crystal after having sorted the crystals by deposited energy:

$E_1 > E_2 > E_3 > ...$

r_i is the distance between the center of the i'th crystal and the bump position. $r_0 = 5$ cm is a measure of the distance between two crystals.

For electromagnetic showers, most of the energy is typically contained in two to three crystals, while hadronic showers spread out over greater distances. Since the sum in the numerator of the LAT equation (above) omits the two highest energies, LAT is typically small for electromagnetic showers and larger fo r hadronic showers.

3.4.3 X_p Cut

In order to suppress combinatorial and $B\bar{B}$ background, we require Ω_c^* candidates to have a scaled momentum:

$$X_p = \frac{p*(\Omega_c^*)}{p^*_{max}} = \frac{p*(\Omega_c^*)}{\sqrt{\frac{s}{4}-M^2}} => 0.5$$

where p* and M are the momentum and invariant mass of the reconstructed Ω_c^* candidate, respectively, and $\sqrt{s}$ is the total e^+e^- beam ener gy in the center of mass frame. Figure 3.1 shows the X_p distribution of Ω_c^* in signal Monte Carlo.

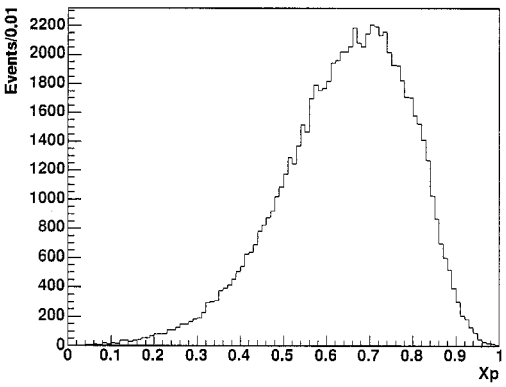

Figure 3.1: The X_p distribution of Ω_c^* is shown in signal MC.

Chapter 4

Data Analysis

The Ω_c^* baryons decays to Ω_c^0 and a γ. Ω_c^* candidates are reconstructed through the following decay channels:

- $\Omega_c^0(\Omega^-\pi^+)\gamma$ ... C1,
- $\Omega_c^0(\Omega^-\pi^+\ \pi^0)\gamma$ ... C2,
- $\Omega_c^0(\Omega^-\pi^+\ \pi^-\ \pi^+)\gamma$ ... C3,
- $\Omega_c^0(\Xi^-K^-\ \pi^+\ \pi^+)\gamma$ ... C4.

4.1 Data and Monte Carlo Samples

We use CM2 converted data processed with analysis-24. Monte Carlo(MC) samples are used for estimation of signal detection efficiencies, optimization of cuts and background studies. The MC simulation is based on Geant4 [1].

4.1.1 MC Samples

To optimize the Ω_c^* selection cuts, we use Ω_c^* signal MC and Ω^- skim $c\bar{c}$ MC, which was assigned a Ω_c^* mass value of 2800 MeV as shown in Table 4.1. In this MC the Ω_c^0 has two peak mass values of 2697.5 and 2704 MeV, corresponding to SP6 and SP5, respectively. These 2 different Ω_c^0 values in Ω_c^* MC give a wider resolution for Ω_c^0 and Ω_c^* which is a problem. After observing Ω_c^* in data we were suggested by the Charm AWG(David Williams and Bill Dunwoodie) to request new signal MC with new observed Ω_c^* peak mass value. To produce the new Ω_c^* signal MC, the Ω_c^* and Ω_c^0 peak mass values are fixed to 2764 MeV and 2697.5 MeV, correspondingly. Final Efficiencies are determined using the new Ω_c^* signal MC.

Table 4.1: MC Samples.

MC Samples	Number of Events	Luminosity (fb^{-1})
$c\bar{c}$ Ω^-skim	472158	322
$c\bar{c}$ Ξ^-skim	4648347	322
C1 signal MC	774K	N/A
C2 signal MC	456K	N/A
C3 signal MC	460K	N/A
C4 signal MC	466K	N/A

4.1.2 Data Samples

The data set used in this work has 230.7 fb^{-1} integrated luminosity recorded with the *BABAR* detector at the PEP-II storage ring from October 1999 until July 2005. This data set includes 209.1 fb^{-1} collected at $\Upsilon(4S)$ (On-resonance) and 21.6 fb^{-1} collected 40 MeV below (Off-resonance). To reduce time to reconstruct Ω_c^* events,

we use Ω^- and Ξ^- data and MC skims which were created by the University of Iowa.

Table 4.2: Ω^- and Ξ^- data skim samples.

Data Sample	Ω^- candidates	Ξ^- candidates	Luminosity (fb^{-1})
On-Peak Run1	114238	1005560	19.49
Off-Peak Run1	7998	82507	2.33
On-Peak Run2	375521	3215160	58.44
Off-Peak Run2	25650	252849	6.91
On-Peak Run3	208408	1756319	31.19
Off-Peak Run3	9409	90521	2.37
On-Peak Run4	769444	6326655	99.94
Off-Peak Run4	43249	403675	10.00
Total On-Peak	1467611	12303694	209.06
Total Off-Peak	86309	829552	21.61
Overall Total	1553920	13133246	230.67

4.1.3 Fit Functions

We use root and *BABAR* roofit packages to perform the fits. To fit Ω_c^* signal MC shape we use Crystal Ball Function. For background parametrization, we use a threshold function times a 4th order polynomial.

Crystal Ball Function

The Crystal Ball function [30] uses the NaI line shape as obtained by the Crystal Ball experiment. It has the following form:

$N \times \exp(-\frac{(x-\bar{x})^2}{2\times\sigma^2})$ For $\frac{(\bar{x}-x)}{\sigma} > \alpha$

$N \times \ A \times (B - \frac{x-\bar{x}}{\sigma})^{-n}$ For $\frac{(\bar{x}-x)}{\sigma} \leq \alpha$.

where $A \equiv (\frac{n}{|\alpha|})^n \times exp(-\frac{|\alpha|^2}{2})$ and $B \equiv \frac{n}{|\alpha|} - |\alpha|$

- N is a normalization factor.
- $\bar{x}$ is the peak value of the Gaussian portion of the function.
- σ is the width of the Gaussian portion of the function.
- α is the point at which the function changes to the power function.
- n is the exponent of the power function.
- A and B are defined such that the function and its first derivative are continuous at α.

Threshold Function

For the background modeling from $c\bar{c}$ MC we use a threshold function multiplied with 4th order polynomial function as described in BAD 1345 [29].

$$S_2(m) = \frac{1}{m^2}\sqrt{(m^2 - (m_1 + m_2)^2)(m^2 - (m_1 - m_2)^2)}$$

where m is the Ω_c^* mass, m_1 and m_2 are the Ω_c^0 and the γ masses, which means $m_2 = 0$. Thus we get

$$S_2(m) = \frac{m^2 - m_1^2}{m^2}$$

The Background pdf $P_b(m, a)$ is defined as

$P_b(m,a) = 0$ for $m \leq m_1$,

$P_b(m,a) = S_2(m)P_4(m-m_1,a)$ for $m > m_1$

where $P_4(x,a) = 1 + a_1x + a_2x^2 + a_3x^3 + a_4x^4$.

4.1.4 Pre-Selection Cuts

In this analysis we use the Ω^- and the Ξ^- skims which come with pre-selection cuts. Particle ID (Very-Loose likelihood) is used for the proton daughter of the Λ^0 and for the kaon daughter of the Ω^-. No flight length cuts are used. The Ω^- skim is created with the following preselection cuts;

- Λ^0 mass cut: $|M_{\Lambda^0} - M_{\Lambda^0(PDG)}| < 10MeV$.
- Λ^0 is mass-constrained.
- Λ^0 vertex χ^2 probability cut: > 0.0.
- Ω^- mass cut: $|M_{\Omega^-} - M_{\Omega^-(PDG)}| < 10MeV$.
- Ω^- vertex χ^2 probability cut: > 0.001.

The Ξ^- skim is created with the following preselection cuts:

- Λ^0 mass cut: $|M_{\Lambda^0} - M_{\Lambda^0(PDG)}| < 10MeV$.
- Λ^0 is mass-constrained.
- Λ^0 vertex χ^2 probability cut: > 0.0.
- Ξ^- mass cut: $|M_{\Xi^-} - M_{\Xi^-(PDG)}| < 10MeV$.
- Ξ^- vertex χ^2 probability cut: > 0.001.

For γ candidates we use the GoodPhotonLoose which has the following preselection cuts:

- Min Raw Energy: 0.030 GeV.
- Max Lateral Moment: 0.8.

For π^0 candidates we use the pi0VeryLoose list which has the following preselection cuts:

- photon list: GoodPhotonLoose.
- Lower energy γ Cut: 0.030 GeV.
- Max Lateral Moment: 0.8.
- π^0 lower mass cut: 0.090 GeV.
- π^0 upper mass cut 0.165 GeV.

4.2 Optimization Procedure

The final event selections are chosen to give the optimal significance, defined as $\frac{S}{\sqrt{B}}$where S is the number of signal events estimated from signal MC and B is the number of background events obtained from Ω^- and Ξ^- $c\bar{c}$ MC. We select $\pm 2.5\sigma$ Ω_c^* mass window from Ω_c^* peak value for optimization. Detailed study of optimization techniques can be found at [36].

Λ^0 Selection

In all 4 decay channels we have a Λ^0 in the final state where B($\Lambda^0 \rightarrow p\pi^-$ $63.9 \pm 0.5\%$). Λ^0 candidates are formed by combining oppositely charged protons

and pions.

For Λ^0 candidates we have the following selection cuts:

- Proton from pLHTight list.
- Pion from piLHTight list.
- Successfully vertexed with Treefitter.

By selecting protons as PLhTight and pions as PiLhTight we obtain the best $\frac{S}{\sqrt{B}}$ value, which is shown in appendix A, Table A.1.

The lifetime of the Λ^0 is 0.26 ns. It can travel 7.8 cm ($c \times \tau$) on average before decaying. A 3D flight length is calculated by using Ω^- and Λ^0 decay vertex points, and is chosen to be greater than 0.30 cm according to appendix A, Table A.1.

Another quantity used for the Λ^0 selection is Λ^0 decay vertex χ^2 with a cut value of less than 20 as detailed in appendix A, Table A.2. The Λ^0 invariant mass is fitted using two Gaussian (with the same mean) functions. The effective width (σ_{eff}) is calculated by using the following formula:

$$\sigma_{eff}^2 = f_1\sigma_1^2 + f_2\sigma_2^2$$

where f_1 and f_2 are fractions of the areas under Gaussian 1 and 2 respectively. σ_1 and σ_2 are the two widths from the Gaussian 1 and 2 respectively. After the Λ^0 selection we plot the Λ^0 in signal MC on the left side of Figure 4.1 and in data on the right side of Figure 4.1 and the result from the unbinned fit is overlayed.

Ω^- Selection

For Ω^- candidates we have the following selection cuts:

- Kaon from KLhVeryTight list.

- Successfully vertexed with Treefitter.

The reconstruction of Ω^- is performed by combining reconstructed Λ^0 and a K^- candidate using TreeFitter. Ω^- decays to Λ^0 and a K^- with a branching fraction of 67.8 $\pm$ 0.7 %. A Λ^0 mass window cut is used to reduce the background. We select a $\pm$ 3.8 MeV Λ^0 mass window from mean value. Appendix A, Table A.3 shows this study. As for the K^- selection, KLhVeryTight is selected as deatailed in appendix A, Table A.4. The Ω^- lifetime is 0.08 ns so it can travel 2.4 cm ($c \times \tau$) on average before decaying. A 3D flight length is calculated by using the Ω^- and Ω_c^0 decay vertex points. The selected flight length is greater than 0.25 cm from appendix A, Table A.5. Ω^- decay vertex χ^2 is chosen to be less than 30 from appendix A, Table A.6. After these cuts we plot the Ω^- in signal MC as shown in Figure 4.2. In Figure 4.3, the Ω^- invariant mass in data is fitted using two Gaussians (with the same mean) on the left, and with a single Gaussian on the right. For the background from data we use a first order polynomial.

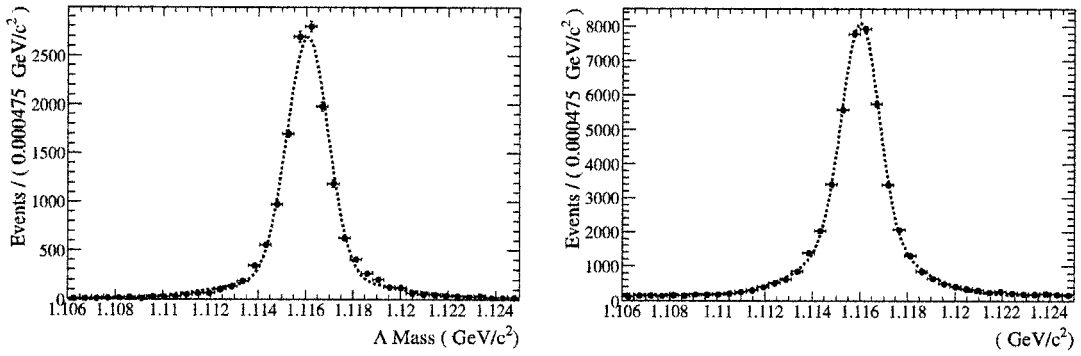

Figure 4.1: On the left , Λ^0 in signal MC for C1 is fitted with double Gaussians (the same mean). From the fit, the mean is 1116.06 $\pm$ 0.01 MeV, σ_1 is 0.86 $\pm$ 0.01 MeV, σ_2 is 3.44 $\pm$ 0.06 MeV. On the right, the same distribution in data is fitted with with double Gaussians (the same mean) and a first order polynomial for the background. From the fit, the mean is 1115.98 $\pm$ 0.01 MeV, σ_1 is 0.77 $\pm$ 0.01 MeV and σ_2 is 2.06 $\pm$ 0.01 MeV.

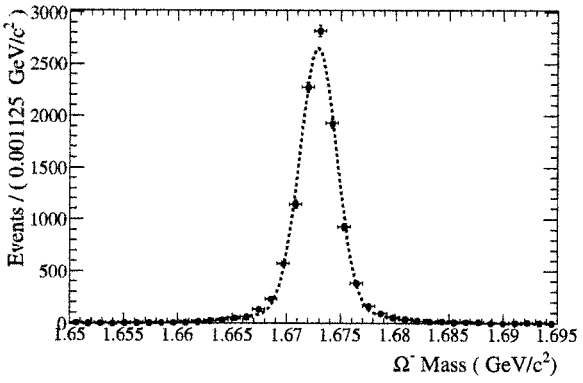

Figure 4.2: Ω^- in signal MC for C1 is fitted with double Gaussians (the same mean). From the fit, the mean is 1672.86 $\pm$ 0.02 MeV, σ_1 is 1.70 $\pm$ 0.02 MeV and σ_2 is 6.65 $\pm$ 0.18 MeV.

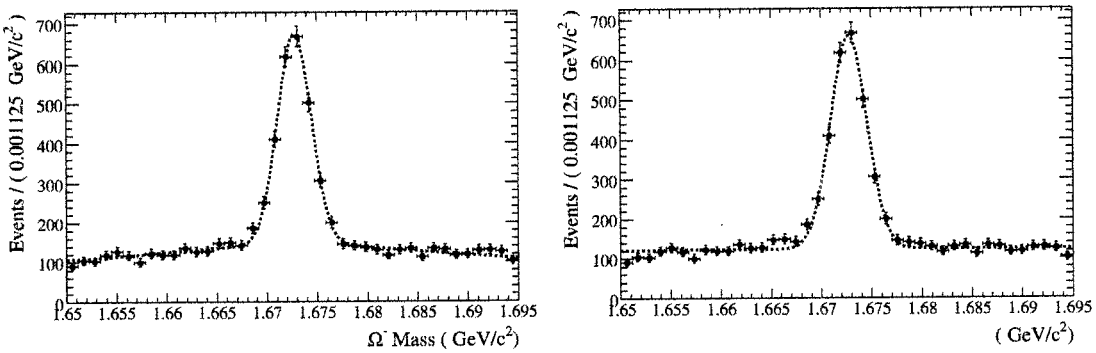

Figure 4.3: On the left, Ω^- in data for C1 is fitted with double Gaussians (the same mean) and with a first order polynomial for the background. From the fit, the mean is 1672.74 $\pm$ 0.05 MeV, σ_1 is 1.69 $\pm$ 0.06 MeV , σ_2 is 13.04 $\pm$ 9.12 MeV. On the right, the same distribution is fitted with a single Gaussian and a first order polynomial. From the fit, the mean is 1672.73 $\pm$ 0.05 MeV and σ is 1.81 $\pm$ 0.05 MeV.

Ξ^- Selection

For Ξ^- candidates we have the following selection cuts:

- Pion from PiLhVeryTight list.
- Successfully vertexed with Treefitter.

The reconstruction of the Ξ^- candidate is performed by combining reconstructed Λ^0 and a π^- candidate using TreeFitter. The Ξ^- decays to Λ^0 and π^- 99.887 $\pm$ 0.035 % of the time. A Λ^0 mass cut is used to lower the background. We select a $\pm$ 2.0 σ (3.8 MeV) Λ^0 mass window from the mean value. As for the π^- selection, PiLhVeryTight is selected as detailed in appendix A, Table A.24. The Ξ^- lifetime is 0.2 ns, and it can fly 6cm ($c \times \tau$) on average in the detector before decaying. A 3D flight length is calculated by using Ξ^- and Ω_c^0 decay vertex points. The selected flight length is greater than 0.25 cm is selected as shown in appendix A, Table A.25. Ξ^- decay vertex χ^2 is chosen to be less than 8 from appendix A, Table A.26. After these cuts we plot the Ξ^- in signal MC on the left side of Figure 4.4 and in data on the right side of figure 4.4 and the result from unbinned fit is overlayed. The Ξ^- invariant mass distribution is fitted with two Gaussians (with the same mean) functions. For the background from data we use a first order polynomial.

γ Selection

For γ candidates we have the following selection cuts:

- γ s from GoodPhotonLoose list.

To separate electromagnetic showers from hadronic ones in the calorimeter, the lateral moment(LAT) cut is selected. For electromagnetic showers, most of the energy is typically contained within two or three crystals, while hadronic showers

spread out over greater distances. LAT is typically small for electromagnetic showers and larger for hadronic showers. This cut study is summarized in appendix A, Table A.12. We select $0.6 > LAT > 0.01$.

The S9/S25 cut study: The energy sum of the 3x3 crystal block (s9) with the most energetic crystal in its center, divided by the energy sum of the 5x5 crystal block (S25) with the most energetic crystal in its center. s9/s25 cut study forγ is summarized in appendix A, Table A.11. We select s9/s25 > 0.9.

The final γ selection cut is on low energy photons to reduce the background further. In appendix A, Table A.13 this study is outlined. We select the γ s with energy greater than 80 MeV.

π^0 Selection

For π^0 candidates we have the following selection criteria:

- π^0 from pi0VeryLoose list.

π^0 candidates are reconstructed by combining 2 photons from GoodPhotonLoose list. We apply LAT cut for all γ candidates. The study of this cut is shown in Table A.15. The study of S9/S25 cut for γ is shown in appendix A Table A.16. We select $0.6 > LAT > 0.01$, s9/s25 > 0.9. To reduce the background further we cut very low energy photons. Study of this cut is in appendix A, Table A.17. We select γ s with energy greater than 80 MeV.

Ω_c^0 Selection

For Ω_c^0 candidates we have the following selection cuts:

- π^0 from pi0VeryLoose list.

- Pions from PiLhLoose list except for the c4 mode where we select PiLhTight list.
- Kaons from KLhTight list.
- Successfully vertexed with Treefitter.

The reconstruction of Ω_c^0 candidates is performed by combining selected Ω^- and a π^+ candidate using TreeFitter. An Ω^- mass window cut is used to reduce the background. We select a $\pm$ 5.2 MeV Ω^- ($\pm$ 6.0 MeV for Ξ^-). The mass window is centered around the Ω^- mean value.

Ω_c^0 pion PID selections for the decay channels c1 and c2 are outlined in Appendix A, Table A.8 and A.14, correspondinly. We select PiLhLoose. The pion PID for the decay channel c3 is summarized in Appendix A, Table A.20 and A.21. We select PiLhLoose. PID of c4 is outlined in Table A.28 and A.29. We select PiLhTight and KLhTight. For c2 we also apply all π^0 selection cuts. Next, we apply a $\pm$ 2.5 σ (12.5 MeV) π^0 mass window cut from π^0 mean mass value. After applying these selection cuts we plot the Ω_c^0 s in figures 4.5 and 4.6. We fit the distribution with a double Gaussian (with the same mean) except in the decay channel c2, where we use a single Gaussian. The results of the fits are shown in Table 4.3.

Table 4.3: Fit results of Ω_c^0 is shown for all decay channels in Ω_c^0 signal MC.

Decay ch.	Peak value (MeV)	σ_1 (MeV)	σ_2 (MeV)	σ_1 fraction (%)
c1	2698.65 $\pm$ 0.06	5.20 $\pm$ 0.11	10.82 $\pm$ 0.79	84.5
c2	2696.18 $\pm$ 0.34	12.06 $\pm$ 0.73	24.71 $\pm$ 2.73	73.6
c3	2697.73 $\pm$ 0.09	3.65 $\pm$ 0.12	11.88 $\pm$ 0.73	71.6
c4	2698.59 $\pm$ 0.09	4.72 $\pm$ 0.12	13.99 $\pm$ 1.07	81.9

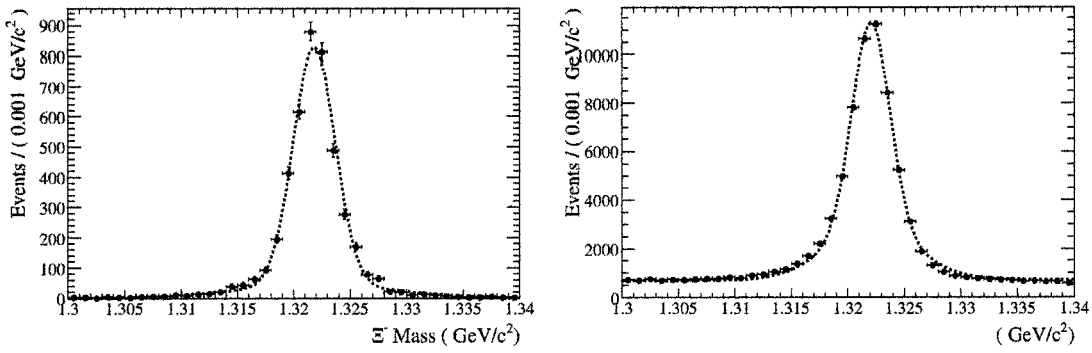

Figure 4.4: On the left, the Ξ^- in signal MC for C4 is fitted with double Gaussians(the same mean). From the fit, the mean is 1321.78 $\pm$ 0.03 MeV, σ_1 is 1.85 $\pm$ 0.04 MeV (with a fraction of 81.9 %), σ_2 is 7.17 $\pm$ 0.31 MeV and the effective sigma is calculated to be 3.45 MeV. On the right mean is 1322.00 $\pm$ 0.01 MeV, σ_1 is 1.66 $\pm$ 0.03 MeV (with a fraction of 63.5 %), σ_2 is 3.96 $\pm$ 0.12 MeV and the effective sigma is calculated to be 2.73 MeV.

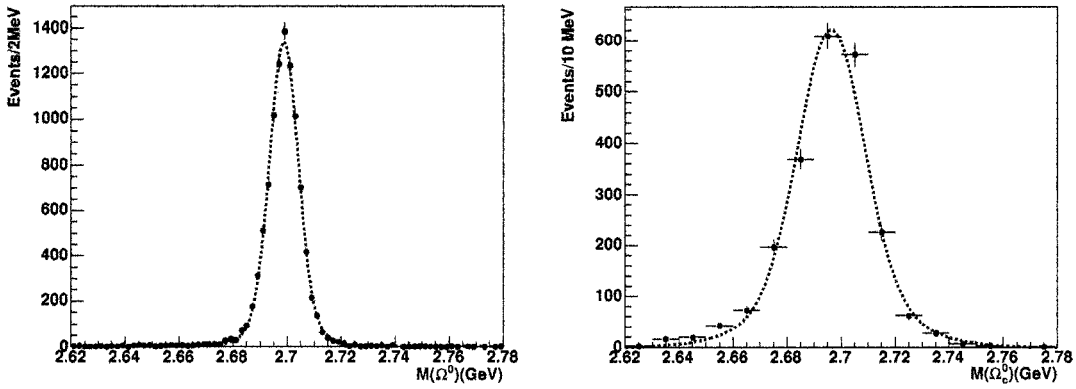

Figure 4.5: $\Delta\Omega_c^0$ distribution in signal MC for decay channel c1 is shown on the left, and for decay channel c2 on the right. On the left the mean value is 2698.65 $\pm$ 0.06 MeV, σ_1 is 5.20 $\pm$ 0.11 MeV, σ_2 is 10.82 $\pm$ 0.79 MeV and the fraction of σ_1 is 84.5 %. On the right the mean value is 2696.18 $\pm$ 0.34 MeV, σ_1 is 12.06 $\pm$ 0.73 MeV, σ_2 is 24.71 $\pm$ 2.73 MeV and the fraction of σ_1 is 73.6 %.

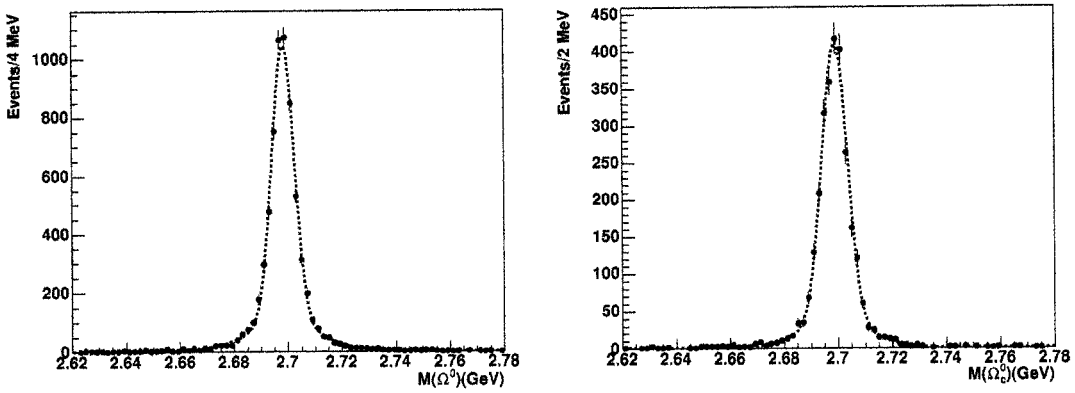

Figure 4.6: M (c3) distribution in signal MC in the decaychannel C3 is shown on the left, and M (c4) distribution decay channel C4 is shown on the right. On the left the mean value is 2697.73 $\pm$ 0.09 MeV, σ_1 is 3.65 $\pm$ 0.12 MeV, σ_2 is 11.88 $\pm$ 0.73 MeV and the fraction of σ_1 is 71.6 %. On the right the mean value is 2698.59 $\pm$ 0.09 MeV, σ_1 is 4.72 $\pm$ 0.12 MeV, σ_2 is 13.99 $\pm$ 1.07 MeV and the fraction of σ_1 is 81.9 %.

Ω_c^* Selection

Reconstruction of Ω_c^* is performed by combining selected Ω_c^0 with a γ candidate. γ selection cuts were given in section 3.3.5. To reduce the background we use a $\pm$ 15 MeV for 1st, 3rd and 4th channel, $\pm$ 33 MeV for 2nd channel Ω_c^0 mass cut around the Ω_c^0 mean mass value. The study of these cuts is outlined in Appendix A, Table A.10, A.19, A.23 and A.29 for each channel. After all the selections we plot the Ω_c^* - Ω_c^0 + 2.6975($\Delta\Omega_c^*$) in Figures 4.7 and 4.8. For fitting we use roofit (unbinned maximum likelihood fits). The Ω_c^* distribution is fitted with the crystal ball function. Fit results are given in Table 4.4.

Table 4.4: Fit results of the $\Delta\Omega_c^*$ distributions are shown for all decay channels in signal MC.

Decay ch.	Peak value (MeV)	Sigma (MeV)	Generator level Ω_c^* mass (MeV)
C1	2763.76 $\pm$ 0.07	4.04 $\pm$ 0.07	2764
C2	2763.68 $\pm$ 0.12	4.24 $\pm$ 0.11	2764
C3	2763.87 $\pm$ 0.07	4.04 $\pm$ 0.06	2764
C4	2763.94 $\pm$ 0.12	4.03 $\pm$ 0.11	2764

4.3 Signal Detection Efficiency Studies

The detection efficiency is defined as the number of reconstructed and truth matches Ω_c^* candidates using all selection cuts divided by the number of generated $\Omega_c^* s$ with $X_p(\Omega_c^*) > 0.5$ cut only.

The selection criteria for Λ^0 , Ω^- , Ξ^- , Ω_c^0 and Ω_c^* are described above in this chapter. Table 4.5, 4.6, 4.7 and 4.8 give the subsequent efficiencies after each

cuts for decay modes C1, C2, C3 and C4, correspondly. We use roofit packages for fitting. After setting all cuts , we plot the Ω_c^* in signal MC in Figures 4.7 and 4.8.

Table 4.5: Signal detection efficiency Table for the decay mode C1.

Selection Cuts	Cut Values	Efficiency
Preselection cuts only		21.7 %
Λ^0Proton and Pion PID	PiLhTight and PLhTight	20.7%
Λ^0 3D Flight Cut	> 0.3 cm	19.1 %
$\chi^2_{\Lambda^0 Vertex}$	< 20	17.4 %
Λ^0 Mass Cut	$\pm$ 2.0 σ	15.9 %
Ω^- Kaon PID	KLhVeryTight	14.1 %
Ω^- 3D flight Cut	> 0.25 cm	13.0 %
$\chi^2_{\Omega^- Vertex}$	< 30	12.3 %
Ω^- Mass Cut	$\pm$ 2.0 σ	11.4 %
Ω_c^0 Pion PID	PiLhLoose	11.2 %
$\chi^2_{\Omega_c^0 Vertex}$	< 15	10.2 %
Ω_c^0 Mass	$\pm$ 2.5 σ	8.9 %
γ s9s25	> 0.9	8.7 %
γ LAT	$0.01 <$ LAT < 0.6	7.6 %
γ Energy	> 80 MeV	5.7 %

4.4 Background Studies with $c\bar{c}$ MC

For the first, second and third decay channels we use 472,158/417,920,626 (Ω^- skim $c\bar{c}$ MC events/total $c\bar{c}$ MC events) Ω^- $c\bar{c}$ MC events, for the 4th decay channel we use 4,648,347/417,920,626 (Ξ^- skim $c\bar{c}$ MC events/total $c\bar{c}$ MC events) Ξ^- $c\bar{c}$ MC events which correspond to 322 fb^{-1} of integrated luminosity.

We use Ω^- $c\bar{c}$ MC to study the background shapes in C1, C2, C3. For C4 we use Ξ^- $c\bar{c}$ MC. The selection of cuts were outlined in Tables 4.5, 4.6, 4.7 and 4.8

Table 4.6: Signal detection efficiency Table for the decay mode C2.

Selection Cuts	Cut Values	Efficiency
Preselection cuts only		11.2 %
Λ^0Proton and Pion PID	PiLhTight and PLhTight	10.7%
Λ^0 3D Flight Cut	> 0.3 cm	10.4 %
$\chi^2_{\Lambda^0 Vertex}$	< 20	10.0 %
Λ^0 Mass Cut	$\pm$ 2.0 σ	9.6 %
Ω^- Kaon PID	KLhVeryTight	9.0 %
Ω^- 3D flight Cut	> 0.25 cm	8.5 %
$\chi^2_{\Omega^- Vertex}$	< 30	8.2 %
Ω^- Mass Cut	$\pm$ 2.0 σ	7.8 %
Ω_c^0 Pion PID	PiLhLoose	7.6 %
π^0 γ LAT	$0.01 <$ LAT < 0.6	7.0 %
π^0 γ s9s25	> 0.9	6.6 %
π^0 γ Energy	> 80 MeV	5.9 %
π^0 Mass	$\pm$ 2.5 σ	5.5 %
$\chi^2_{\Omega_c^0 Vertex}$	< 15	5.1 %
Ω_c^0 Mass	$\pm$ 2.5 σ	4.4 %
γ s9s25	> 0.9	4.2 %
γ LAT	$0.01 <$ LAT < 0.6	3.5 %
γ Energy	> 80 MeV	2.0 %

for each channel. After applying selected cuts we plot the Ω_c^0 in Figure 4.9, 4.10, 4.11 and 4.12. We fit the $\Delta\Omega_c^*$ with a Crystal Ball function used to parametrize the signal, and a threshold function multiplied by a 4th order polynomial used for the background. The results of the fits are shown in Table 4.9.

Table 4.7: Signal detection efficiency Table for the decay mode C3.

Selection Cuts	Cut Values	Efficiency
Preselection cuts only		10.9 %
Λ^0Proton and Pion PID	PiLhTight and PLhTight	10.3%
Λ^0 3D Flight Cut	> 0.3 cm	9.9 %
$\chi^2_{\Lambda^0 Vertex}$	< 20	9.2 %
Λ^0 Mass Cut	$\pm$ 2.0 σ	8.6 %
Ω^- Kaon PID	KLhVeryTight	7.9 %
Ω^- 3D flight Cut	> 0.25 cm	7.1 %
$\chi^2_{\Omega^- Vertex}$	< 30	6.9 %
Ω^- Mass Cut	$\pm$ 2.0 σ	6.6 %
Ω_c^0 Pion PID	PiLhLoose	6.5 %
$\chi^2_{\Omega_c^0 Vertex}$	< 15	6.2 %
Ω_c^0 Mass	$\pm$ 2.5 σ	5.6 %
γ s9s25	> 0.9	5.3 %
γ LAT	$0.01 <$ LAT < 0.6	4.4 %
γ Energy	> 80 MeV	3.0 %

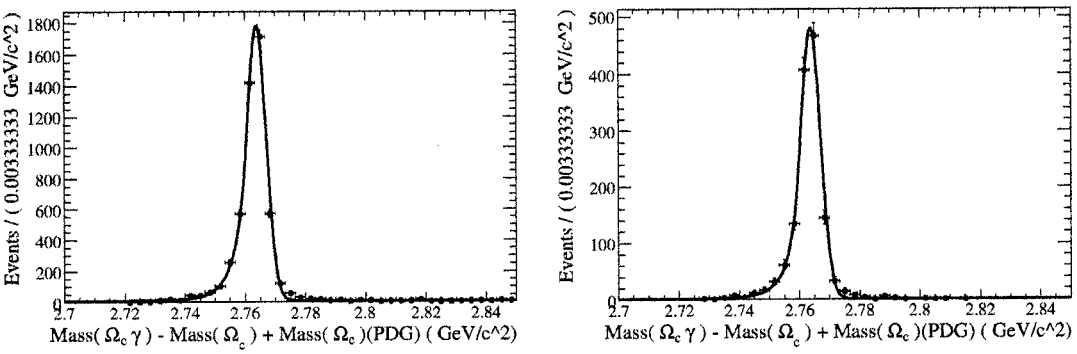

Figure 4.7: The $\Delta\Omega_c^*$ in signal MC for the decay channel C1 is shown on the left, and in the decaychannel C2 is shown on the right. The distribution is fitted with a Crystal Ball function and the results from the unbinned fit is overlayed. On the left the mean value is 2763.76 $\pm$ 0.07 MeV and σ is 4.04 $\pm$ 0.07 MeV. On the right the mean value is 2763.68 $\pm$ 0.12 MeV and σ is 4.24 $\pm$ 0.11 MeV.

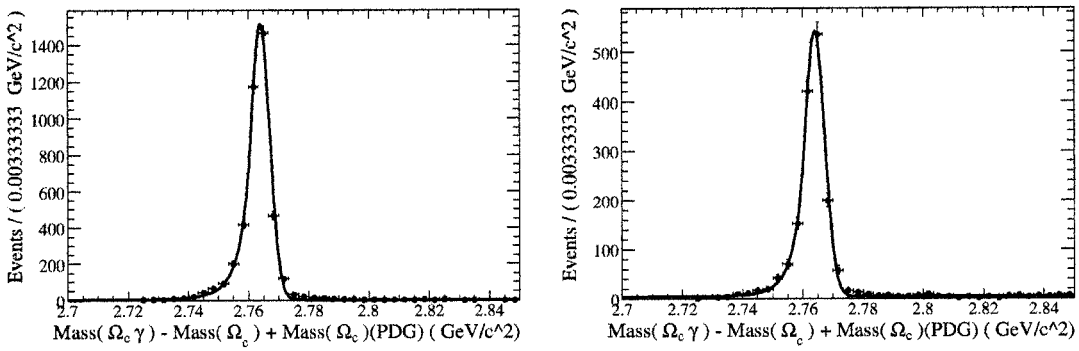

Figure 4.8: The $\Delta\Omega_c^*$ distribution in signal MC in the decaychannel C3 is shown on the left, and in the decaychannel C4 is shown on the right. The distribution is fitted with a Crystal Ball function. On the left the mean value is 2763.87 $\pm$ 0.07 MeV and σ is 4.04 $\pm$ 0.06 MeV. On the right the mean value is 2763.94 $\pm$ 0.12 MeV and σ is 4.03 $\pm$ 0.11 MeV.

Table 4.8: Signal detection efficiency Table for the decay mode C4.

Selection Cuts	Cut Values	Efficiency
Preselection cuts only		11.0 %
Λ^0Proton and Pion PID	PiLhTight and PLhTight	10.2%
Λ^0 3D Flight Cut	> 0.3 cm	10.0 %
$\chi^2_{\Lambda^0 Vertex}$	< 20	8.9 %
Λ^0 Mass Cut	$\pm$ 2.0 σ	8.0 %
Ξ^- Pion PID	PiLhVeryTight	7.9 %
Ξ^- 3D flight Cut	> 0.25 cm	7.4 %
$\chi^2_{\Xi^- Vertex}$	< 30	5.8 %
Ξ^- Mass Cut	$\pm$ 2.0 σ	5.6 %
Ω_c^0 PID	PiLhTight and KLhTight	5.2 %
$\chi^2_{\Omega_c^0 Vertex}$	< 15	4.6 %
Ω_c^0 Mass	$\pm$ 2.5 σ	3.8 %
γ s9s25	> 0.9	3.6 %
γ LAT	$0.01 <$ LAT < 0.6	3.2 %
γ Energy	> 80 MeV	2.5 %

Table 4.9: Fit parameters of $\Delta\Omega_c^*$ is shown for all the decay channels in $c\bar{c}$ MC.

Decay channel	Peak value (MeV)	Sigma (MeV)	Number of Events
C1	2797.4 $\pm$ 1.1	4.0 (fixed)	78.3 $\pm$ 14.0
	2796.4 $\pm$ 1.4	5.3 $\pm$ 1.3	86.5 $\pm$ 19.4
C2	2798.4 $\pm$ 1.5	4.2 (fixed)	51.5 $\pm$ 13.9
	2795.5 $\pm$ 2.8	7.5 $\pm$ 2.5	75.6 $\pm$ 25.8
C3	2797 (fixed)	4.0 (fixed)	13.0 $\pm$ 5.7
C4	2797 (fixed)	4.0 (fixed)	24.6 $\pm$ 18.5

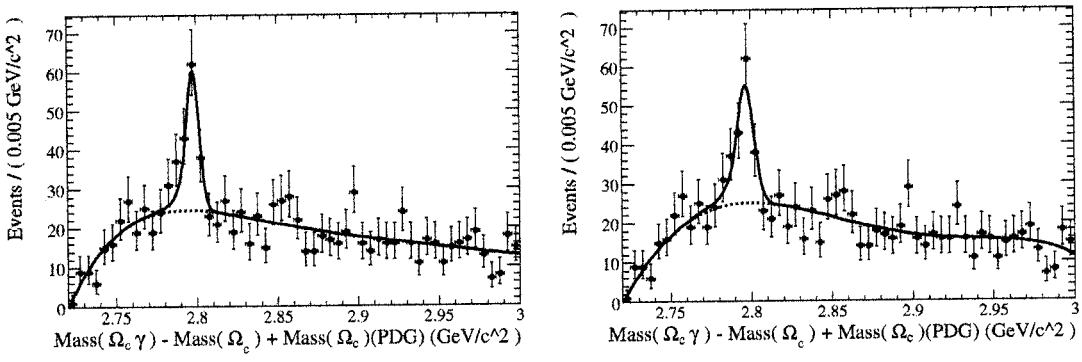

Figure 4.9: $\Delta\Omega_c^*$ in $c\bar{c}$ MC for the decay channel C1 is shown on the left with fixed σ. The same channel is shown on the right with released σ. On the left, the mean value is 2797.4 $\pm$ 1.1 MeV, σ is fixed to 4.0 MeV and the yield is 78.4 $\pm$ 14.0 events. On the right, the mean value is 2796.4 $\pm$ 1.4 MeV, σ is 5.3 $\pm$ 1.3 MeV and the yield is 86.5 $\pm$ 19.4 events.

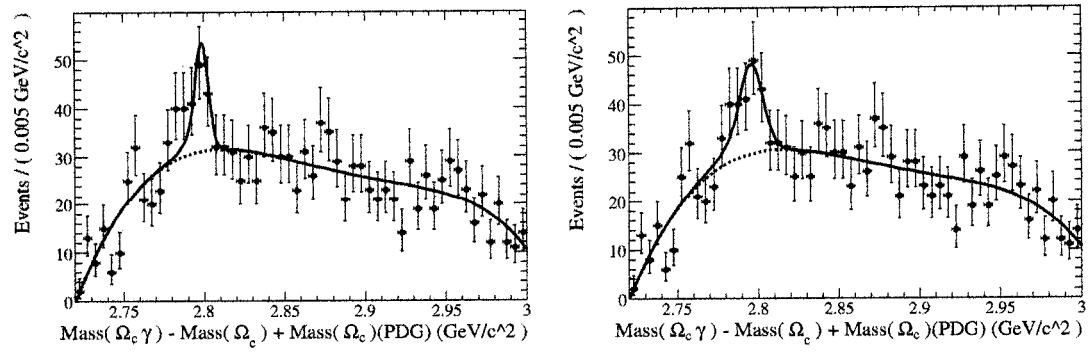

Figure 4.10: $\Delta\Omega_c^*$ in $c\bar{c}$ MC in the decaychannel C2 is shown on the left with fixed σ. The same channel is shown on the right with released σ. On the left, the mean value is 2798.4 $\pm$ 1.5 MeV, σ is fixed to 4.2 MeV and the yield is 51.5 $\pm$ 13.9 events. On the right, the mean value is 2795.5 $\pm$ 2.8 MeV, σ is 7.5 $\pm$ 2.5 MeV and the yield is 75.6 $\pm$ 25.8 events.

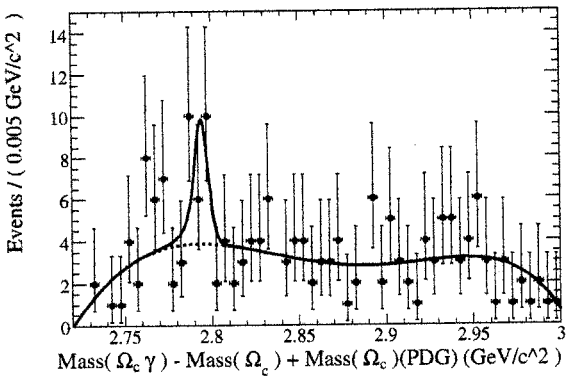

Figure 4.11: $\Delta\Omega_c^*$ in $c\bar{c}$ MC in the decaychannel C3 is shown. The mean value is fixed at 2797.0 MeV, σ is fixed to 4.0 MeV and the yield is 13.0 $\pm$ 5.7 events.

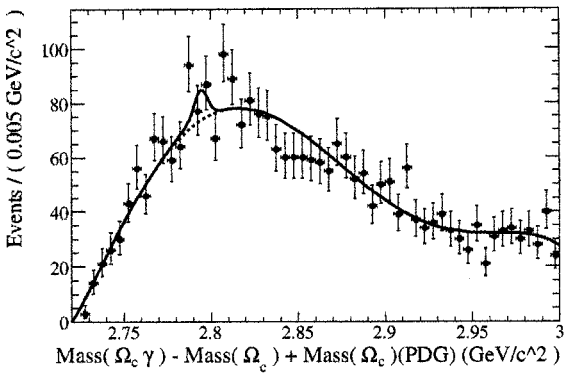

Figure 4.12: $\Delta\Omega_c^*$ in $c\bar{c}$ MC in the decaychannel C4 is shown with fixed σ and mean. The mean value is fixed at 2797.0 MeV, σ is fixed to 4.0 MeV and the yield is 24.6 $\pm$ 18.5 events.

4.4.1 Peaking Background

We check for the existence of peaking background in $c\bar{c}$ MC. After all our selection cuts we see an $\Delta\Omega_c^*$ signal which has a yield of 78.4 $\pm$ 14.0 events in the decay mode C1 (Figure 4.9). Then we check $c\bar{c}$ MC with the truth information. With a truth veto (we reject true Ω_c^* events) the $\Delta\Omega_c^*$ distribution is shown in Figure 4.13. We do not see any hint of peaking background signal therefore there is no peaking background.

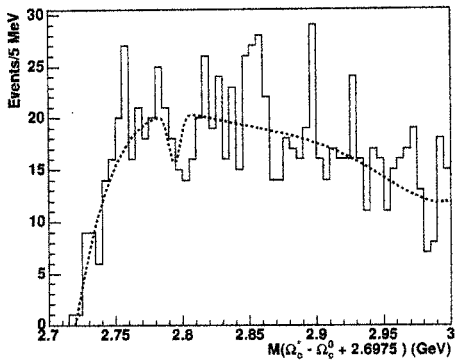

Figure 4.13: $\Delta\Omega_c^*$ in $c\bar{c}$ MC in the decaychannel C1 is shown. The Ω_c^* events in the MC have been removed by a truth veto.

4.5 Data Study

In this section we use unbinned maximum likelihood fits. To fit the signal in data we use a Crystal Ball function, to fit the background we use a threshold function multiplied with a 4th order polynomial as described above.

4.5.1 Search for Ω_c^*

We analyzed 230.7 fb^{-1} data (Runs 1 to 4). After applying selection cuts, which are outlined in section 3.4, we plot Ω_c^* distributions in Figures 4.14, 4.15, 4.16 and 4.17 for each individual channels. A crystal ball function is used to parameterize the signal and a threshold function multiplied with a 4th order polynomial is used for the background (see section 3.1). The signal shapes are fixed to the values from the signal MC fits, except for the mean value. We observe a signal yield of $39.2^{+9.8}_{-9.1}$ events (stat) at a peak value of $2767.4^{+1.4}_{-1.4}$ MeV with a significance of 4.2 standard deviations in the decay mode C1. The significance is calculated using $\sqrt{2\ln(L_{max}/L_0)}$, where L_{max} and L_0 are the likelihoods for fits with and without a resonance peak component. Then L_0 is reevaluated including systematic uncertainty on the observed signal. In decay mode C2 we get a signal yield of $55.2^{+16.1}_{-15.2}$ events (stat) at a peak value of $2769.3^{+1.3}_{-1.3}$ MeV with a significance of 3.4 standard deviations (σ). In decay mode C4 we get a signal yield of $20.2^{+9.3}_{-8.5}$ events (stat) at a peak value of $2766.9^{+1.9}_{-2.0}$ MeV with a significance of 2.0 standard deviations. We do not see any signal for the C3decay channel. We calculate upper limit on the ratio of production cross section using the Feldman and Cousins method [31] including systematic uncertainty. Assuming the same production mechanism for all the decays of the Ω_c^* we combine all the data from these three decay channels and the fit results a yield of $110.4^{+20.7}_{-20.1}$ events (stat) with a significance of 5.6 σ. After combining all four decay modes of the Ω_c^* the fit results a signal yield of $105.3^{+21.2}_{-20.5}$ events (stat) with a significance of 5.2 σ. Table 4.10 outlines fit results for each channel as well as the combined channels.

Table 4.10: Fit results of $\Delta\Omega_c^*$ distributions are shown for all 4 channels. Lineshapes are fixed to Ω_c^* signal MC except for the mean values.

Decay Channel	$\Delta\Omega_c^*$ (MeV)	σ (MeV)	Ω_c^* events	Significance	χ^2/ndf
C1	$2767.4^{+1.4}_{-1.4}$	4.0 (fixed)	$39.2^{+9.8}_{-9.1}$	4.2	1.00
C2	$2769.3^{+1.3}_{-1.3}$	4.2 (fixed)	$55.2^{+16.1}_{-15.2}$	3.4	0.96
C3	2767.4 (fixed)	4.0 (fixed)	$-5.1^{+5.3}_{-4.7}$	0.9	0.55
C4	$2766.9^{+1.9}_{-2.0}$	4.0 (fixed)	$20.2^{+9.3}_{-8.5}$	2.0	0.66
C1 + C2 + C4	$2768.4^{+0.9}_{-1.0}$	4.0 (fixed)	$110.4^{+20.7}_{-20.1}$	5.6	1.56
c1 + ch2 + ch4	$2768.7^{+1.1}_{-1.3}$	$3.2^{+1.7}_{-1.3}$	$98.9^{+36.2}_{-35.1}$		
combined	$2768.3^{+1.0}_{-1.0}$	4.0 (fixed)	$105.3^{+21.2}_{-20.5}$	5.6	1.53
combined	$2768.8^{+0.7}_{-0.7}$	$2.7^{+1.2}_{-0.9}$	$84.8.9^{+25.9}_{-22.4}$		

4.6 Pizero Study

As a crosscheck We study the π^0 rejection in data to prove that the peak we see for the $\Delta\Omega_c^*$ distribution is not a reflection from $\Omega_c^0\pi^0$ combinations. This study also shows how much the background is reduced. The primary γ from Ω_c^* candidates is combined with an additional reconstructed in the event and the invariant $\gamma\ \gamma$ mass is calculated. We reject all candidates with an invariant mass within $\pm$ 1 σ, $\pm$ 2 σ and $\pm$ 3 σ around the nominal π^0 mass value with all selection criteria and we plot the $\Delta\Omega_c^*$ distributions in Figure 4.20 and Figure 4.21. We fit the $\Delta\Omega_c^*$ using a Crystal Ball and a threshold function multiplied by a 4th order polynomial. The outline of the fits is in Table 4.11. We see a tendency that the central value for the corrected yield is decreasing, but within $\pm$ 1 σ all the results are consistent with each other. This could be the result of the low statistics in the data. The peak we see for $\Delta\Omega_c^*$ is not a reflection from $\Omega_c^0\pi^0$ combinations. We do not use the π^0 rejection for this analysis.

We also have checked the π^0 rejection on $c\bar{c}$ MC. The result is summatrized in Table 4.12. The results are consistent with each other within statistical uncertainties. The fitted distribution is shown in Figure 4.22.

Table 4.11: Fit results of $\Delta\Omega_c^*$ distribution with π^0 mass window rejection.

	Efficiency (%)	Yield (events)	Corrected yield (events)
No π^0 mass rejection	5.72 $\pm$ 0.07	39.2 $\pm$ 9.1	685.3 $\pm$ 159.1
$\pm$ 1 σ π^0 rejection	5.06 $\pm$ 0.07	30.9 $\pm$ 8.5	610.7 $\pm$ 167.9
$\pm$ 2 σ π^0 rejection	4.43 $\pm$ 0.06	26.7 $\pm$ 8.1	602.7 $\pm$ 188.3
$\pm$ 3 σ π^0 rejection	3.77 $\pm$ 0.05	18.6 $\pm$ 6.9	493.4 $\pm$ 183.0

Table 4.12: Fit results for the study of π^0 rejection in $c\bar{c}$ MC.

	Efficiency (%)	Yield (events)	Corrected yield (events)
No π^0 mass rejection	5.72 $\pm$ 0.07	78.3 $\pm$ 14.0	1368.9 $\pm$ 244.8
$\pm$ 1 σ π^0 rejection	5.06 $\pm$ 0.07	60.7 $\pm$ 13.0	1199.6 $\pm$ 256.9
$\pm$ 2 σ π^0 rejection	4.43 $\pm$ 0.06	56.8 $\pm$ 12.2	1282.2 $\pm$ 275.4
$\pm$ 3 σ π^0 rejection	3.77 $\pm$ 0.05	49.7 $\pm$ 10.8	1318.3$\pm$ 286.5

4.7 Omegazero Study

4.7.1 Ω_c^0 MC and data Studies.

After observing Ω_c^* in data we decided to calculate the production cross section ratio of $\frac{\sigma(\Omega_c^*)}{\sigma(\Omega_c^0)}$. In order to calculate it we need Ω_c^0 detection efficiency and the yield from data for each decay mode. We use Ω_c^* signal MC to calculate Ω_c^0 detection efficiencies.

4.7.2 Ω_c^0 MC Studies.

We use Ω_c^0 MC to find Ω_c^0 detection efficiencies. An Ω^- is combined with a pion in order to reconstruct an Ω_c^0 candidate for the decay channel C1. Selections are exactly the same as the Ω_c^* selection, which is given in section 3.3 , except for the X_p cut. We use $X_p(\Omega_c^0) > 0.5$ instead of $X_p(\Omega_c^*) > 0.5$. After applying the selection cuts we plot the $\Delta\Omega_c^0$ invariant mass distribution in Figure 4.23 and 4.24 for each channel using Ω_c^0 signal MC. The distribution is fitted with a double Gaussian (with the same mean) using an unbinned maximum likelihood fit. The fit values are given at table 4.13

Table 4.13: Fit results of $\Delta\Omega_c^0$ mass distribution for all 4 decay channels in Ω_c^0 signal MC. For efficiency calculations we use Ω_c^* signal MC.

Decay channel	Peak value (MeV)	σ_1 (MeV)	σ_2 (MeV)	Efficiency
c1	2698.04 ± 0.04	5.3 ± 0.03	19.29 ± 0.95	16.3 ± 0.8 %
c2	2694.89 ± 3.65	12.43 ± 0.48	37.36± 4.77	5.9 ± 2.1 %
c3	2697.62 ± 0.47	4.13 ± 0.05	17.41 ± 0.64	9.1 ± 0.9 %
c4	2698.53 ± 0.07	4.66 ± 0.08	18.29 ± 0.90	7.2 ± 1.8 %

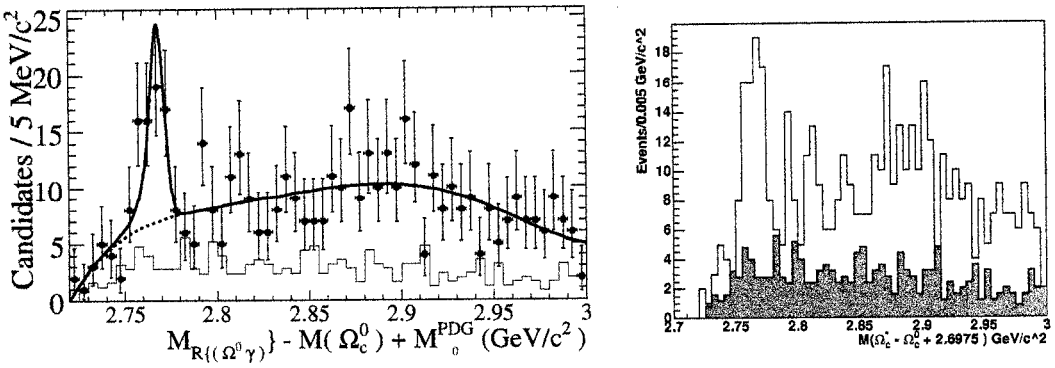

Figure 4.14: $\Delta\Omega_c^*$ distribution in data for C1 is shown. From the fit, the mean value is $2767.4^{+1.4}_{-1.4}$ MeV, σ is fixed to 4.0 MeV, and the yield is $39.2^{+9.8}_{-9.1}$ events. On the right, the empty histogram represents the data (the same as the left plot without error bars) and the hatched histogram is the background selected from the sideband of c1. On the right, the sideband region is $2630MeV < M(c1) < 2660MeV$ and $2728MeV < M(c1) < 2758MeV$.

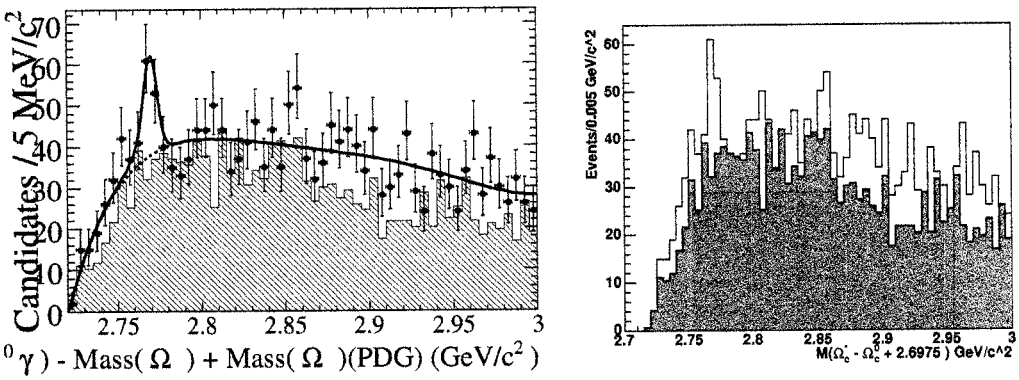

Figure 4.15: $\Delta\Omega_c^*$ distribution in data for C2 is shown. From the fit, the mean value is $2769.3^{+1.3}_{-1.3}$ MeV, σ is fixed to 4.2 MeV, and the yield is $55.2^{+16.1}_{-15.2}$ events. On the right the empty histogram represents the data (the same as the left plot without error bars) and the hatched histogram is the background selected from the sideband of c2. The sideband region is $2590MeV < M(c2) < 2635MeV and 2728MeV < M(c2) < 2768MeV$.

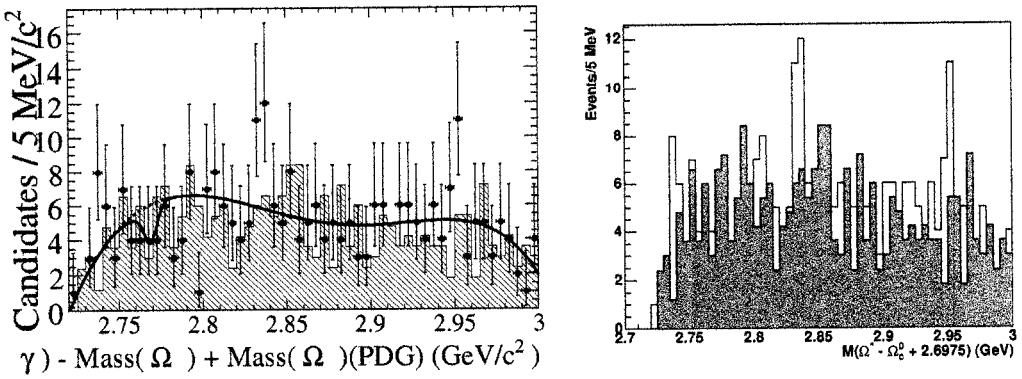

Figure 4.16: $\Delta\Omega_c^*$ distribution in data for C3 is shown. From the fit, the yield is $-5.1^{+5.3}_{-4.7}$ events, where the mean value is fixed to 2767.4 MeV and σ is fixed to 4.0 MeV. On the right the empty histogram represents the data (the same as the left plot without error bars) and the hatched histogram is the background selected from the sideband of c3. The sideband region is $2635MeV < M(c3) < 2665MeV and 2725MeV < M(c3) < 2755MeV$.

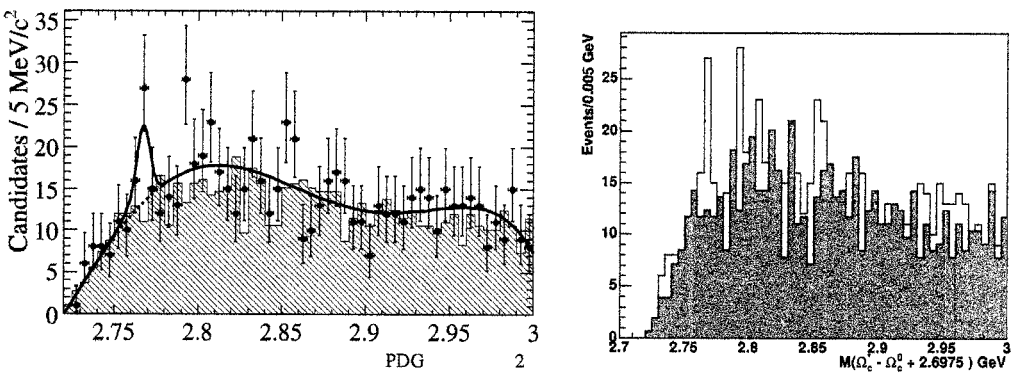

Figure 4.17: $\Delta\Omega_c^*$ distribution in data for C4. From the fit,mean value is $2766.9^{+1.9}_{-2.0}$ MeV, σ is fixed to 4.0 MeV, and the yield is $20.2^{+9.3}_{-8.5}$ events. On the right, the empty histogram represents the data (the same as the left plot without error bars) and the hatched histogram is the background selected from the sideband of c4. The sideband region is $2640MeV < M(c4) < 2664MeV and 2727MeV < M(c4) < 2745MeV$.

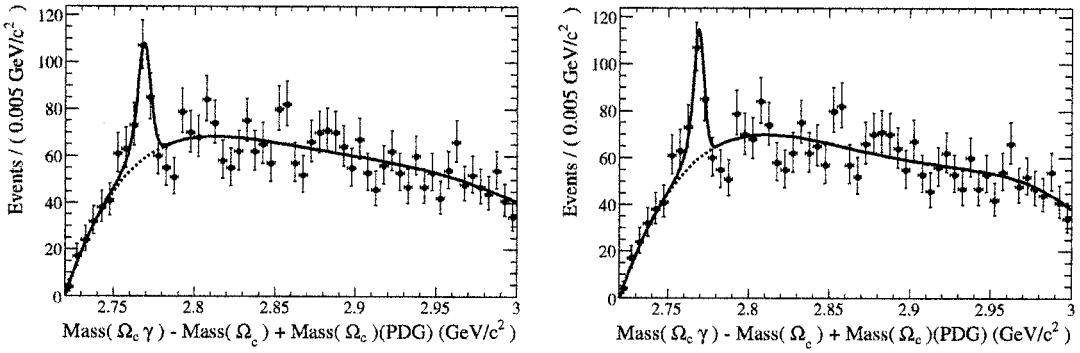

Figure 4.18: $\Delta\Omega_c^*$ distribution in data with all the channels combined except for C3 is shown on the left (σ is fixed). From the fit, the mean value is $2768.4^{+0.9}_{-1.0}$ MeV, σ is fixed to 4.0 MeV and the yield is $110.4^{+20.7}_{-20.1}$ events. On the right, the same distribution with released σ is shown. From the fit, the mean value is $2768.7^{+1.1}_{-1.3}$ MeV, σ is $3.2^{+1.7}_{-1.3}$ MeV, and the yield is $98.9^{+36.2}_{-35.1}$ events.

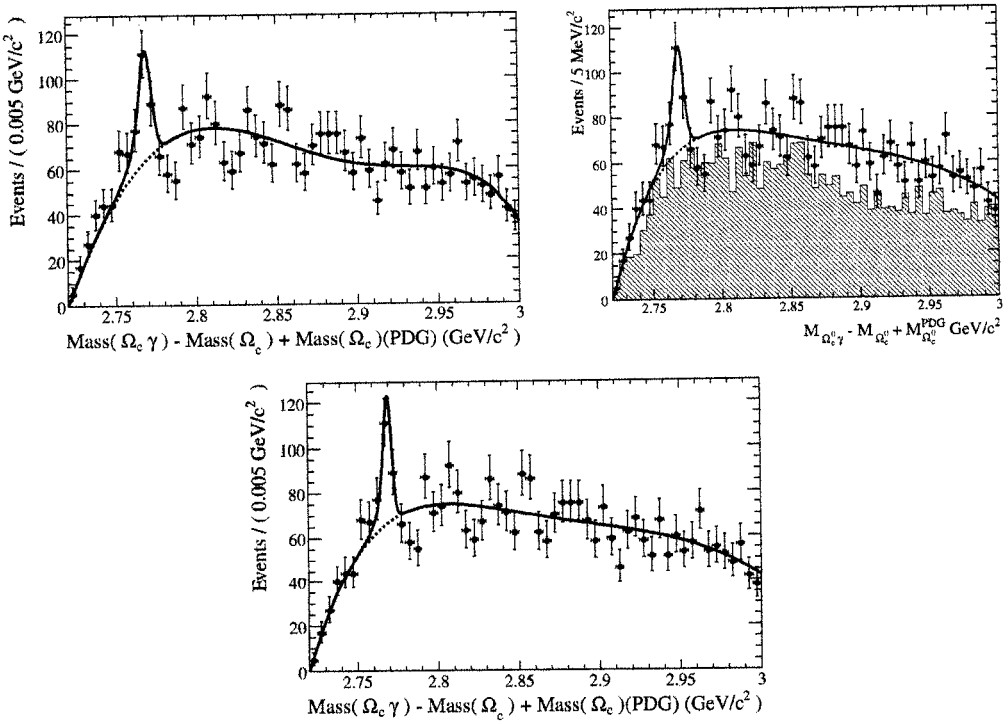

Figure 4.19: $\Delta\Omega_c^*$ distribution in data for all 4 channels combined is shown. On the left, from the fit, the mean value is $2768.3^{+1.0}_{-1.0}$ MeV, σ is fixed to 4.0 MeV and the yield is $105.3^{+21.2}_{-20.5}$ events. On the right, the mean value is $2768.8^{+0.7}_{-0.7}$ MeV, σ is $2.7^{+1.2}_{-0.9}$ MeV, and the yield is $84.8.9^{+25.9}_{-22.4}$ events.

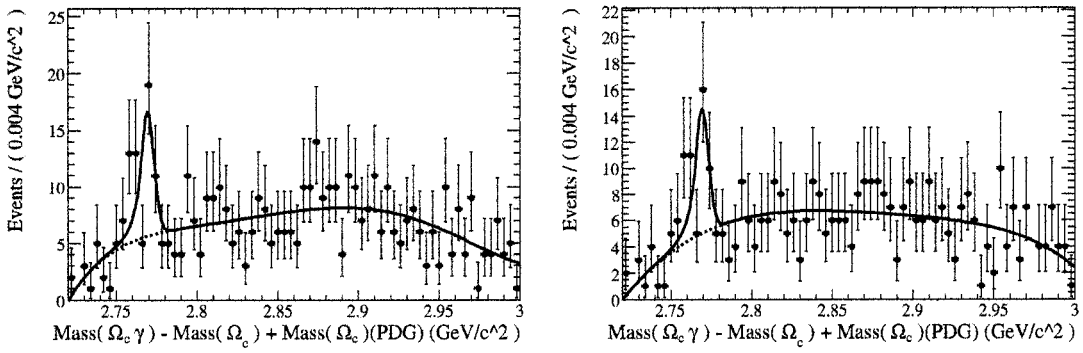

Figure 4.20: $\Delta\Omega_c^*$ distribution in data is shown for the decay channel C1 is shown with $\pm$ 1 σ π^0 rejection on the left, and with $\pm$ 2 σ π^0 rejection on the right. On the left, the mean value is 2769.0 $\pm$ 1.5 MeV, σ is fixed to 4 MeV, and the yield is 30.9 $\pm$ 8.5 events. On the right, the mean value is 2769.1 $\pm$ 1.6 MeV, σ_1 is fixed to 4 MeV, and the yield is 26.7 $\pm$ 8.1 events.

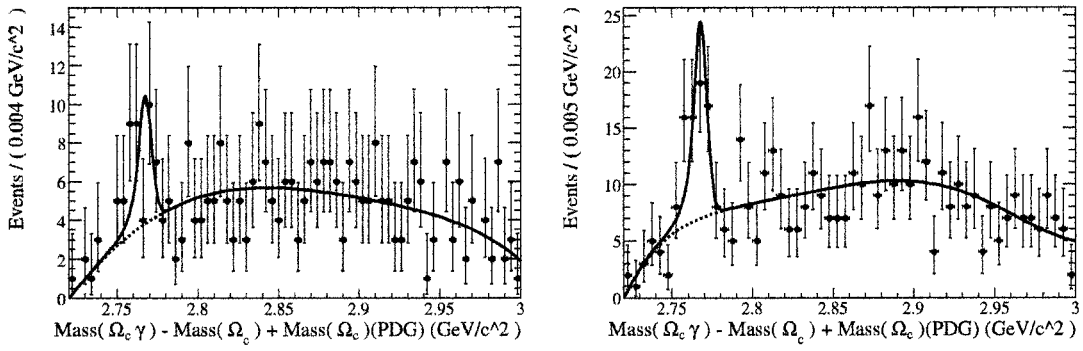

Figure 4.21: $\Delta\Omega_c^*$ distribution in data is shown for the decay channel C1 is shown with $\pm$ 3 σ π^0 rejection on the left, and without π^0 mass window rejection on the right. On the left, the mean value is 2766.9 $\pm$ 2.6 MeV, σ is fixed to 4 MeV, and the yield is 18.6 $\pm$ 6.9 events. On the right, the mean value is 2767.4 $\pm$ 1.3 MeV, σ_1 is fixed to 4 MeV, and the yield is 39.2 $\pm$ 9.1 events.

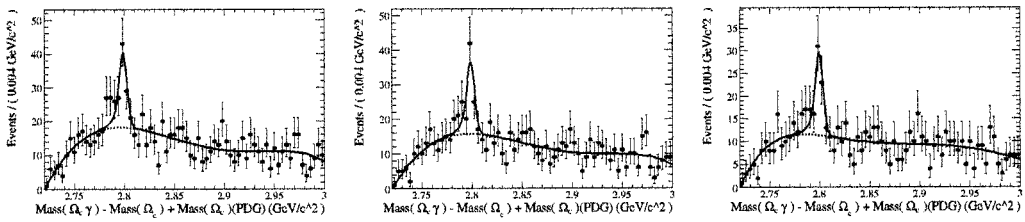

Figure 4.22: $\Delta\Omega_c^*$ distribution in $c\bar{c}$ MC is shown for the decay channel C1 is shown with $\pm$ 1 σ π^0 rejection on the left, and with $\pm$ 2 σ π^0 rejection in the middle and with $\pm$ 3 σ π^0 rejection on the right . The signal shape is fixed to the value from the signal MC.

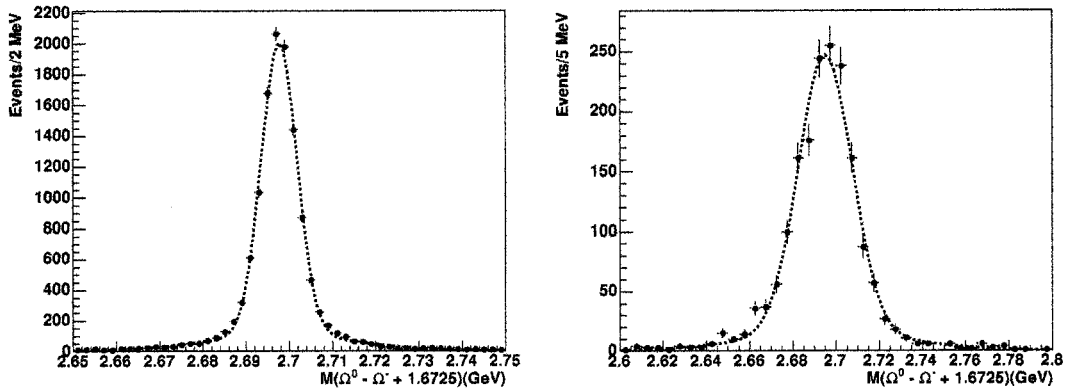

Figure 4.23: $\Delta\Omega_c^0$ mass distribution in signal MC is shown for the decay channelc1 is shown on the left, and for the decay channel c2 is shown on the right. On the left, the mean value is 2698.04 $\pm$ 0.04 MeV, σ_1 is 5.29 $\pm$ 0.03 MeV, σ_2 is 19.29 $\pm$ 0.95 MeV and the fraction of σ_1 is 91.82 %. On the right, the mean value is 2694.89 $\pm$ 3.65 MeV, σ_1 is 12.43 $\pm$ 0.48 MeV, σ_2 is 37.36 $\pm$ 4.77 MeV and the fraction of σ_1 is 83.41 %.

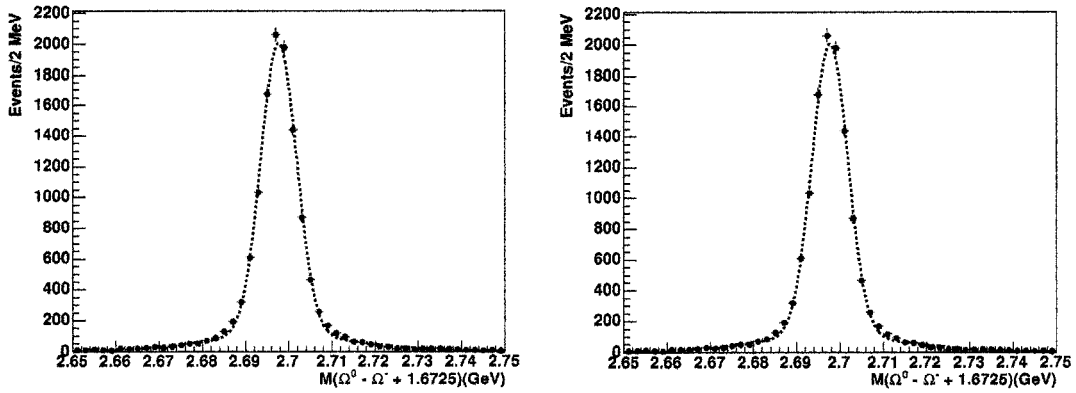

Figure 4.24: $\Delta\Omega_c^0$ distribution in signal MC is shown for the decay channel c3 is shown on the left, and for the decay channel c4 is shown on the right. On the left, the mean value is 2697.62 $\pm$ 0.47 MeV, σ_1 is 4.13 $\pm$ 0.05 MeV, σ_2 is 17.41 $\pm$ 0.64 MeV and the fraction of σ_1 is 90.63 %. On the right, the mean value is 2698.53 $\pm$ 0.07 MeV, σ_1 is 4.66 $\pm$ 0.08 MeV, σ_2 is 18.29 $\pm$ 0.90 MeV and the fraction of σ_1 is 83.81 %.

4.7.3 Ω_c^0 data Studies.

We analyze 230.7 fb^{-1} data to reconstruct $\Omega_c^0 s$. Selections are exactly the same as Ω_c^* selection, which is given at section 3.3 , except the X_p cut. We use X_p of Ω_c^0 instead of X_p Ω_c^*. After applying selection criteria we plot $\Delta\Omega_c^0$ mass distribution at Figure 4.25 and 4.26. Lineshapes are fixed to Ω_c^0 signal MC. The distribution is fitted with double Gaussian (the same mean) using unbinned fit. Fitting parameters are given at Table 4.14.

Table 4.14: Fit results of $\Delta\Omega_c^0$ mass distribution for all 4 decay channels are shown in data. Lineshapes are fixed to Ω_c^0 signal MC.

Decay	Peak value (MeV)	σ_1 (MeV)	σ_2 (MeV)	σ_1 Frac.(%)	Yield	χ^2/ndf
c1	$2693.3^{+0.6}_{-0.6}$	5.3	19.3	91.8	$156.4^{+15.4}_{-14.7}$	3.40
c2	2693.3 MeV (fixed)	12.4	37.4	83.4	$91.6^{+26.0}_{-25.4}$	1.53
c3	2693.3 (fixed)	4.1	17.4	90.6	$23.3^{+9.9}_{-9.1}$	0.59
c4	2693.3 (fixed)	4.7	18.3	83.8	$34.0^{+14.9}_{-14.1}$	0.71

4.8 Systematic Errror Studies

We are measuring the ratio of production cross sections of $\frac{\sigma(\Omega_c^*)}{\sigma(\Omega_c^0)}$, therefore many of the systematic uncertainties get canceled.

4.8.1 Canceled Systematics

The following systematic uncertainties are negligible:

- Track finding: We use the Ω_c^0 decay mode as normalization mode. The effect

due to the tracking is negligible.

- PID : We use the same PID requirements for Ω_c^* and Ω_c^0 reconstruction therefore the uncertainty due to the PID is negligible.

- Uncertainty on luminosity measurement: It is about 1 % , but cancels out.

- Uncertainty on daughter branching fraction [33]: also negligible.

4.8.2 Calculated Systematics

The following systematic uncertainties are calculated:

- MC statistics. Because we have limited signal MC. The systematic uncertainties are 1.4 %, 3.2 %, 1.4 %, and 3.2 % for R1=$\frac{\sigma(e^+e^-\rightarrow C1)}{\sigma(e^+e^-\rightarrow c1)}$, R2=$\frac{\sigma(e^+e^-\rightarrow C2)}{\sigma(e^+e^-\rightarrow c2)}$, R3=$\frac{\sigma(e^+e^-\rightarrow C3)}{\sigma(e^+e^-\rightarrow c3)}$, and

  R4=$\frac{\sigma(e^+e^-\rightarrow C4)}{\sigma(e^+e^-\rightarrow c4}$ respectively.

- Photon Selection: No correction is applied for photons because we use a neutral smearing procedure [32]. Systematic uncertainty due to the photon is about 1.8 %.

- Fitting : Systematic uncertainties due to the fitting are calculated by changing the signal and the background shapes. For the Ω_c^0 we vary σ of the signal shape by $\pm$ 1 σ, any change in signal yield is assigned as systematic uncertainty. For the background shape, we vary the order of the polynomial, and any change in signal yield is assigned as systematic uncertainty. The systematic uncertainties are 3.4 %, 5.7 %, 5.6 %, and 5.9 % due to Ω_c^0 fitting. As for the Ω_c^* fitting, fixed parameters, which are n, α and σ, are varied by $\pm$ 1 σ.

For the background shape, we change the polynomial function to 3rd and 5th order. The systematic uncertainties are 15.5 %, 10.2 %, 19.1 %, and 15.4 % due to Ω_c^* fitting.

- For the mass measurement, we quote mass difference Δ M(mass of Ω_c^* - mass of Ω_c^0). We applied energy correction as described [34] and found the shift in ΔM to be 1.1 MeV which is recommended by neutral group at *BABAR*.

We added the individual contributions to the systematic uncertainty in quadrature. The Outline of systematic errors are given in in Table 4.15.

Table 4.15: Outline of systematic errors

Sources of Systematic Errors.	Systematic Error
Track finding	Cancel out
PID	Cancel out
Uncertainty in luminosity	Cancel out
Uncertainty in daughter fraction	Cancel out

Sources of Systematic Errors.	R1	R2	R3	R4
MC statistics	1.4 %	3.2 %	1.4 %	3.2 %
Photon Selection	1.8 %	1.8 %	1.8 %	1.8 %
Ω_c^* Fitting	15.5 %	10.2 %	19.1 %	15.4 %
Ω_c^0 Fitting	3.4 %	5.7 %	5.6 %	5.9 %
Total Systematic Errors	16.0 %	12.2 %	20.0 %	16.9 %

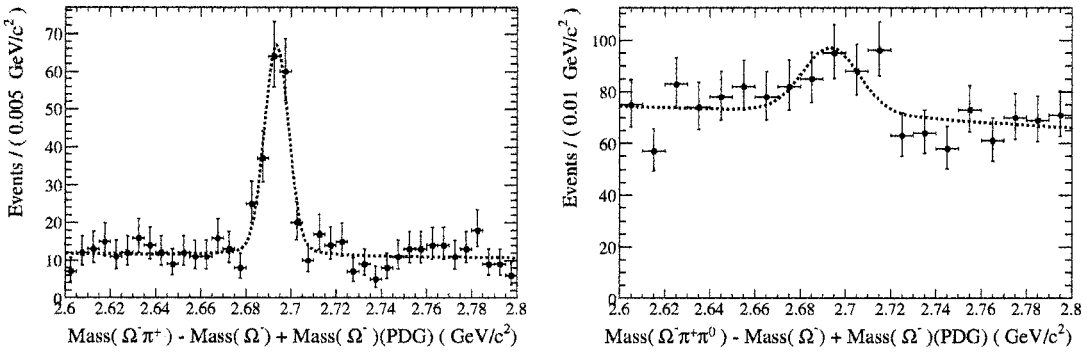

Figure 4.25: On the left, $\Delta\Omega_c^0$ distribution in data is shown. From the fit, the mean value is $2693.3^{+0.6}_{-0.6}$ MeV, σ_1 is 5.3 MeV, σ_2 is 19.3 MeV, fraction of the σ_1 is 91.8 % and the yield is $156.4^{+15.4}_{-14.7}$ events. On the right, the same distribution is shown for C2. The mean value is fixed to 2693.3 MeV, σ_1 is 12.4 MeV , σ_2 is 37.4MeV, fraction of σ_1 is 83.4 % and the yield is $91.6^{+26.0}_{-25.4}$ events.

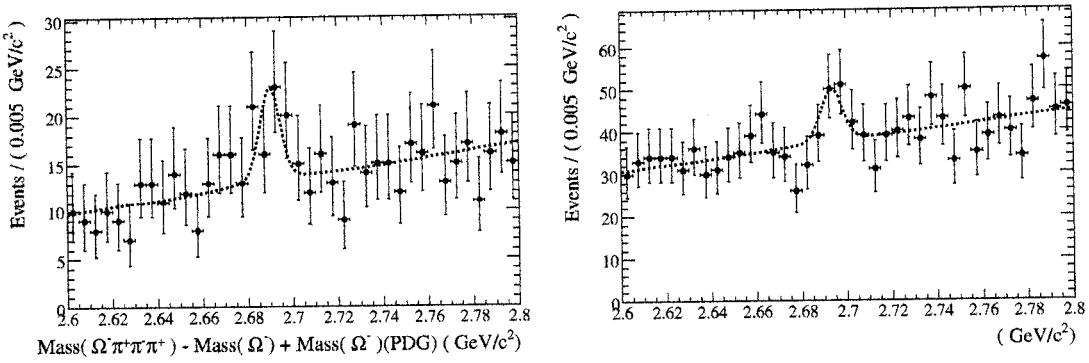

Figure 4.26: On the left, $\Delta\Omega_c^0$ distribution in data is shown for c3. From the fit, the mean value is 2693.3 MeV (fixed), σ_1 is 4.1 MeV , σ_2 is 17.4 MeV, fraction of σ_1 is 90.6 % and the yield is $23.3^{+9.9}_{-9.1}$ events and for the decay channel c4 is shown on the right. On the right, the same distribution is shown for C4. The mean value is fixed to 2693.3 MeV, σ_1 is 4.7 MeV, σ_2 is 18.3 MeV, fraction of σ_1 is 83.8 % and the yield is $34.0^{+14.9}_{-14.1}$ events.

Chapter 5

Results

5.1 Summary

We observe significant Ω_c^* signals in the decay modes C1, and C2, and some in C4. We do not observe any signal in the decay channel C3. We calculate the ratio of production cross sections of $\frac{\sigma(\Omega_c^*)}{\sigma(\Omega_c^0)}$. In order to calculate it we need the Ω_c^0 detection efficiency and th e yield from the data for each decay modes of Ω_c^0. This study is shown in detail in appendix C. Table 5.1 shows the yield of Ω_c^0 as we ll as the yield of Ω_c^* from the data including the respective efficiencies. Ω_c^0 yields are obtained by fixing the lineshape to Ω_c^0 signal MC. F or Ω_c^* decay modes we use $X_p(\Omega_c^*) > 0.5$ and for Ω_c^0 decay modes we use $X_p(\Omega_c^0) > 0.5$. In Table 5.2 we give the ratios of the production cross section of Ω_c^* and Ω_c^0 for each channel. Results are consistent with each other within statistical and systematic uncerta inties.

Table 5.1: Ω_c^* yields, Ω_c^0 yields and ratio of the detection effici encies for all 4 decay channels in data.

Ch	Ω_c^* Efficiency/ Ω_c^0 Efficiency	Ω_c^* Yield (events)	Ω_c^0 Yield (events)
C1	0.35 ± 0.005	$39.2^{+9.8}_{-9.1}$	$156.4^{+15.4}_{-14.7}$
C2	0.34 ± 0.011	$55.2^{+16.1}_{-15.2}$	$91.6^{+26.0}_{-25.4}$
C3	0.33 ± 0.005	$-5.1^{+5.3}_{-4.7}$	$23.3^{+9.9}_{-9.1}$
C4	0.35 ± 0.011	$20.2^{+9.3}_{-8.5}$	$34.0^{+14.9}_{-14.1}$

Table 5.2: Ratio of Production cross sections for different decay modes is given below. For Ω_c^* decay modes we use $X_p(\Omega_c^*) > 0.5$ and for Ω_c^0 decay modes we use $X_p(\Omega_c^0) > 0.5$. The first uncertainty is statistical error and the second one is systematic er ror.

Ratio of Production Cross Sections	Results
$\frac{\sigma(e^+e^- \to C1)}{\sigma(e^+e^- \to c1)}$	$0.71^{+0.19}_{-0.18} \pm 0.11$
$\frac{\sigma(e^+e^- \to C2)}{\sigma(e^+e^- \to c2)}$	$1.76^{+0.71}_{-0.69} \pm 0.19$
$\frac{\sigma(e^+e^- \to C3)}{\sigma(e^+e^- \to c3)}$	$< 0.68@90\% C.L.$
$\frac{\sigma(e^+e^- \to C4)}{\sigma(e^+e^- \to c4}$	$1.70^{+1.0}_{-0.9} \pm 0.27$
$\frac{\sigma(e^+e^- \to (\Omega_c^* \ (ch1+ch2+ch3+ch4)))}{\sigma(e^+e^- \to (\Omega_c^0 \ (ch1+ch2+ch3+ch4)))}$	$1.0^{+0.23}_{-0.22} \pm 0.11$

5.2 Conclusions

We report the first observation of Ω_c^* decaying to Ω_c^0 and γ. For the decay channel C1, we observe a signal yield of $39.2^{+9.8}_{-9.1}$ (stat) with a significance of 4.2 standard deviations. We observe signals in C2 and C4 with significances of 3.4 and 2.0 σ, respectively. Assuming the sam e production mechanism for all decay channels of Ω_c^* we combine all the data from these three decay modes and the fit results in a yield of $110.4^{+20.7}_{-20.1}$ events (stat) with 5.6 σ significance. We do not see

any signal from the C3 decay channel. After combining all four decay modes of t he Ω_c^* the fit results a signal yield of $105.3^{+21.2}_{-20.5}$ events (stat) with 5.2 σ significance. We also report the mass difference M(ø mgcst -Ω_c^0) of newly discovered singly charmed baryon Ω_c^* to be $70.8^{+1.0}_{-1.0}$ (stat) $\pm$ 1.1 (syst) MeV.

Appendices

Appendix A

Optimization Tables

In this part of the appendix we present optimization study in tables.

A.1 Optimization Tables of the C1.

	Proton	Pion	$\frac{S}{\sqrt{B}}$
1	PLhVeryLoose	PiLhVeryLoose	141,523
2	PLhVeryLoose	PiLhLoose	143,303
3	PLhVeryLoose	PiLhTight	143,568
4	PLhVeryLoose	PiLhVeryTight	143,469
5	PLhLoose	PiLhVeryLoose	155,737
6	PLhLoose	PiLhLoose	156,678
7	PLhLoose	PiLhTight	156,925
8	PLhLoose	PiLhVeryTight	156,792
9	PLhTight	PiLhVeryLoose	161,314
10	PLhTight	PiLhLoose	162,024
11	PLhTight	PiLhTight	162,125
12	PLhTight	PiLhVeryTight	161,906
13	PLhVeryTight	PiLhVeryLoose	156,852
14	PLhVeryTight	PiLhLoose	157,357
15	PLhVeryTight	PiLhTight	157,369
16	PLhVeryTight	PiLhVeryTight	157,023

Table A.1: Λ^0 3D flight cut optimization is shown for the decay channel C1.

	Λ^0 3D Flight Cut (cm)	$\frac{S}{\sqrt{B}}$
1	> 0.10	169,052
2	> 0.15	170,711
3	> 0.20	171,012
4	> 0.25	171,026
5	> 0.30	171,096
6	> 0.35	170,938
7	> 0.40	170,458

Table A.2: Optimization of Λ^0 χ^2 decay vertex is shown for decay channel C1

	$\chi^2_{\Lambda^0 Vertex}$ cut	$\frac{S}{\sqrt{B}}$
1	< 6	183,196
2	< 10	185,149
3	< 20	185,402
4	< 30	184,859
5	< 40	184,470
6	< 50	183,779
7	< 100	181,877

Table A.3: Λ^0 mass cut optimization is shown for decay channel C1

	Width (MeV) of Λ^0	$\frac{S}{\sqrt{B}}$
1	$\pm$ 1.90	194,731
2	$\pm$ 3.80	206,196
3	$\pm$ 4.75	204,481
4	$\pm$ 5.70	201,986
5	$\pm$ 6.65	199,649
6	$\pm$ 7.60	196,944

Table A.4: Ω^- PID optimization is shown for C1

	Kaon	$\frac{S}{\sqrt{B}}$
1	KLhVeryLoose	232,518
2	KLhLoose	270,842
3	KLhTight	306,564
4	KLhVeryTight	306,866

Table A.5: 3D flight cut of Ω^- is shown for the decay channel C1.

	3D Flight Cut of Ω^- (cm)	$\frac{S}{\sqrt{B}}$
1	> 0.10	363,264
2	> 0.15	383,857
3	> 0.20	394,996
4	> 0.25	396,753
5	> 0.30	396,470
6	> 0.35	393,439
7	> 0.40	387,616

Table A.6: χ^2 decay vertex cut of Ω^- is shown for the decay channel C1.

	$\chi^2_{\Omega^- Vertex}$ of Ω^-	$\frac{S}{\sqrt{B}}$
1	< 10	446,242
2	< 15	452,608
3	< 20	454,682
4	< 25	455,824
5	< 30	457,078
6	< 35	456,794
7	< 40	456,159

Table A.7: Mass cut of Ω^- is shown for the decay channel (C1 .

	Width (MeV) of Ω^-	$\frac{S}{\sqrt{B}}$
1	$\pm$ 2.6	1,244,561
2	$\pm$ 5.2	1,330,598
3	$\pm$ 6.5	1,256,072
4	$\pm$ 7.8	1,136,432
5	$\pm$ 9.1	1,049,080
6	$\pm$ 10.4	980,146

Table A.8: PID selections of Ω_c^0 is shown for the decay channel (C1 .

	Pion	$\frac{S}{\sqrt{B}}$
1	PiLhVeryLoose	1,330,598
2	PiLhLoose	1,352,922
3	PiLhTight	1,349,049
4	PiLhVeryTight	1,274,641

Table A.9: χ^2 vertex cut of Ω_c^0 is shown for the decay channel (C1 .

	$\chi^2_{\Omega_c^0 Vertex}$ of Ω_c^0	$\frac{S}{\sqrt{B}}$
1	< 7	1,936,500
2	< 8	1,942,078
3	< 9	1,949,064
4	< 10	1,955,340
5	< 11	1,957,558
6	< 12	1,944,482
7	< 13	1,945,841
8	< 20	1,910,550
9	< 30	1,880,549

Table A.10: Mass cut of Ω_c^0 is shown for the decay channel (C1 .

	Width (MeV) of Ω_c^0	$\frac{S}{\sqrt{B}}$
1	$\pm$ 6.0	2,312,307
2	$\pm$ 12.0	3,018,188
3	$\pm$ 15.0	3,034,420
4	$\pm$ 18.0	3,030,678
5	$\pm$ 21.0	2,989,282
6	$\pm$ 24.0	2,972,327

Table A.11: s9/s25 cuts of γ candidates is shown for the decay channel C1.

	γ s9/s25 cut	$\frac{S}{\sqrt{B}}$
1	s9/s25 $>$ 0.8	3,095,429
2	s9/s25 $>$ 0.85	3,094,984
3	s9/s25 $>$ 0.9	3,113,535
4	s9/s25 $>$ 0.91	3,072,284
5	s9/s25 $>$ 0.92	3,050,730
6	s9/s25 $>$ 0.93	3,009,642

Table A.12: Latency cuts of γ candidates is shown for the decay channel (C1 .

	γ LAT Cut	$\frac{S}{\sqrt{B}}$
1	LAT$>$ 0.01,LAT $<$ 0.9	3,649,059
2	LAT$>$ 0.01,LAT $<$ 0.8	3,649,059
3	LAT$>$ 0.01,LAT $<$ 0.75	3,654,343
4	LAT$>$ 0.01,LAT $<$ 0.7	3,649,714
5	LAT$>$ 0.01,LAT $<$ 0.6	3,625,759
6	LAT$>$ 0.01 ,LAT $<$ 0.5	3,597,429

Table A.13: γ Energy Cuts is shown for the decay channel C1 .

	γ Energy Cut	$\frac{S}{\sqrt{B}}$
1	$>$ 40	3,781,423
2	$>$ 45	3,846,549
3	$>$ 50	3,998,383
4	$>$ 55	4,175,545
5	$>$ 60	4,257,623
6	$>$ 65	4,383,030
7	$>$ 70	4,587,623
8	$>$ 75	4,630,912
9	$>$ 80	4,676,121
10	$>$ 85	4,648,011
11	$>$ 90	4,570,192

A.2 Optimization of C2.

Table A.14: PID selections of pion for Ω_c^0 optimizing is shown for C2.

	Pion	$\frac{S^2}{B}$
1	PiLhVeryLoose	119,542
2	PiLhLoose	125,963
3	PiLhTight	125,542
4	PiLhVeryTight	1,222,285

Table A.15: Latency cuts of 2 γ candidates that reconstruct π^0 is shown for C2.

	γ LAT Cuts	$\frac{S}{\sqrt{B}}$
1	LAT$>$ 0.01,LAT $<$ 0.80	148,875
2	LAT$>$ 0.01,LAT $<$ 0.75	151,519
3	LAT$>$ 0.01,LAT $<$ 0.70	153,674
4	LAT$>$ 0.01,LAT $<$ 0.65	155,468
5	LAT$>$ 0.01,LAT $<$ 0.60	158,681
6	LAT$>$ 0.01,LAT $<$ 0.55	162,920
7	LAT$>$ 0.01,LAT $<$ 0.50	163,337
8	LAT$>$ 0.01,LAT $<$ 0.45	162,702
9	LAT$>$ 0.01,LAT $<$ 0.40	155,741

Table A.16: s9/s25 cuts of γ candidates is shown for C2.

	γ of π^0 s9/s29 cut	$\frac{S}{\sqrt{B}}$
1	s9/s25 $>$ 0.70	167,080
2	s9/s25 $>$ 0.75	170,053
3	s9/s25 $>$ 0.80	173,374
4	s9/s25 $>$ 0.85	177,008
5	s9/s25 $>$ 0.90	178,076
6	s9/s25 $>$ 0.91	177,655
7	s9/s25 $>$ 0.92	177,140
8	s9/s25 $>$ 0.93	174,591
9	s9/s25 $>$ 0.94	172,283
10	s9/s25 $>$ 0.95	166,621

Table A.17: Energy cut of γ candidates is shown for C1.

	γ of π^0 E cut	$\frac{S}{\sqrt{B}}$
1	Egam$>$ 40	189,723
2	Egam$>$ 45	195,587
3	Egam$>$ 50	199,742
4	Egam$>$ 55	203,662
5	Egam$>$ 60	205,405
6	Egam$>$ 65	216,608
7	Egam$>$ 70	220,257
8	Egam$>$ 75	222,367
9	Egam$>$ 80	229,298
10	Egam$>$ 85	237,049
11	Egam$>$ 90	239,871

Table A.18: Mass cut of π^0 is shown for C1.

	Width (MeV) of π^0	$\frac{S}{\sqrt{B}}$
1	$\pm$ 5.0	318,195
2	$\pm$ 10.0	370,824
3	$\pm$ 12.5	335,630
4	$\pm$ 15.0	308,468
5	$\pm$ 17.5	296,072
6	$\pm$ 20.0	278,629

Table A.19: Mass cut of Ω_c^0 is shown for C1

	Width (σ) of Ω_c^0	$\frac{S}{\sqrt{B}}$
1	$\pm$ 13.2	1,254,925
2	$\pm$ 26.4	1,308,629
3	$\pm$ 33.0	1,077,819
4	$\pm$ 39.6	936,236
5	$\pm$ 46.2	811,478
6	$\pm$ 52.8	794,256

A.3 Optimization of C3

Table A.20: PID of Ω_c^0 is shown for C3.

	Pion	Pion	Pion	$\frac{S}{\sqrt{B}}$
1	PiLhVeryLoose	PiLhVeryLoose	PiLHVeryLoose	265,904
2	PiLhVeryLoose	PiLhVeryLoose	PiLLoose	268,393
3	PiLhVeryLoose	PiLhVeryLoose	PiLTight	266,632
4	PiLhVeryLoose	PiLhVeryLoose	PiLHVeryTight	263,859
5	PiLhVeryLoose	PiLhLoose	PiLHVeryLoose	269,204
6	PiLhVeryLoose	PiLhLoose	PiLLoose	271,645
7	PiLhVeryLoose	PiLhLoose	PiLTight	269,919
8	PiLhVeryLoose	PiLhLoose	PiLHVeryTight	267,196
9	PiLhVeryLoose	PiLhTight	PiLHVeryLoose	267,152
10	PiLhVeryLoose	PiLhTight	PiLHLoose	269,600
11	PiLhVeryLoose	PiLhTight	PiLHTight	267,925
12	PiLhVeryLoose	PiLhTight	PiLHVeryTight	265,229
13	PiLhVeryLoose	PiLhVeryTight	PiLHVeryLoose	261,461
14	PiLhVeryLoose	PiLhVeryTight	PiLLoose	263,601
15	PiLhVeryLoose	PiLhVeryTight	PiLTight	262,047
16	PiLhVeryLoose	PiLhVeryTight	PiLHVeryTight	259,444
17	PiLhLoose	PiLhVeryLoose	PiLHVeryLoose	273,621
18	PiLhLoose	PiLhVeryLoose	PiLLoose	276,363
19	PiLhLoose	PiLhVeryLoose	PiLTight	274,678
20	PiLhLoose	PiLhVeryLoose	PiLHVeryTight	271,987
21	PiLhLoose	PiLhLoose	PiLHVeryLoose	276,236
22	PiLhLoose	PiLhLoose	PiLHLoose	278,908
23	PiLhLoose	PiLhLoose	PiLHTight	277,260
24	PiLhLoose	PiLhLoose	PiLHVeryTight	274,619
25	PiLhLoose	PiLhTight	PiLHVeryLoose	274,254
26	PiLhLoose	PiLhTight	PiLLoose	276,936
27	PiLhLoose	PiLhTight	PiLTight	275,341
28	PiLhLoose	PiLhTight	PiLHVeryTight	272,730
29	PiLhLoose	PiLhVeryTight	PiLHVeryLoose	268,373
30	PiLhLoose	PiLhVeryTight	PiLLoose	270,726
31	PiLhLoose	PiLhVeryTight	PiLTight	269,254
32	PiLhLoose	PiLhVeryTight	PiLHVeryTight	266,737

Table A.21: PID of Ω_c^0 is shown for C3.

	Pion	Pion	Pion	$\frac{S}{\sqrt{B}}$
33	PiLhTight	PiLhVeryLoose	PiLHVeryLoose	273,423
34	PiLhtight	PiLhVeryLoose	PiLLoose	276,235
35	PiLhTight	PiLhVeryLoose	PiLTight	274,280
36	PiLhTight	PiLhVeryLoose	PiLHVeryTight	271,735
37	PiLhTight	PiLhLoose	PiLHVeryLoose	276,107
38	PiLhTight	PiLhLoose	PiLLoose	278,850
39	PiLhTight	PiLhLoose	PiLTight	276,926
40	PiLhTight	PiLhLoose	PiLHVeryTight	274,435
41	PiLhTight	PiLhTight	PiLHVeryLoose	274,159
42	PiLhTight	PiLhTight	PiLHLoose	276,913
43	PiLhTight	PiLhTight	PiLHTight	275,042
44	PiLhTight	PiLhTight	PiLHVeryTight	272,581
45	PiLhTight	PiLhVeryTight	PiLHVeryLoose	268,221
46	PiLhtight	PiLhVeryTight	PiLLoose	270,638
47	PiLhTight	PiLhVeryTight	PiLTight	268,894
48	PiLhTight	PiLhVeryTight	PiLHVeryTight	266527
49	PiLhVeryTight	PiLhVeryLoose	PiLHVeryLoose	275746
50	PiLhVeryTight	PiLhVeryLoose	PiLLoose	277643
51	PiLhVeryTight	PiLhVeryLoose	PiLTight	276281
52	PiLhVeryTight	PiLhVeryLoose	PiLHVeryTight	274120
53	PiLhVeryTight	PiLhLoose	PiLHVeryLoose	278483
54	PiLhVeryTight	PiLhLoose	PiLHLoose	280766
55	PiLhVeryTight	PiLhLoose	PiLHTight	278964
56	PiLhVeryTight	PiLhLoose	PiLHVeryTight	276867
57	PiLhVeryTight	PiLhTight	PiLHVeryLoose	280224
58	PiLhVeryTight	PiLhTight	PiLLoose	278967
59	PiLhVeryTight	PiLhTight	PiLTight	277220
60	PiLhVeryTight	PiLhTight	PiLHVeryTight	275157
61	PiLhVeryTight	PiLhVeryTight	PiLHVeryLoose	269853
62	PiLhVeryTight	PiLhVeryTight	PiLLoose	271780
63	PiLhVeryTight	PiLhVeryTight	PiLTight	270160
64	PiLhVeryTight	PiLhVeryTight	PiLHVeryTight	268182

Table A.22: χ^2 vertex cut of Ω_c^0 is shown for C3.

	$\chi^2_{\Omega_c^0 Vertex}$ of Ω_c^0	$\frac{S}{\sqrt{B}}$
1	< 5	936500
2	< 10	942078
3	< 13	949064
4	< 14	955340
5	< 15	957558
6	< 16	944482
7	< 17	945841
8	< 20	910550

Table A.23: Mass cut of Ω_c^0 is shown for C3

	Width (σ) of Ω_c^0	$\frac{S}{\sqrt{B}}$
1	$\pm$ 1.0 σ	1342065
2	$\pm$ 2.0 σ	1389714
3	$\pm$ 2.5 σ	1327765
4	$\pm$ 3.0 σ	1258775
5	$\pm$ 3.5 σ	1106976
6	$\pm$ 4.0 σ	1015529

A.4 Optimization of C4.

Table A.24: PID selections of Ξ^- is shown for C4.

	Pion	$\frac{S}{\sqrt{B}}$
1	PiLhVeryLoose	636
2	PiLhLoose	643
3	PiLhTight	648
4	PiLhVeryTight	651

Table A.25: 3D flight cut of Ξ^- is shown for C4.

	3D Flight Cut of Ξ^- (cm)	$\frac{S}{\sqrt{B}}$
1	> 0.10	693
2	> 0.15	703
3	> 0.20	706
4	> 0.25	707
5	> 0.30	704
6	> 0.35	700
7	> 0.40	696

Table A.26: ${\chi^2}_{\Xi^- Vertex}$ cut is shown for C4.

	${\chi^2}_{\Xi^- Vertex}$	$\frac{S}{\sqrt{B}}$
1	< 5	1146
2	< 6	1150
3	< 7	1157
4	< 8	1159
5	< 9	1157
6	< 10	1153
7	< 15	1142

Table A.27: Mass cut of Ξ^- is shown for C4.

	Width (MeV) of Ξ^-	$\frac{S}{\sqrt{B}}$
1	$\pm$ 3.0	4846
2	$\pm$ 6.0	4562
3	$\pm$ 7.5	4227
4	$\pm$ 9.0	3875
5	$\pm$ 11.5	3592
6	$\pm$ 12.0	3350

Table A.28: PID of Ω_c^0 is shown for C4.

	Kaon	Pion	Pion	$\frac{S}{\sqrt{B}}$
1	KLhVeryLoose	PiLhVeryLoose	PiLHVeryLoose	4561
2	KLhVeryLoose	PiLhVeryLoose	PiLLoose	4609
3	KLhVeryLoose	PiLhVeryLoose	PiLTight	4634
4	KLhVeryLoose	PiLhVeryLoose	PiLHVeryTight	4592
5	KLhVeryLoose	PiLhLoose	PiLHVeryLoose	4672
6	KLhVeryLoose	PiLhLoose	PiLLoose	4721
7	KLhVeryLoose	PiLhLoose	PiLTight	4746
8	KLhVeryLoose	PiLhLoose	PiLHVeryTight	4705
9	KLhVeryLoose	PiLhTight	PiLHVeryLoose	4670
10	KLhVeryLoose	PiLhTight	PiLHLoose	4719
11	KLhVeryLoose	PiLhTight	PiLHTight	4745
12	KLhVeryLoose	PiLhTight	PiLHVeryTight	4704
13	KLhVeryLoose	PiLhVeryTight	PiLHVeryLoose	4577
14	KLhVeryLoose	PiLhVeryTight	PiLLoose	4626
15	KLhVeryLoose	PiLhVeryTight	PiLTight	4652
16	KLhVeryLoose	PiLhVeryTight	PiLHVeryTight	4610
17	KLhLoose	PiLhVeryLoose	PiLHVeryLoose	5591
18	KLhLoose	PiLhVeryLoose	PiLLoose	5645
19	KLhLoose	PiLhVeryLoose	PiLTight	5682
20	KLhLoose	PiLhVeryLoose	PiLHVeryTight	5629
21	KLhLoose	PiLhLoose	PiLHVeryLoose	5730
22	KLhLoose	PiLhLoose	PiLHLoose	5788
23	KLhLoose	PiLhLoose	PiLHTight	5826
24	KLhLoose	PiLhLoose	PiLHVeryTight	5773
25	KLhLoose	PiLhTight	PiLHVeryLoose	5732
26	KLhLoose	PiLhTight	PiLLoose	5791
27	KLhLoose	PiLhTight	PiLTight	5830
28	KLhLoose	PiLhTight	PiLHVeryTight	5777
29	KLhLoose	PiLhVeryTight	PiLHVeryLoose	5622
30	KLhLoose	PiLhVeryTight	PiLLoose	5680
31	KLhLoose	PiLhVeryTight	PiLTight	5720
32	KLhLoose	PiLhVeryTight	PiLHVeryTight	5667

Table A.29: Continue on PID of Ω_c^0 is shown for C4.

	Kaon	Pion	Pion	$\frac{S}{\sqrt{B}}$
33	KLhTight	PiLhVeryLoose	PiLHVeryLoose	6723
34	KLhtight	PiLhVeryLoose	PiLLoose	6789
35	KLhTight	PiLhVeryLoose	PiLTight	6837
36	KLhTight	PiLhVeryLoose	PiLHVeryTight	6789
37	KLhTight	PiLhLoose	PiLHVeryLoose	6904
38	KLhTight	PiLhLoose	PiLLoose	6974
39	KLhTight	PiLhLoose	PiLTight	7024
40	KLhTight	PiLhLoose	PiLHVeryTight	6977
41	KLhTight	PiLhTight	PiLHVeryLoose	6910
42	KLhTight	PiLhTight	PiLHLoose	6981
43	KLhTight	PiLhTight	PiLHTight	7034
44	KLhTight	PiLhTight	PiLHVeryTight	6987
45	KLhTight	PiLhVeryTight	PiLHVeryLoose	6785
46	KLhtight	PiLhVeryTight	PiLLoose	6855
47	KLhTight	PiLhVeryTight	PiLTight	6910
48	KLhTight	PiLhVeryTight	PiLHVeryTight	6861
49	KLhVeryTight	PiLhVeryLoose	PiLHVeryLoose	6720
50	KLhVeryTight	PiLhVeryLoose	PiLLoose	6786
51	KLhVeryTight	PiLhVeryLoose	PiLTight	6834
52	KLhVeryTight	PiLhVeryLoose	PiLHVeryTight	6786
53	KLhVeryTight	PiLhLoose	PiLHVeryLoose	6901
54	KLhVeryTight	PiLhLoose	PiLHLoose	6971
55	KLhVeryTight	PiLhLoose	PiLHTight	7022
56	KLhVeryTight	PiLhLoose	PiLHVeryTight	6974
57	KLhVeryTight	PiLhTight	PiLHVeryLoose	6907
58	KLhVeryTight	PiLhTight	PiLLoose	6978
59	KLhVeryTight	PiLhTight	PiLTight	7031
60	KLhVeryTight	PiLhTight	PiLHVeryTight	6984
61	KLhVeryTight	PiLhVeryTight	PiLHVeryLoose	6782
62	KLhVeryTight	PiLhVeryTight	PiLLoose	6852
63	KLhVeryTight	PiLhVeryTight	PiLTight	6906
64	KLhVeryTight	PiLhVeryTight	PiLHVeryTight	6858

Table A.30: χ^2 vertex cut of Ω_c^0 is shown for C4.

	P_{χ^2} of Ω^-	$\frac{S}{\sqrt{B}}$
1	< 5	31194
2	< 10	43800
3	< 13	45274
4	< 14	45457
5	< 15	45397
6	< 16	45422
7	< 17	45081
8	< 18	44800
9	< 20	44320

Table A.31: Mass cut of Ω_c^0 is shown for C4.

	Width (σ) of Ω_c^0	$\frac{S}{\sqrt{B}}$
1	$\pm$ 1.0 σ	242045
2	$\pm$ 2.0 σ	246887
3	$\pm$ 2.5 σ	218589
4	$\pm$ 3.0 σ	198686
5	$\pm$ 3.5 σ	174005
6	$\pm$ 4.0 σ	159840

Appendix B

Other Studies

B.1 Ω_c^* data Fits with Single Gaussian

At this section we fit same $\Delta\Omega_c^*$ distributions, which are given at chapter 4, with single Gaussian. For background we use the same threshold function with 4th order polynomial which is given in section 3.1. The result is given in Table B.1. Fit results are consistent with the fit results of the Crystal Ball funciton (See chapter 4.2).

Table B.1: Fit results of $\Delta\Omega_c^*$ distributions is shown for all decay channels.

Channel	$\Delta\Omega_c^*$	Width (fixed)	Ω_c^* events
$\Omega_c^* \rightarrow \Omega_c^0(\Omega^-\pi^+)\gamma$	2767.0 $\pm$ 1.5	4.0 MeV	32.3 $\pm$ 8.2
$\Omega_c^* \rightarrow \Omega_c^0(\Omega^-\pi^+\ \pi^0)\gamma$	2769.4 $\pm$ 1.3	4.2 MeV	47.7 $\pm$ 13.9
$\Omega_c^* \rightarrow \Omega_c^0(\Xi^-K^-\ \pi^+\ \pi^+)\gamma$	2766.6 $\pm$ 1.6	4.0 MeV	24.4 $\pm$ 9.4
ch1 + ch2 + ch4	2768.1 $\pm$ 0.9	4.0 MeV	101.2 $\pm$ 18.9
ch1 + ch2 + ch3 + ch4	2768.2 $\pm$ 1.1	4.0 MeV	89.7 $\pm$ 19.5

B.2 Ω_c^* Studies

In this part we answer RC requests.

B.2.1 More Ω_c^* Signal MC Information

This table is prepared to answer Wolfgang Mader's request.

Table B.2: Ω_c^* signal MC table

	Ch1 (Events)	Ch2 (Events)	Ch3 (Events)	Ch4 (Events)
a	115 K	60 K	174 K	57 K
b	108035	57024	165190	53916
c	89877	47324	137028	44793
d	5712 $\pm$ 100	1305 $\pm$ 53	4457 $\pm$ 108	1212 $\pm$ 47
e	5255	996	4271	1138
f	5141 $\pm$ 63	967 $\pm$ 24	4076 $\pm$ 65	1131 $\pm$ 31

a-) Number of events generated (from tcl files)

b-) Number of generated Ω_c^* events (no cut at all).

c-) Number of generated Ω_c^* events with $X_p > 0.5$ cut.

d-) Non truth match fitted Ω_c^* events (with all the selection criteria)

e-) Number of Ω_c^* events with truth match (no fit with all the selection criteria)

f-) Number of Ω_c^* events after truth match and with fit (with all the selection criteria).

B.2.2 X_p and γ Energy Study

This is prepared to answer Mike Roney's request. In this part we plot X_p and γ Energy distributions using data for all decay channels except for the the decay

channel C3 where we do not observe Ω_c^* signal.

B.2.3 γ Energy Study in $c\bar{c}$ MC and in Data

This is prepared to answer Wolfgang Mader's request. In this part we plot γ Energy distributions using $c\bar{c}$ MC and data.

B.3 Study of γ energy cut.

We use a minumum γ energy cut of 80 MeV for the γ s coming from Ω_c^*. The systematic uncertainty due to the requirement of the energy is studied by varying the γ energy by $\pm$ 2 MeV. We observe a 4.5 % change in the mean value of the result. Conservatively, we assign 4.5% as a systematic uncertainty due to the energy γ energy cut. (For RC).

B.4 Study of X_p cut

We have studied by changing $X_p(\Omega_c^*\ ) > 0.5$ to $X_p(\Omega_c^0) > 0.5$ in the data. The new efficiency and fit results are summarized in Table B.3. The fitted mass distribution is shown in Figure B.13. The change in efficiency is very small and the fitted signal yield consistent with the yield we get by the requirement of $X_p(\Omega_c^*) > 0.5$.

Table B.3: Fit results of $\Delta\Omega_c^*$ distributions for all decay channels. Lineshapes are fixed to Ω_c^* signal MC except for the mean values.

Ch	$\Delta\Omega_c^*$ (MeV)	σ (MeV)	Ω_c^* events	Eff(%) ($X_p(\Omega_c^0)$)	Eff(%)($X_p(\Omega_c^*)$)
C1	$2766.7^{+1.4}_{-1.4}$	4.0 (fixed)	$38.8^{+9.8}_{-9.0}$	5.745 $\pm$ 0.061	5.720 $\pm$ 0.070
C2	$2769.3^{+1.3}_{-1.2}$	4.2 (fixed)	$43.4^{+14.7}_{-14.0}$	2.063 $\pm$ 0.034	2.043 $\pm$ 0.051
C3	2767.4 (fixed)	4.0 (fixed)	$-3.3^{+3.8}_{-3.1}$	3.048 $\pm$ 0.041	2.975 $\pm$ 0.047
C4	$2766.9^{+1.9}_{-1.9}$	4.0 (fixed)	$20.2^{+9.3}_{-8.5}$	2.522 $\pm$ 0.068	2.525$\pm$ 0.069

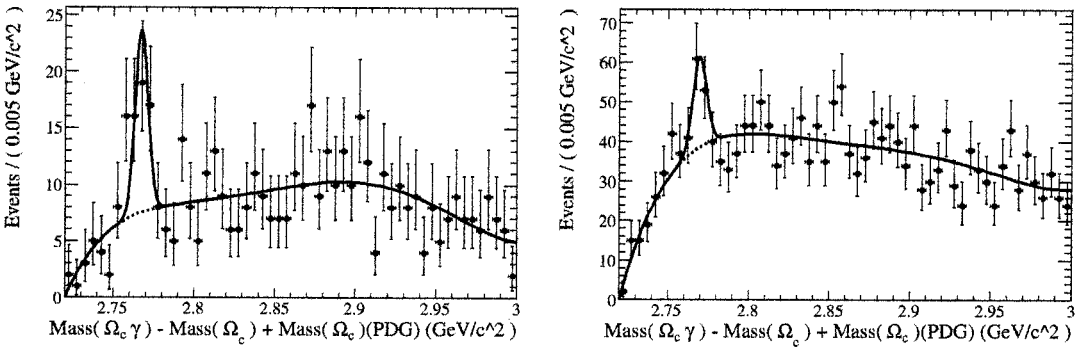

Figure B.1: $\Delta\Omega_c^*$ distribution in data is shown for the decay channel (C1 is shown on the left. On the right,$\Delta\Omega_c^*$ distribution in data is shown for the decay channel C2. On the left, the mean value is 2767.0 $\pm$ 1.5 MeV, σ_1 is fixed to 4.0 MeV and the yield is 32.3 $\pm$ 8.2 events. On the right, the mean value is 2769.4 $\pm$ 1.3 MeV, σ is fixed to 4 MeV and the yield is 47.7 $\pm$ 13.9 events.

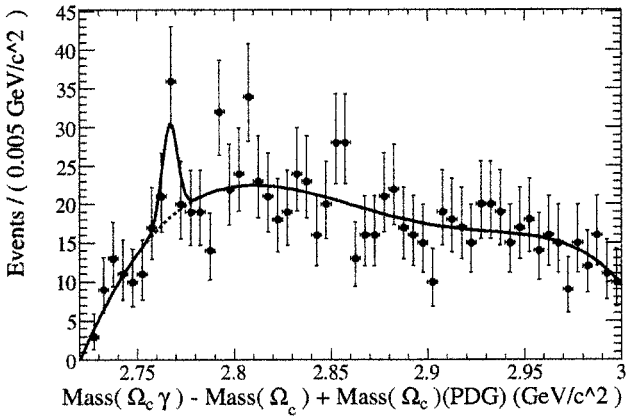

Figure B.2: $\Delta\Omega_c^*$ distribution in data is shown for the decay channel ($\Omega_c^0 \rightarrow \Xi^-$ km $\pi^+ \pi^+)\gamma$. The mean value is 2766.6 $\pm$ 1.6 MeV, σ is fixed to 4.0 MeV, and the yield is 24.4 $\pm$ 9.4 events.

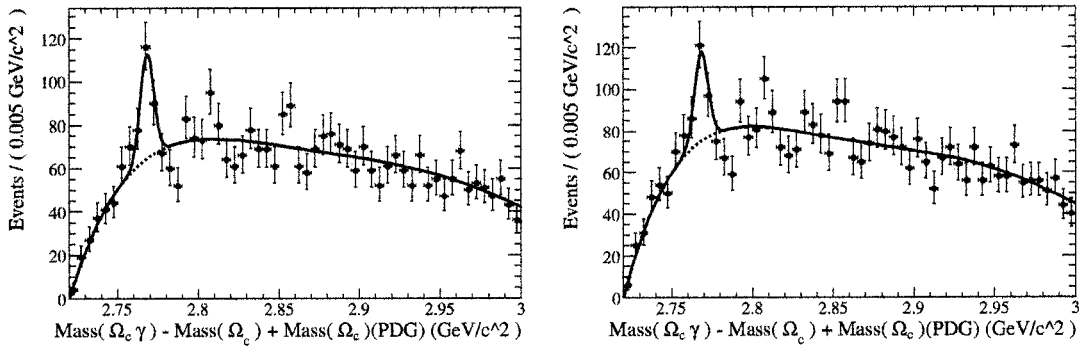

Figure B.3: $\Delta\Omega_c^*$ distribution in data with all channels together except for the decay channel (C3 is shown on the left (σ is fixed). On the right,$\Delta\Omega_c^*$ distribution with all channel together. On the left, the mean value is 2768.1 $\pm$ 0.9 MeV, σ_1 is fixed to 4.0 MeV and the yield is 101.2 $\pm$ 18.9 events. On the right, the mean value is 2768.2 $\pm$ 1.1, σ is fixed to 4 MeV and the yield is 89.7 $\pm$ 19.5 events.

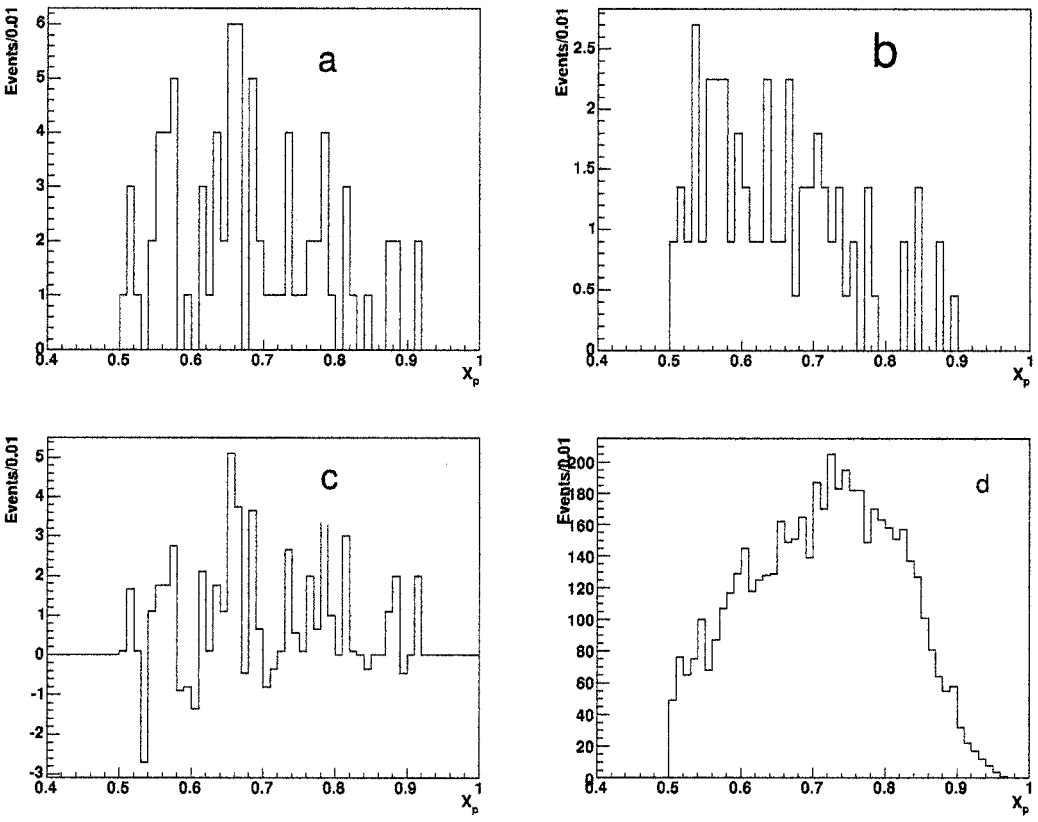

Figure B.4: X_p distributions are shown for the decay mode (C1 in data (a, b and c) and in signal MC (d). a: X_p distribution is shown for the signal region ($2.7554(GeV) < M(\Omega_c^*) < 2.7799(GeV)$). b:$X_p$ distribution is shown for normalized background from Ω_c^* sideband data ($2.8000(GeV) < M(\Omega_c^*) < 2.8480(GeV)$). c: Background subtracted signal X_p distribution is shown (a-b). d: X_p distribution is shown in signal MC.

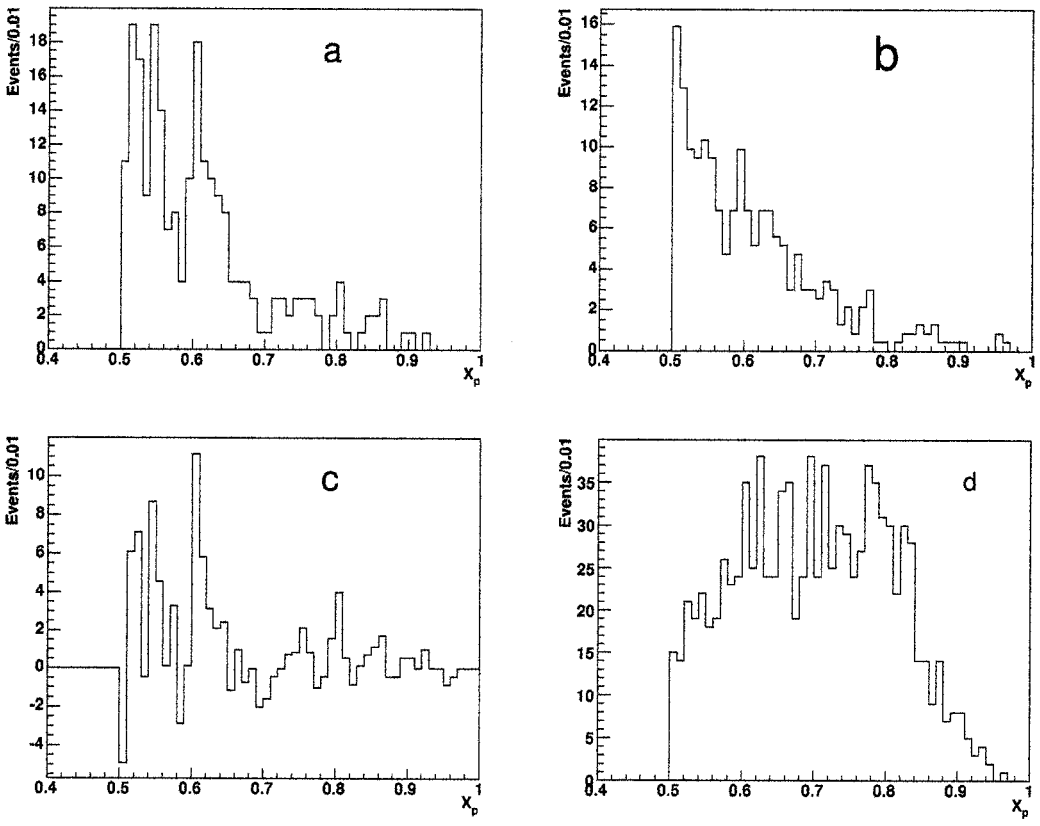

Figure B.5: X_p distributions are shown for the decay mode C2 in data (a, b and c) and in signal MC (d). a: X_p distribution is shown for the signal region $(2.7548(GeV) < M(\Omega_c^*) < 2.7805(GeV))$. b:$X_p$ distribution is shown for normalized background from Ω_c^* sideband data $(2.8000(GeV) < M(\Omega_c^*) < 2.8504(GeV))$. c: Background subtracted signal X_p distribution is shown (a-b). d: X_p distribution is shown in signal MC.

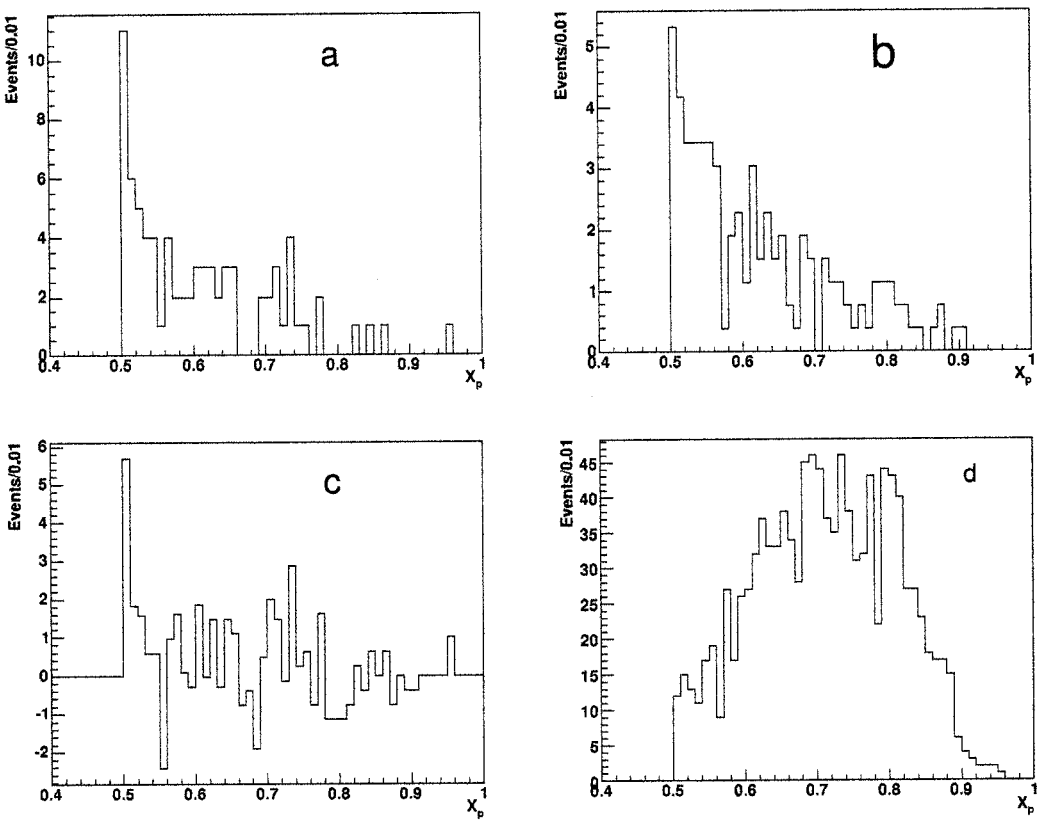

Figure B.6: X_p distributions are shown for the decay mode (C4 in data (a, b and c) and in signal MC (d). a: X_p distribution is shown for the signal region ($2.7554(GeV) < M(\Omega_c^*) < 2.7799(GeV)$). b:$X_p$ distribution is shown for normalized background from Ω_c^* sideband data ($2.8000(GeV) < M(\Omega_c^*) < 2.8480(GeV)$). c: Background subtracted signal X_p distribution is shown (a-b). d: X_p distribution is shown in signal MC.

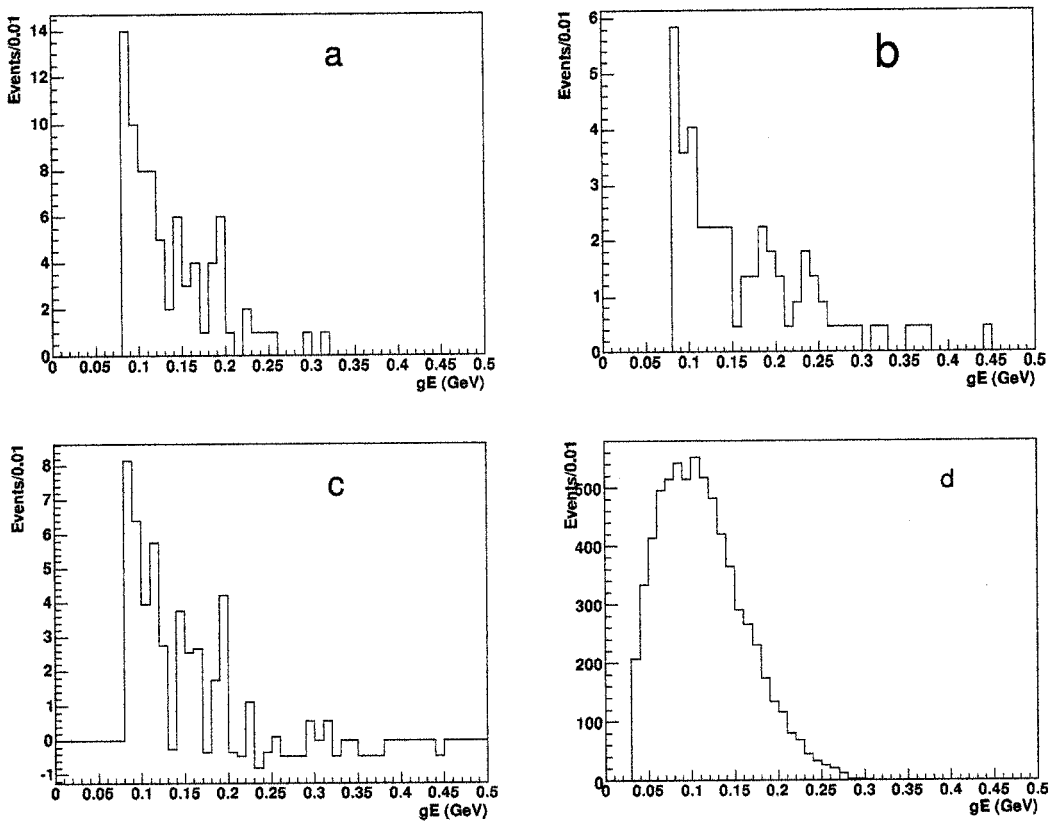

Figure B.7: γ energy distributions are shown for the decay mode (C1 in data (a, b and c) and in signal MC (d). a: γ energy distribution is shown for the signal region ($2.7554(GeV) < M(\Omega_c^*) < 2.7799(GeV)$). b: γ energy distribution is shown for normalized background from Ω_c^* sideband data ($2.8000(GeV) < M(\Omega_c^*) < 2.8480(GeV)$). c: Background subtracted signal γ energy distribution is shown (a-b). d: γ energy distribution is shown in signal MC.

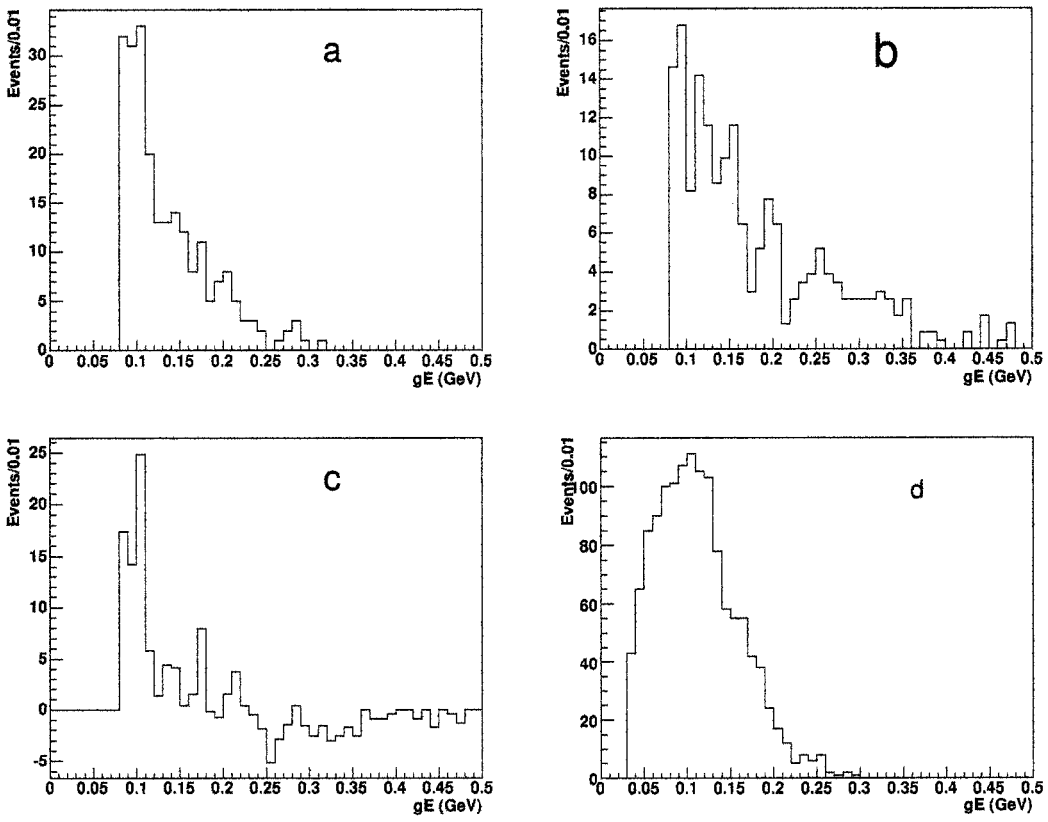

Figure B.8: γ energy distributions are shown for the decay mode C2 in data (a, b and c) and in signal MC (d). a: γ energy distribution is shown for the signal region ($2.7548(GeV) < M(\Omega_c^*) < 2.7805(GeV)$). b: γ energy distribution is shown for normalized background from Ω_c^* sideband data ($2.8000(GeV) < M(\Omega_c^*) < 2.8504(GeV)$). c: Background subtracted signal γ energy distribution is shown (a-b). d: γ energy distribution is shown in signal MC.

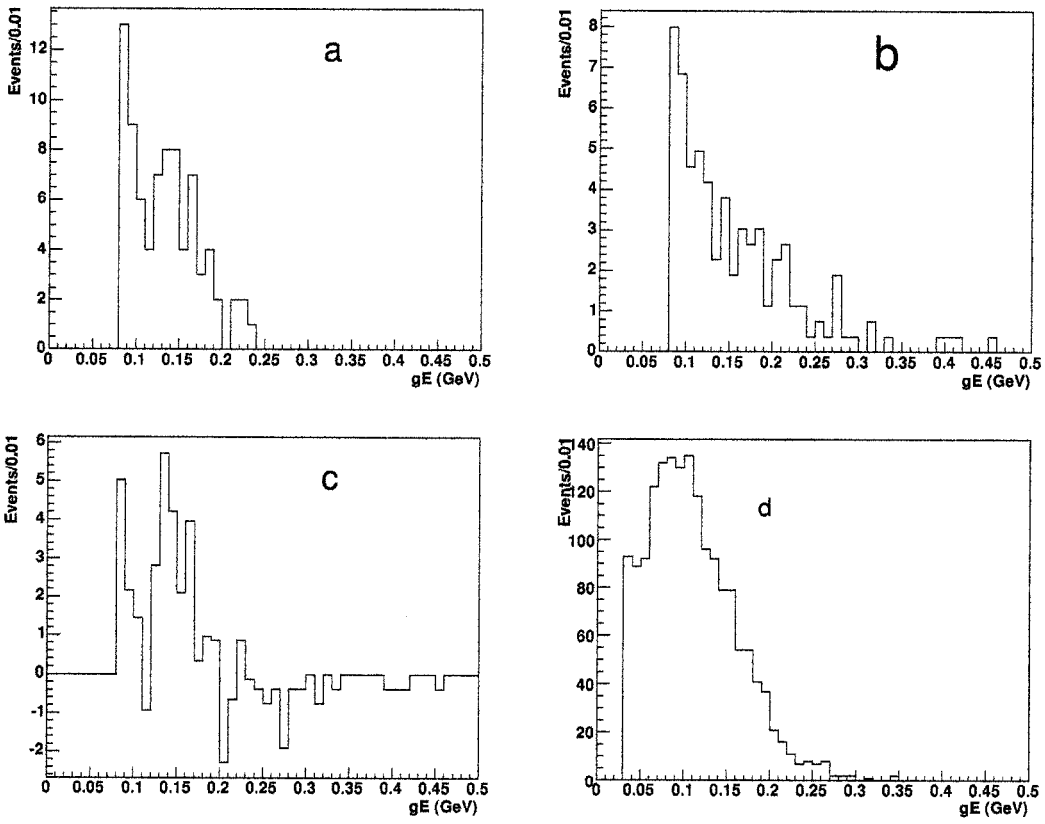

Figure B.9: γ Energy distributions are shown for the decay mode (C4 in data (a, b and c) and in signal MC (d). a: γ Energy distribution is shown for the signal region ($2.7554(GeV) < M(\Omega_c^*) < 2.7799(GeV)$). b: γ Energy distribution is shown for normalized background from Ω_c^* sideband data ($2.8000(GeV) < M(\Omega_c^*) < 2.8480(GeV)$). c: Background subtracted signal γ energy distribution is shown (a-b). d: γ energy distribution is shown in signal MC.

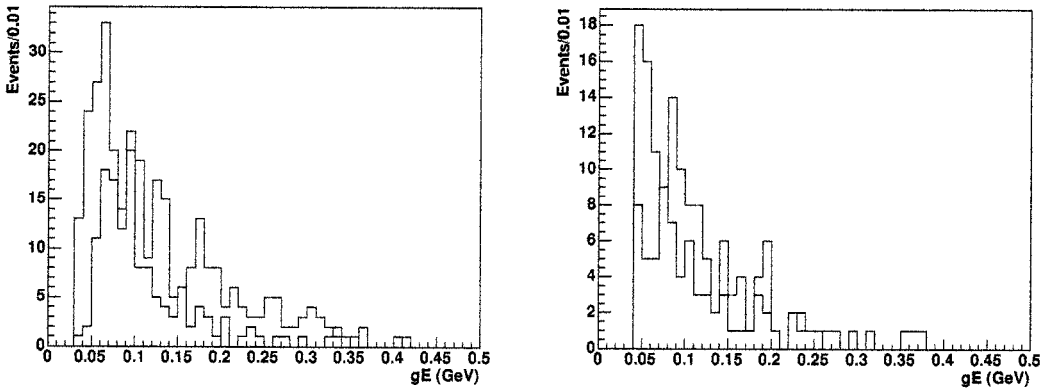

Figure B.10: γ energy distributions is shown for the decay mode (C1 in $c\bar{c}$ MC (on the left) and in data (on the right). Red color is used for the signal region ($2.7854(GeV) < M(\Omega_c^*) < 2.8094(GeV)$ in $c\bar{c}$ MC and $2.7554(GeV) < M(\Omega_c^*) < 2.7799(GeV)$ in data). Black color is used for the sideband ($2.8200(GeV) < M(\Omega_c^*) < 2.8440(GeV)$).

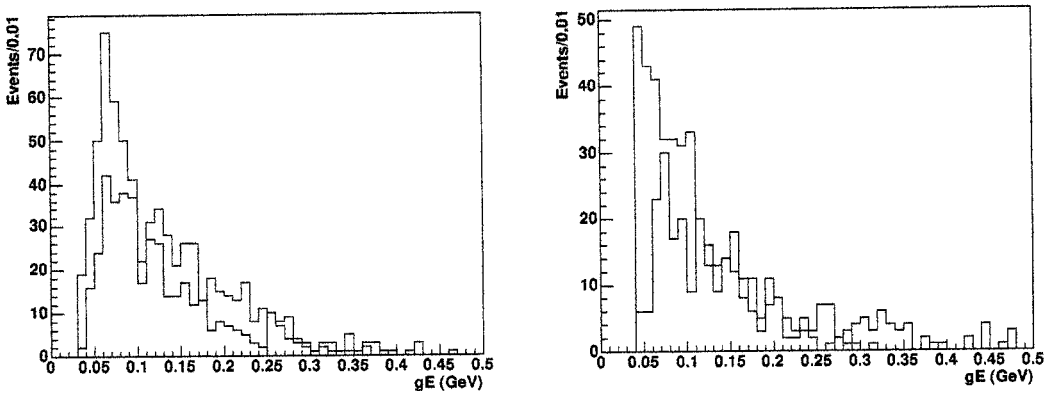

Figure B.11: γ energy distributions is shown for the decay mode C2 in $c\bar{c}$ MC (on the left) and in data (on the right). Red color is used for the signal region ($2.7854(GeV) < M(\Omega_c^*) < 2.8094(GeV)$ in $c\bar{c}$ MC and $2.7554(GeV) < M(\Omega_c^*) < 2.7799(GeV)$ in data). Black color is used for the sideband ($2.8200(GeV) < M(\Omega_c^*) < 2.8440(GeV)$).

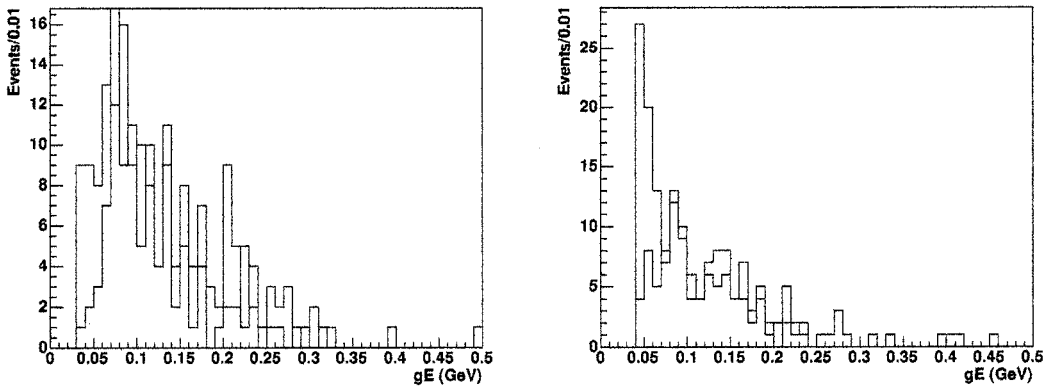

Figure B.12: γ energy distributions is shown for the decay mode (C4 in $c\bar{c}$ MC (on the left) and in data (on the right). Red color is used for the signal region ($2.7854(GeV) < M(\Omega_c^*) < 2.8094(GeV)$ in $c\bar{c}$ MC and $2.7554(GeV) < M(\Omega_c^*) < 2.7799(GeV)$ in data). Black color is used for the sideband ($2.8200(GeV) < M(\Omega_c^*) < 2.8440(GeV)$).

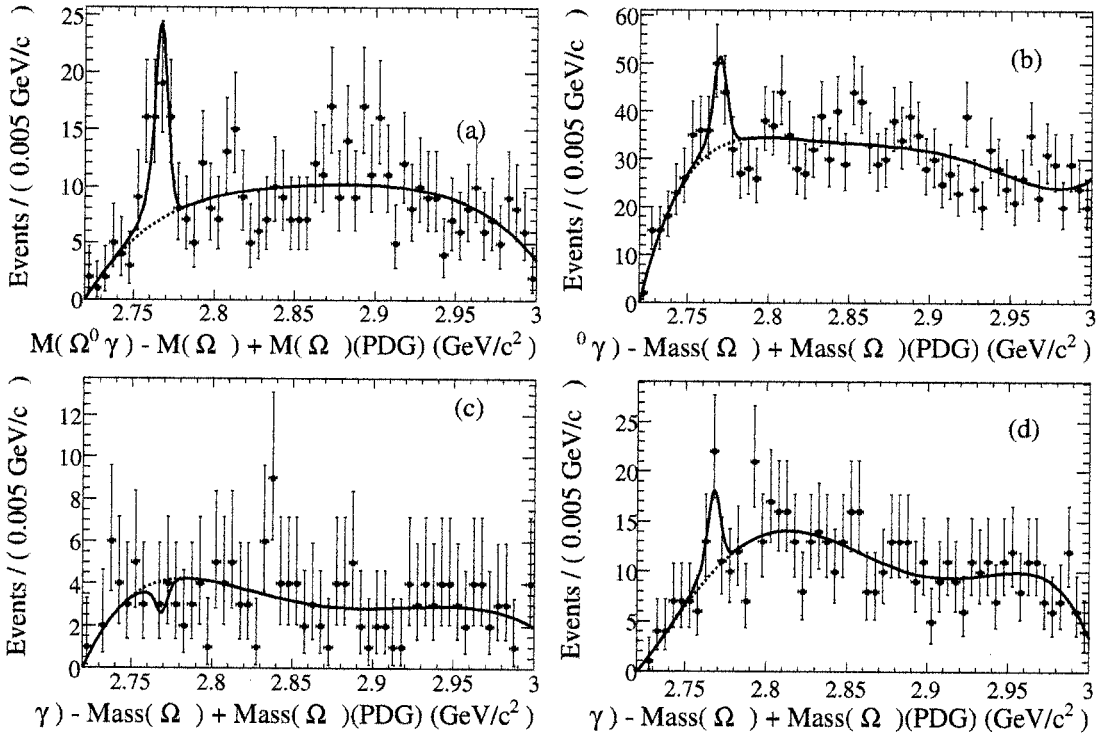

Figure B.13: $\Delta\Omega_c^*$ distribution in data for the decay channel (C1 is shown on the Figure(a), Figure(b) for $\Omega_c^* \rightarrow \Omega_c^0(\Omega^-\pi^+\ \pi^0)\gamma$, Figure(c) for $\Omega_c^* \rightarrow \Omega_c^0(\Omega^-\pi^+\ \pi^-\ \pi^+)\gamma$ and Figure(d) for $\Omega_c^* \rightarrow \Omega_c^0(\Xi^-K^-\ \pi^+\ \pi^+)\gamma$. The lineshape is fixed to Ω_c^* signal MC except the mean value.

B.5 Cross Check with varying X_p Cuts

X_p cuts: We change X_p values of Ω_c^* and Ω_c^0 by $\pm$ 0.025. The effect is about 2% on the final result.

B.6 Efficiency study as function of X_p (by changing the shape of fragmentation function)

We study the effect of different fragmentation function on the signal detection efficiency for the decay channel C1. The generated level X_p distribution is shown in Figure B.14 in signal MC. We weight the distribution by the Peterson fragmentation function [35]. The Peterson fragmentation function is defined as,

$$\frac{dN}{dx_p} \alpha \frac{1}{x_p(1-\frac{1}{x_p}-\frac{\epsilon}{(1-x_p)})^2}$$

;

The Peterson fragmentation function is shown in Figure B.15 for different ϵ values. We have varied the fragmentation function and the result is summarized in Table B.4.

Table B.4: Outline of systematic errors

ϵ	Relative Change in Detection Efficiency (%)
0.06	7.5
0.08	3.0
0.10	1.3
0.15	2.6

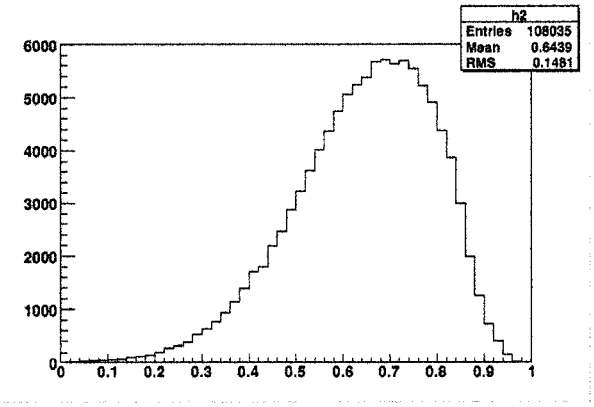

Figure B.14: X_p distribution at generator level is shown for the decay mode C1 .

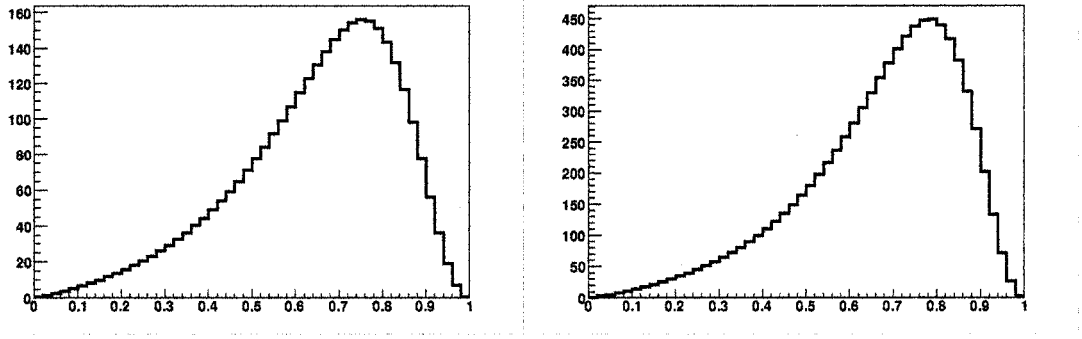

Figure B.15: On the left Peterson fragmentation function for $\epsilon = 0.08$ is shown, On the right Peterson fragmentation function for $\epsilon = 0.06$ is shown.

Bibliography

[1] Geant4 Collaboration, "Geant4 - A Simulation ToolKit", CERN-IT-2002-003. To be published in Nucl. Instrum. Meth. A.

[2] L. Burakovsky and T. Goldman.Phys. Rev. D Volume 56, Number 11 (1997).

[3] A. Martin and J. M. Richard, Phys. Lett. B 355, 345 (1995).

[4] M.J. Savage, Phys. Lett. B 359, 189 (1995).

[5] J. L. Rosner, Phys. Rev. D 52, 6461 (1995).

[6] R. Roncaglia, D. B. Lichtenberg, and E. Predazzi, Phys. Rev. D 52, 1722 (1995).

[7] D. B. Lichtenberg, R. Roncaglia, and E. Predazzi, Phys. Rev. D 53, 6678 (1996).

[8] A. Zalewska and K. Zalewski,'Heavy Baryon Masses,' hep-ph/9608240.

[9] L. Ya. Glozman and D. O. Riska, Nucl. Phys. A603, 326 (1996).

[10] E. Jenkins, Phys. Rev. D 54, 4515 (1996);55, R10 (1997).

[11] A. De. Rujula, H. Georgi, and S. L. Glashow, Phys. Rev. D 12, 147 (1975).

[12] J.-L. Basdevant and S. Boukraa, Z. Phys. C 30, 103 (1986).

[13] A. M. Badalyan, Phys. Lett. B 199, 267 (1987); A. M.Badalyan and D.I. Kitoroage, Sov. J. Nucl. Phy. 47, 515 (1988).

[14] S. Fleck and J. M. Richard, Part. World 1, 67 (1990).

[15] K. Maltman and N. Isgur, Phys. Rev. D 22, 1701 (1980).

[16] H.W. Siebert, in Topics in Hadron Spectroscopy, edited by D. C. Peasley (Nova Science, Commack, NY, 1995), Vol. 3, p.11.

[17] W. A. Ponce, Phys. Rev. D 19, 2197 (1979).

[18] D. Izatt, C. DeTar, and M. Stephenson, Nucl. Phys. B199, 269 (1982).

[19] M. Sadzikowski, Acta Phys. Pol. B 24, 1121 (1993).

[20] S. Samuel and K. J. M. Moriarty, Phys. Lett. 166B, 413 (1986); Phys. Lett. B 175, 197 (1986).

[21] K. C. Bowler et al., Phys. Rev. D 54, 3619 (1996).

[22] J. G. Korner, M. Kramer, and D. Pirjol, Prog. Part. Nucl. Phys. 33, 787 (1994).

[23] M. Rho, D. O. Riska, and N. N. Scoccola, Phys. Lett. B 251, 597 (1990).

[24] L. H. Chan, Phys. Rev. D 15. 2478 (1977).

[25] G. Q. Sofi and M. Ahmad, Acta Phys. Pol. B 10, 619 (1979).

[26] J. Dey, M. Dey, and P. Volkovitsky, Phys. Lett. B 261, 493 (1991), 375 358 (1996).

[27] S. Iwao, Prog. Theor. Phys. 87, 1443 (1992).

[28] K. Suziki and H. Toki, Mod. Phys. Lett. A 7, 2867 (1992).

[29] BAD 1345 D. C. Willams, Observation of a Baryon Decaying to D^0p at a Mass of 2.94 GeV/c^2

[30] hep-ex/0207079 v1 25 July 2002.

[31] G. J. Feldman and R. D. Cousins, Phys. Rev. D 57, 3873 (1998).

[32] *http : //www.slac.stanford.edu/BFROOT/www/Physics/Analysis/AWG*

[33] S. Eidelman et al., Phys. Lett. B 592, 1 (2004).

[34] BAD 790.

[35] C. Peterson et al., Phys. Rev. D 27, 105 (1983).

[36] G. Punzi, Sensitivity of Searches for New Signals and its Optimization, physics/0308063 (2003).